NTNU
Norwegian University of
Science and Technology

Simulation and Fabrication of a Photonic Crystal Mach-Zehnder Interferometer

Lars Grønmark Holmen

Nanotechnology
Submission date: July 2016
Supervisor: Astrid Aksnes, IET
Co-supervisor: Jens Høvik, IET
Kay Gastinger, NTNU NanoLab

Norwegian University of Science and Technology
Department of Electronics and Telecommunications

This page is intentionally left blank

This thesis is typeset using LaTeX 2_ε and the KOMA-Script report-class. Sketches and illustrations are created with PGF/Ti*k*Z, and data plots with pgfplots. The thesis is intended to be printed in color.

Problem Description

Integrated photonics is the optical counterpart to integrated electronics, and involves the design and fabrication of on-chip components such as dielectric waveguides, couplers, resonators and modulators.

In this master's project, slab photonic crystals with two-dimensional periodicity will be investigated for use as optical biosensors. The sensor will be an integrated Mach-Zehnder interferometer implemented on the silicon-on-insulator material platform. The focus of this project will be dual, where sensor design and simulations are combined with device fabrication and characterization.

Computer simulations of photonic crystals will be made using eigenmode computations with MIT Photonic Bands (MPB) and finite-difference time-domain simulations with MIT Electromagnetic Equation Propagation (Meep). The overall aim is to simulate and understand fundamental aspects of wave propagation in various photonic crystal structures, and investigate the possibility of using PhCs as a platform for making interferometric label-free optical biosensors.

Fabrication will be performed in the NTNU NanoLab cleanroom facilities and consists of training on and use of nanofabrication instruments such as plasma-enhanced chemical vapor deposition (PECVD), electron beam lithography (EBL) and inductively coupled plasma-reactive ion etching (ICP-RIE). Devices will be characterized using e.g. scanning electron microscopy (SEM), reflectometry and atomic force microscopy (AFM). The goal of the experimental part of the project is to develop and systematically optimize fabrication processes in order to make devices of high optical quality.

Abstract

Photonic crystals (PhC) are materials with extraordinary optical properties in terms of dispersion characteristics and light confinement, which make them a promising platform for photonic integrated circuits. This study aims at designing, simulating and fabricating a Mach-Zehnder interferometer (MZI) implemented in an air-hole silicon photonic crystal slab, with a specific application as a label-free optical biosensor.

Computer simulations are performed in both two and three dimensions using the freely available software packages MIT Photonic Bands [1] for computation of eigenmodes in periodic dielectric media, and MIT Electromagnetic Equation Propagation [2] for finite-difference time-domain simulations of transmission through finite-sized devices. The transmission properties of the interferometer are investigated and optimized at the level of its discrete constituents (linear defect waveguides, 60° bends and Y-splitters), before the MZI is studied for use in label-free sensing of biomaterials, where biolayers added to the sensing arm of the interferometer are used to modulate the output intensity.

After studying fundamental mechanisms for optical losses in PhC waveguides, structural optimizations resulted in high and broadband transmission through complete MZIs, with 3 dB bandwidths of 99 nm and 53 nm in 2D and 3D, respectively. Addition of biolayers to the MZI sensing arm successfully resulted in modulations of the output intensity in form of sharp transmission dips caused by excitation of high-Q resonances. The simulations demonstrate a novel concept of a compact MZI with promising possibilities of working as a label-free biosensor.

Fabrication of photonic crystal structures is performed using electron beam lithography (EBL)-patterning followed by inductively coupled plasma-reactive ion etching (ICP-RIE) of silicon-on-insulator (SOI) substrates made by depositing SiO_2 and amorphous silicon onto silicon wafers using plasma-enhanced chemical vapor deposition (PECVD).

The systematic optimizations of fabrication processes resulted in high-quality silicon structures, having RMS sidewall roughness $<$1 nm as measured from top-view SEM images, and vertically etched sidewalls with angles from 1° to 2°. With respect to hole shape, sidewall roughness and process reproducibility, these are the best results from fabrication of silicon photonic crystals achieved at NTNU. Work remains on optical characterization of fabricated devices and development of biofunctionalization processes, but the processes developed form a promising basis for future fabrication of functional SOI photonic devices.

Sammendrag

Fotoniske krystaller (PhC) er materialer med unike dispersjonsegenskaper og muligheter for lokalisering av lys, hvilket gjør dem til en lovende platform for integrert fotonikk. Denne studien tar for seg design, simuleringer og fabrikasjon av et Mach-Zehnder interferometer (MZI) implementert som en luft-hull silisiummembran fotonisk krystall, med den spesifikke applikasjonen som markør-fri optisk biosensor.

Datasimuleringer blir utført i både to og tre dimensjoner med de fritt tilgjengelig programvarepakkene MIT Photonic Bands [1] for beregning av egenmoder i periodiske dielektriske medier, og MIT Electromagnetic Equation Propagation [2] for finite-difference tidsdomenesimuleringer av transmisjon gjennom komponenter av endelig utstrekning. Transmisjonsegenskapene til interferometeret undersøkes og optimeres først for hver individuelle bestanddel, (lineære defektbølgeledere, 60° svinger og Y-splittere), før MZIet studeres for bruk innen markør-fri deteksjon av biomaterialer, hvor biolag lagt på sensorarmen til interferometeret brukes til å modulere utgangsintensiteten.

Etter å ha studert fundamentale mekanismer for optiske tap i PhC-bølgeledere, resulterte strukturelle optimeringer i høy og bredbåndet transmisjon gjennom det komplette MZIet, med 3 dB båndbredder på 99 nm og 53 nm i henholdsvis 2D og 3D. Biolag lagt på sensorarmen til MZIet resulterte i modulasjoner av utgangsintensiteten i form av skarpe transmisjonsfall grunnet eksitasjon av resonanser med høy Q-faktor. Simuleringene demonstrerer et lovende konsept for et kompakt MZI med muligheter for anvendelse som en markør-fri biosensor.

Fabrikasjon av fotoniske krystallstrukturer gjøres med elektronstrålelitografi (EBL) etterfulgt av inductively coupled plasma-reactive ion etsing (ICP-RIE) av silicon-on-insulator (SOI) substrater laget ved deponering av SiO_2 og amorft silisium på silisiumskiver ved plasma-enhanced chemical vapor deposition (PECVD).

Systematisk optimering av fabriksjonsprosesser har resultert i silisiumstrukturer av høy kvalitet, med RMS sideveggsruhet under 1 nm, målt ved analyse av top-view SEM-bilder. Sideveggene var vertikalt etset med vinkler mellom 1° og 2°. Basert på hullform, sideveggsruhet og reproduserbarheten til prosessene er dette de beste resultatene fra fabrikasjon av fotoniske krystaller av silisium oppnådd på NTNU. Arbeid gjenstår med optisk karakterisering av fabrikerte komponenter og utvikling av biofunksjonaliseringsprosesser, men de utviklede prosessene danner en lovende basis for fremtidig fabrikasjon av funksjonelle SOI fotoniske komponenter.

Preface

This thesis is submitted in partial fulfillment of the requirements for the degree of Master of Science in Nanotechnology at the Department of Electronics and Telecommunications (IET) at the Norwegian University of Science and Technology (NTNU).

This work is a continuation of a one semester project performed in the Fall 2015 [3], which consisted of design and computer simulations of photonic crystal structures intended for use as biosensors. Part of the work is reproduced here, most notably parts of the theory chapter. The experimental parts of the project build partly upon previous work at IET [4, 5, 6, 7, 8], from which primarily fabrication processes are inspired.

Everything presented is entirely the work of the author with the following exceptions:

- Figures 3.1, 3.6 and 3.7 were kindly provided by Ane Tefre Eide, and were made in the context of her own Master's thesis.
- The AFM instrument used in Section 5.2.2 for measuring surface roughness was operated by Ane Tefre Eide.

Acknowledgements

I am grateful for the help and support from several people during this project. Firstly, I thank my supervisor Prof. Astrid Aksnes for prioritizing her students in a busy schedule, supervising with great enthusiasm and for taking me to my first conference. Also, our discussions about scientific writing are highly appreciated.

Secondly, I thank my co-supervisor Jens Høvik for sharing his cleanroom experience and process recipes, and for providing on-demand instrument training. The numerous instruments and processes needed for the experimental part of this work would be difficult to master in the time frame of one semester without his efforts.

Also my other co-supervisor, Dr. Kay Gastinger, deserves acknowledgement for hosting rewarding group meetings where both issues of organizational character and fabrication-specific problems were discussed and solved.

I thank Einar Standal Digernes for useful discussions and help with lithography-related problems, Jakob Vinje for discussions about report formatting, and the rest of my classmates for making these five years outstanding!

I thank you, Ane, for all your help and support, and also for performing AFM measurements and for allowing me to use your beautiful illustrations of instrumental setups.

The Research Council of Norway is acknowledged for the support to the Norwegian Micro- and Nano-Fabrication Facility, NorFab.

Contents

List of Abbreviations

a-Si	Amorphous Silicon
BZ	Brillouin Zone
CCP	Capacitively Coupled Plasma
CMOS	Complementary Metal-Oxide-Semiconductor
CMP	Chemical-Mechanical Polishing/Planarization
DI	Deionized (water)
EBL	Electron Beam Lithography
FDTD	Finite-Difference Time-Domain
FEM	Finite Element Method
ICP-RIE	Inductively Coupled Plasma-Reactive Ion Etching
IPA	Isopropyl Alcohol (isopropanol)
LER	Line Edge Roughness
MEEP	MIT Electromagnetic Equation Propagation
MPB	MIT Photonic Bands
MZI	Mach-Zehnder Interferometer
PECVD	Plasma-Enhanced Chemical Vapor Deposition
PhC	Photonic Crystal
PML	Perfectly Matched Layer
RIU	Refractive Index Units
RMS	Root Mean Square
sccm	Standard cubic centimeters per minute

SEM	Scanning Electron Microscopy
$\mathbf{SiO_2}$	Silicon Dioxide
SOI	Silicon-on-Insulator
TE	Transverse-Electric
TIR	Total Internal Reflection
TM	Transverse-Magnetic

Chapter 1.

Introduction

Integrated photonics is the optical counterpart of integrated electronics, and consists of monolithic integration of various optical functions on a single chip, where some examples are light generation, transportation, filtering and detection [9]. Compared to the use of discrete components, photonic integrated circuits enable increased functionality, lower cost and higher reliability. Possible applications range from optical computer interconnects and ultrafast telecommunication to metrology, spectroscopy and sensing applications [10, Ch. 13].

Photonic Crystals

One particularly attractive type of optical structures with sufficiently strong light-confinement needed for dense photonic circuit integration is *photonic crystals* (PhC). In short, photonic crystals are materials that have a periodic dielectric constant, $\varepsilon(\mathbf{r})$, where the periodicity is comparable in size to the wavelength of light. Since they were suggested by Yablonovitch [11] and John [12] in 1987, these materials have been extensively studied due to their remarkable potential in manipulation of light propagation.

Photonic crystals can be made to posses *photonic band gaps*, which are frequency ranges where the crystal supports no propagating electromagnetic modes – much comparable to the energy band gap for electrons in periodic atomic crystals. By intentionally introducing defects in the PhC, states within the band gap can be created and give rise to localized modes that can be used for e.g. lossless confinement of light around sharp bends, or confinement in wavelength-scale cavities [13]. The extraordinary light confinement properties of PhCs can be used for achieving high density integrated optics.

Particularly interesting for practical applications are PhCs with periodicity in two dimensions, since these can be fabricated on-chip using standard lithography and etching techniques. Due to the wavelength-comparable dimensions of PhC features, modern nanofabrication techniques allow for an high degree of flexibility in structural design, and PhCs can be accurately tuned to have desired properties. A specific material system called *silicon-on-insulator* (SOI) is regarded as one of the most promising routes towards large-scale deployment of photonic integrated circuits [10, Ch. 13]. SOI has a high contrast in refractive index between silicon and SiO_2, which allows strong light confinement. Also, the material system is compatible with the mature CMOS industry, enabling mass-production of high-quality functional optical circuits.

Photonic Crystal Biosensors

One promising PhC-application is as sensors detecting e.g. gases or biomaterials, and recent work has demonstrated PhC sensors used for label-free detection of femto gram amounts of biomaterials [14, 15, 16]. By functionalizing a sensor surface with biorecognition molecules, target analytes can bind specifically to these and replace the buffer solution in close vicinity to the surface. Most commonly, the transduction method of the reported PhC biosensors has been based on spectral shifts of defect-mode resonances caused by biomolecule-induced changes in effective refractive index [17]. Although being highly sensitive to biomaterials, these sensors are inherently susceptible to noise and drift caused by e.g. changes in temperature or the background refractive index. Sensors based on interferometric transduction could be more attractive, due to the intrinsic reduction of common-mode noise from the use of sensing- and reference channels [17].

Objectives

The scope of this project is twofold. Firstly, the theoretical part aims to design and simulate a photonic crystal Mach-Zehnder interferometer for use in sensing of biomaterials. Focus is put on gaining a thorough understanding of light propagation in PhC waveguides and other structural components of the interferometer using both frequency-domain and time-domain computer simulations.

Secondly, the experimental part consists of fabrication of silicon nanophotonic devices. Originally, the intention was to optically characterize these devices, but substantial downtime of the PECVD-instrument during the project required a reprioritization from making functional devices to development and optimization of individual fabrication processes. Thus, the goal of the experimental part is to realize high-quality silicon nanophotonic devices, and form a solid framework of processes for future fabrication and characterization of functional devices.

Thesis Overview

Chapter 2 presents general theory of electromagnetic wave propagation in periodic dielectric media, in addition to specific theory of the PhC devices and -applications considered in this project.

Chapter 3 describes the methods and tools used in this Master's project for simulating and fabricating devices. The chapter is intended as a concise but self-consistent presentation of the various tools since aspects of their theory will be repeatedly referenced throughout the thesis. This chapter is kept separate from the theory chapter since experimental equipment is considered, but also separate from the experimental procedure because of the focus on general working principles.

Chapter 4 considers the experimental procedures. Both the simulations performed and fabrication steps with relevant parameters and recipes are presented.

Chapter 5 presents the findings from computer simulations and from fabrication of PhC devices. To aid the readability of the thesis, it is decided to discuss the results as they are presented. Summaries of the key findings are included at the end of each main section of this chapter (5.1 – Simulations and 5.2 – Fabrication).

Chapter 6 concludes the results obtained in this project, and suggests research topics of particular relevance for future work.

Chapter 2.

Theory

This chapter explains the fundamental optical properties of photonic crystals. We start the discussion by introducing Maxwell's equations and specializing them for the media we are interested in. From there, the equations are recast into a Hermitian eigenvalue formulation which due to the similarity to well-established results in quantum mechanics allows us to gain intuitive insight into concepts that are complex in nature. Later, a brief description of label-free optical biosensing is given, along with how photonic crystals can be used for this. Lastly, theory of real-world aspects that must be considered for making high performance devices is discussed, namely loss mechanisms and schemes for device light coupling.

This chapter is written with the goal of developing intuition about electromagnetism in periodic media, and focus will be put on heuristics rather than excessive mathematics. Much of the theory presented is based on the first few chapters of J. D. Joannopoulos [18] which I consider to be an excellent introduction to the theory of photonic crystals. Also, the PhD thesis of W. Bogaerts [19] has been a valuable reference with a more application-oriented approach. Part of this chapter is adapted from the project performed prior to this thesis [3].

2.1. Electromagnetism in Periodic Media

The propagation of light in photonic crystals is governed by Maxwell's equations,

$$\nabla \cdot \mathbf{B} = 0 \tag{2.1}$$

$$\nabla \cdot \mathbf{D} = \rho \tag{2.2}$$

$$\nabla \times \mathbf{E} = -\frac{\partial \mathbf{B}}{\partial t} \tag{2.3}$$

$$\nabla \times \mathbf{H} = \mathbf{J} + \frac{\partial \mathbf{D}}{\partial t}, \tag{2.4}$$

where **E** and **H** are the macroscopic electric and magnetic fields, **D** is the displacement field, **B** is the magnetic induction field, and ρ and **J** are the free charge and current densities. For the sake of simplicity, we impose some restrictions on the media that will be considered.

Firstly, the media are assumed to be homogeneous and time-invariant within regions of the same material, in addition to having no free charges or currents. Furthermore, we restrict ourselves to materials that are linear[1], isotropic and non-dispersive. Linearity means that **D** and **B** are related to **E** and **H** through constitutive relations including only first order terms of the fields, which we express as

$$\mathbf{D}(\mathbf{r}) = \varepsilon_0 \varepsilon \mathbf{E}(\mathbf{r}) \tag{2.5}$$

$$\mathbf{B}(\mathbf{r}) = \mu_0 \mu \mathbf{H}(\mathbf{r}). \tag{2.6}$$

ε_0 and μ_0 are the vacuum permittivity and -permeability, respectively, and ε and μ are the relative permittivity and permeability, which are constant scalars in isotropic and non-dispersive media. Only non-magnetic materials will be considered from here, thus $\mu = 1$. A final restriction is the assumption of transparent media such that ε is both real and positive.

Because Maxwell's equations are linear, it is possible to separate the time dependence from the spatial dependence of the fields by expanding them into a set of harmonic modes. The fields are expressed as a spatial pattern that varies harmonically in time,

$$\mathbf{H}(\mathbf{r}, t) = \mathbf{H}(\mathbf{r}) e^{-i\omega t} \tag{2.7}$$

$$\mathbf{E}(\mathbf{r}, t) = \mathbf{E}(\mathbf{r}) e^{-i\omega t}. \tag{2.8}$$

Notably, the fields are now (for mathematical convenience) expressed as complex-valued functions, and the physical fields will be the real part of these.

When inserting the above two equations into Maxwell's equations (2.1) and (2.2) and applying the medium requirements discussed, we get

$$\nabla \cdot \mathbf{H}(\mathbf{r}) = 0, \qquad \nabla \cdot [\varepsilon(\mathbf{r}) \mathbf{E}(\mathbf{r})] = 0. \tag{2.9}$$

These equations impose important restrictions on the fields that can be interpreted in two intuitive ways. Firstly, they say that there are no point sources or sinks of **H** and **D**. Secondly, by assuming we have a plane wave $\mathbf{H}(\mathbf{r}) = \mathbf{a} \exp(i\mathbf{k} \cdot \mathbf{r})$, Equation (2.9) requires that $\mathbf{a} \cdot \mathbf{k} = 0$. In other words the electromagnetic waves that build up the fields must be transverse, and for that reason we refer to Equation (2.9) as the *transversality requirement.*

By taking the curl of Equation (2.4) and combining with Equation (2.3), we can decouple Maxwell's equations into a wave equation expressed entirely in $\mathbf{H}(\mathbf{r})$:

$$\nabla \times \frac{1}{\varepsilon(\mathbf{r})} \nabla \times \mathbf{H}(\mathbf{r}) = \left(\frac{\omega}{c}\right)^2 \mathbf{H}(\mathbf{r}). \tag{2.10}$$

---

[1] Various non-linear optical phenomena can be enhanced in photonic crystal cavities, making PhCs very interesting in the field of (integrated) non-linear optics [20].

The factor c is the vacuum speed of light defined as $c = 1/\sqrt{\varepsilon_0\mu_0}$. Equation (2.10) will be referred to as the *master equation* since it together with the transversality requirement defines all properties of $\mathbf{H}(\mathbf{r})$.

The observant reader will note that the master equation is an eigenvalue problem, with $\mathbf{H}(\mathbf{r})$ being the eigenfunctions and ω^2/c^2 the eigenvalues. The differential operator on the left hand side will for convenience be gathered into an operator $\hat{\Theta}$ defined as

$$\hat{\Theta} = \nabla \times \frac{1}{\varepsilon(\mathbf{r})}\nabla \times \,. \tag{2.11}$$

Many properties of electromagnetic eigenmodes can be directly understood from the properties of $\hat{\Theta}$. Because the operator is linear, it follows that any linear combination of solutions to the master equation will itself be a solution. Additionally, as derived in Chapter 2 of Joannopoulos [18], $\hat{\Theta}$ is a *Hermitian* operator – just like the Hamiltonian in quantum mechanics.

The definition of an Hermitian operator, $\hat{O}$, is an operator that acts the same to the left and right under the inner product between any two vector fields $\mathbf{F}(\mathbf{r})$ and $\mathbf{G}(\mathbf{r})$. Formally, this can be stated as

$$\langle \mathbf{F}|\hat{O}\mathbf{G}\rangle = \langle \hat{O}\mathbf{F}|\mathbf{G}\rangle, \tag{2.12}$$

where the inner product between two vector fields is

$$\langle \mathbf{F}|\mathbf{G}\rangle = \int \mathbf{F}^*(\mathbf{r}) \cdot \mathbf{G}(\mathbf{r})\, \mathrm{d}^3\mathbf{r}, \tag{2.13}$$

where the “*” denotes complex conjugation.

The fact that $\hat{\Theta}$ is Hermitian allows us to draw important conclusions about $\mathbf{H}(\mathbf{r})$ and the eigenvalues ω^2/c^2 such as mode orthogonality, that the eigenvalues must be real and that the eigenmodes can be obtained by a variational principle, all of which will be discussed in the following.

It is readily found that the eigenvalues of $\hat{\Theta}$ must be real numbers. Assume $\mathbf{H}(\mathbf{r})$ is an eigenmode of $\hat{\Theta}$ with the eigenvalue ω^2/c^2, for convenience denoted λ from here. This means that

$$\hat{\Theta}\mathbf{H} = \lambda\mathbf{H} \qquad \text{and} \qquad \langle \mathbf{H}|\hat{\Theta}\mathbf{H}\rangle = \langle \mathbf{H}|\lambda\mathbf{H}\rangle = \lambda\langle \mathbf{H}|\mathbf{H}\rangle.$$

Since $\hat{\Theta}$ is Hermitian, then

$$\langle \mathbf{H}|\hat{\Theta}\mathbf{H}\rangle = \langle \hat{\Theta}\mathbf{H}|\mathbf{H}\rangle = \langle \lambda\mathbf{H}|\mathbf{H}\rangle = \lambda^*\langle \mathbf{H}|\mathbf{H}\rangle,$$

and since $\langle \mathbf{H}|\mathbf{H}\rangle \neq 0$, we must have $\lambda = \lambda^*$, hence ω^2 is real.

Any two modes $\mathbf{H}_1$ and $\mathbf{H}_2$ having different frequencies ω_1 and ω_2 must have an inner product of zero, enforced by the Hermiticity of $\hat{\Theta}$. A simple proof is given as

$$\omega_1^2\langle \mathbf{H}_1|\mathbf{H}_2\rangle = c^2\langle \mathbf{H}_2|\hat{\Theta}\mathbf{H}_1\rangle = c^2\langle \hat{\Theta}\mathbf{H}_2|\mathbf{H}_1\rangle = \omega_2^2\langle \mathbf{H}_1|\mathbf{H}_2\rangle \tag{2.14}$$

$$\Rightarrow (\omega_1^2 - \omega_2^2)\langle \mathbf{H}_2|\mathbf{H}_1\rangle = 0 \tag{2.15}$$

Since $\omega_1 \neq \omega_2$, the inner product between the modes must be zero, and we say that they are orthogonal. If however the modes have the same frequency, they are not necessarily orthogonal, a case referred to as degeneracy. This occurs e.g. in situations where a crystal is invariant under a particular symmetry operation such as for example a rotation. The requirement of orthogonality for non-degenerate modes explain qualitatively why modes of different frequency typically have a different number of spatial nodes.

Symmetries in Electromagnetic Systems

The various symmetries in a given dielectric structure allow for classification of the supported electromagnetic eigenmodes [18][2]. Photonic crystals can have several types of symmetries, for example rotational symmetry and mirror symmetry. These will be discussed below, after looking at the most important symmetry that is characteristic for photonic crystals – *discrete translational symmetry.*

Discrete translational symmetry means that the crystal is invariant under translations corresponding to some lattice vector $\mathbf{R}$. The concepts of lattice vectors, reciprocal lattices and Brillouin zones are elaborated in Section 2.2, where they are discussed for two-dimensional crystals. More specifically, a PhC has a periodic dielectric function so that $\varepsilon(\mathbf{r}) = \varepsilon(\mathbf{r}+\mathbf{R})$. The dielectric unit that can be considered to be repeated in space is known as a *unit cell.*

As proved by Felix Bloch in 1929, the eigenfunctions of the wave equation for a periodic potential are the product of a plane wave $\exp(i\mathbf{k}\cdot\mathbf{r})$ and a function $\mathbf{u_k}(\mathbf{r})$ having the periodicity of the lattice [21]. Although Bloch's theorem was originally derived for the Schrödinger equation, it also applies for the electromagnetic wave equation, meaning the eigenmodes can be written as

$$\mathbf{H_k}(\mathbf{r}) = \mathbf{u_k}(\mathbf{r})e^{i\mathbf{k}\cdot\mathbf{r}}. \tag{2.16}$$

Eigenfunctions of this form are called *Bloch states*, and the eigenvalues $\omega_n(\mathbf{k})$ form discrete bands that are continuous functions of the Bloch wavevector $\mathbf{k}$. Notably, both ω and $\mathbf{k}$ are conserved quantities, which has the remarkable implication that waves can travel through PhCs without scattering, if assuming an infinite crystal without defects.

Another key property of these eigensolutions is that addition of so-called reciprocal lattice vectors does not change an eigenstate, which is very different

---

[2] A rigorous study of crystal symmetry would fall under the topic of group theory, which is outside the scope of this thesis.

from free-space propagation where all wave vectors represent physically distinct states [18]. Addition of reciprocal lattice vectors is merely a change of label, and results in the same physical mode. The finite zone in reciprocal space in which you cannot get from one part of the zone to another by adding reciprocal lattice vectors is called the (first) *Brillouin Zone* (BZ), and this defines the region in reciprocal space for which one need to calculate the eigenmodes.

By inserting Equation (2.16) into the master equation (2.10), an expression for the periodic function $\mathbf{u_k}(\mathbf{r})$ can be found:

$$\hat{\Theta}\mathbf{H_k} = \left(\frac{\omega(\mathbf{k})}{c}\right)^2 \mathbf{H_k} \tag{2.17}$$

$$\nabla \times \frac{1}{\varepsilon(\mathbf{r})}\nabla \times e^{i\mathbf{k}\cdot\mathbf{r}}\mathbf{u_k}(\mathbf{r}) = \left(\frac{\omega(\mathbf{k})}{c}\right)^2 \mathbf{H}(\mathbf{r}) \tag{2.18}$$

$$\hat{\Theta}_\mathbf{k}\mathbf{u_k}(\mathbf{r}) = \left(\frac{\omega(\mathbf{k})}{c}\right)^2 \mathbf{u_k}(\mathbf{r}), \tag{2.19}$$

where a new Hermitian operator is defined as

$$\hat{\Theta}_\mathbf{k} = (i\mathbf{k} + \nabla) \times \frac{1}{\varepsilon(\mathbf{r})}(i\mathbf{k} + \nabla) \times . \tag{2.20}$$

This form of the master equation is the one that is used for calculating band structures $\omega_n(\mathbf{k})$, which is discussed further in Section 3.1.

In addition to discrete translational symmetry, a crystal might be left invariant after a certain rotation, for example 90° for a square lattice. This is called rotational symmetry, and means in short that if a particular mode satisfies the master equation, so will an appropriately rotated mode. The same applies for reflection and inversion symmetries, and the consequence is that the band structure within the Brillouin zone has a lot of redundancy. An *irreducible* Brillouin zone is the smallest region of the BZ that cannot be further reduced via symmetry operations. This is the region in which the band structures in following sections are calculated, and can for example be seen for a hexagonal lattice in Figure 2.3.

The symmetry that always exists along the third dimension for 2D photonic crystals gives rise to the separation of modes with two uncoupled polarizations [18, Ch. 3]. One polarization has the electric field confined to the xy-plane (E_x, E_y, H_z), and the other has the magnetic field in-plane (H_x, H_y, E_z). Different conventions exist for naming these polarizations, but here we denote the former as *TE polarization* (transverse-electric) and the latter as *TM polarization* (transverse-magnetic).

Scale Invariance and Dimensionless Units

A neat property of Maxwell's equations is that they do not have a fundamental length scale[3]. We say that they are scale invariant, which means that solutions to electromagnetic problems of systems differing only by their spatial scale are related through simple scaling factors.

Consider an eigenmode $\mathbf{H}(\mathbf{r})$ with an eigenfrequency ω in a dielectric environment $\varepsilon(\mathbf{r})$. For a version $\varepsilon(\mathbf{r}')$ of the dielectric function scaled spatially with a factor s, in other words $\varepsilon(\mathbf{r}') = \varepsilon(\mathbf{r}/s)$, it is readily shown from Equation (2.10) that the harmonic eigenmode of the new system is simply the old one scaled spatially with a factor s and with an eigenfrequency scaled by $1/s$. This remarkable property means that, in principle, a given photonic crystal device can be designed to operate at any desired frequency in the electromagnetic spectrum simply by giving it appropriate physical dimensions[4].

The scale invariance allows us to define our system in terms of any fundamental length scale we wish, and a natural choice when dealing with periodic structures is the lattice constant (periodicity) of the system, a. In other words, we define the lattice constant to be 1 and scale all coordinates accordingly. Furthermore, it is useful to express both frequency and wave vectors in dimensionless units so that also these can be calculated for a general dimensionless case and later evaluated for a particular a when a specific physical size is to be considered. These units will be used extensively throughout this report and for that reason the relationships needed to convert physical units (ω, k) into dimensionless ones (ω', k') are stated below:

$$\omega' = \frac{\omega a}{2\pi c} \qquad k' = \frac{ka}{2\pi} \tag{2.21}$$

Another parameter that is defined in a convenient way due to the scale invariance, is the size of band gaps. It is useful to characterize the gap size in terms of the "gap-midgap ratio", $\Delta\omega/\omega_{\mathrm{m}}$. This will be independent of the crystal scale, since both the gap size $(\Delta\omega)$ and the midgap frequency (ω_{m}) will scale by the same factor when scaling a structure.

The Electromagnetic Variational Theorem

A general property of Hermitian eigenproblems is that they have eigenvalues that minimize a variational problem [22]. In the case of electromagnetic eigenvalue problems, the harmonic modes of $\hat{\Theta}$ will be those that minimize the *electromagnetic*

---

[3] This is in contrast to the Schrödinger equation in quantum mechanics which does have a fundamental length scale such that physical properties of differently scaled systems can be very different.

[4] Obvious practical limitations are the feasibility of fabricating the device with the required dimensions as well as wavelength-dependent properties of the materials used.

energy functional, also known as the *Rayleigh quotient*, which is defined as

$$U_f(\mathbf{H}) = \frac{\langle \mathbf{H} | \hat{\Theta} \mathbf{H} \rangle}{\langle \mathbf{H} | \mathbf{H} \rangle}. \tag{2.22}$$

The mode with the smallest eigenvalue ω_0^2/c^2 (the lowest-frequency mode) will correspond to the minimum of U_f over all conceivable field patterns $\mathbf{H}$ that fulfill the transversality requirement. The nth-lowest frequency mode will be that which minimizes U_f within the subspace of field patterns that are orthogonal to all $\mathbf{H}_m$ with $m < n$.

It is possible to rewrite the energy functional in terms of $\mathbf{E}$ instead of $\mathbf{H}$, and the result is [18, Ch. 2]

$$U_f(\mathbf{E}) = \frac{\int |\nabla \times \mathbf{E}(\mathbf{r})|^2 \, \mathrm{d}^3\mathbf{r}}{\int \varepsilon(\mathbf{r}) |\mathbf{E}(\mathbf{r})|^2 \, \mathrm{d}^3\mathbf{r}}. \tag{2.23}$$

This equivalent formulation of the energy functional reveals two important tendencies for the qualitative features of electromagnetic eigenmodes. In order to minimize Equation (2.23), the denominator must be large, and the numerator small. A large denominator is achieved by concentrating the electric field energy in regions of high ε, while the numerator is small if the amount of spatial oscillations in the field pattern is small. These heuristic rules for the modes of $\hat{\Theta}$ will in Section 2.1 and 2.2 help us understand both the origin of band gaps as well as the field distribution of modes in photonic crystals of different kinds.

The variational theorem can not only be used for understanding properties of eigenmodes, it is also a common method for computing them. In this case, it is often called the *variational method*. The method is in short terms based on computing the eigenvalue of some trial eigenmode before one or more parameters of the mode is changed with the goal of minimizing the Rayleigh quotient.

The Physical Origin of Photonic Band Gaps

An intuitive understanding of the origin of photonic band gaps is best obtained by considering the simplest possible periodic structure – a one-dimensional stack of dielectrics with alternating high and low dielectric constant (ε_1 and ε_2). For simplicity, the layers will be assumed to have the same thickness of $a/2$. Two approaches can be followed for analyzing the problem, where the simplest is to consider the sum of multiple reflections and refractions of an incoming plane wave on the stack. Light of certain wavelengths will be completely reflected, if the multiple reflections of the incident wave interfere destructively to eliminate the forward-propagating wave.

A more general approach is to consider dispersion relations and photonic band structures, $\omega_n(\mathbf{k})$, and this will be the method of choice in this project. Assume

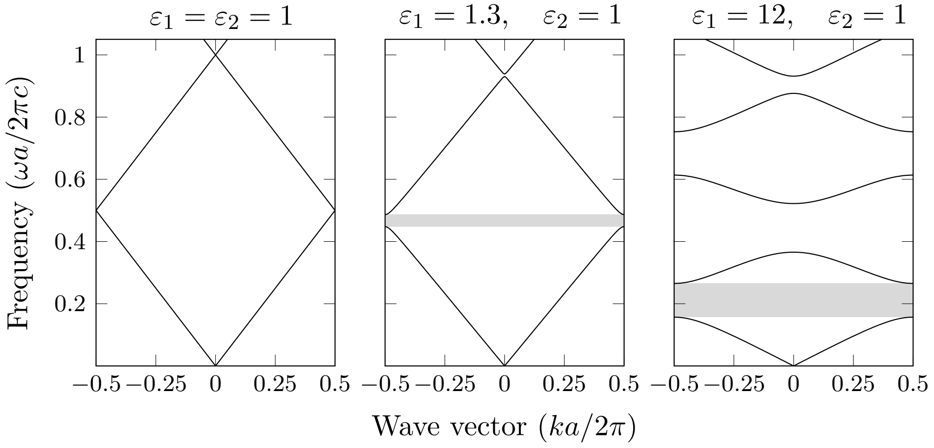

Figure 2.1.: Photonic band structures for dielectric stacks of equally thick layers of different dielectric contrasts. Gray shaded regions indicate photonic band gaps between the lowest two bands. The band structures are computed with the MATLAB®-script in Appendix A of Høvik [23].

to begin with that the dielectric constant of the two materials are equal, and for simplicity it is chosen to be $\varepsilon = 1$. This means that the eigensolutions will be plane waves with a dispersion relation as seen in Figure 2.1 (a), which can be expressed as

$$\omega(k) = \frac{ck}{\sqrt{\varepsilon}}. \tag{2.24}$$

This linear dispersion is referred to as the *light line.* Although there is no actual periodicity in the material when the dielectric constants are equal, we are free to introduce such a fictive periodicity a without changing the physics of the problem. The only consequence is that the band is folded back at the edge of the 1D Brillouin zone.

The effect of introducing a small index contrast between the layers is seen in Figure 2.1 (b). At the edge of the BZ where the eigenfrequencies in the homogeneous medium were the same, a gap arises between the lowest and second lowest band. In this frequency range, k is complex, which means that waves are evanescent and cannot propagate in the crystal. Since no propagating modes exist, this range is called a *photonic band gap.*

The origin of the gap is understood by considering the electric field mode profiles immediately below and above the gap. At the edge of the BZ, the modes are standing waves with a wavelength of $2a$, which matches twice the period of

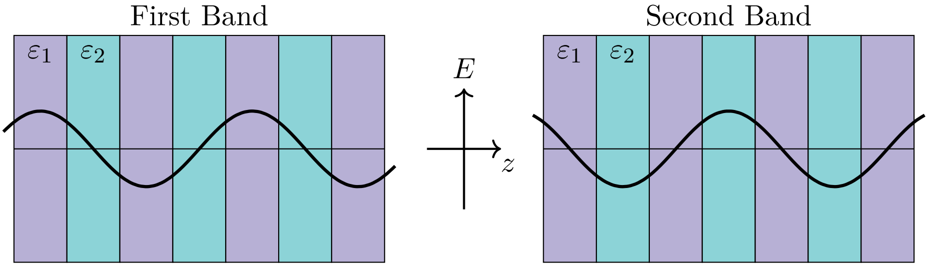

Figure 2.2.: Electric field amplitude of plane waves at the edge of the one-dimensional Brillouin zone for the lowest two bands in Figure 2.1 (b)

the crystal. These modes can be positioned to have their nodes in either the low-ε or high-ε-layers, and any other position would violate the symmetry of the unit cell about its center [18, Ch. 4]. Figure 2.2 shows these two modes superimposed onto the dielectric stack. The first (lowest) band has most of its energy in the high-dielectric constant material (ε_1), while the opposite is true for the second band. Remembering the heuristic from the variational principle that low frequency modes tend to concentrate their energy in high-ε regions, it is understandable why these two modes have a different frequency.

Figure 2.1 (c) shows the band structure for a dielectric stack of much higher dielectric contrast (12:1), and the photonic band gap is observed to increase in size. Gaps between higher lying bands are also present. Also, the light lines are observed to have a smaller slope when the effective index of the system is increased.

2.2. Two-Dimensional Photonic Crystals

A natural extension to the previous discussion of one-dimensional photonic crystals is to consider crystals that have periodicity in two dimensions. Whereas any periodic modulation in $\varepsilon(z)$ leads to a photonic band gap in 1D structures, the situation in 2D and 3D is more complicated. A complete gap can only form if all spatial directions in the crystal support a band gap by the one-dimensional argument, and if these gaps have some mutual frequency-overlap for all **k**-points. To achieve this, one generally needs some minimum refractive index contrast, an appropriate crystal structure and an appropriate distribution of dielectric material on this lattice. The latter two points are briefly discussed below, before we embark on band structures of 2D photonic crystals.

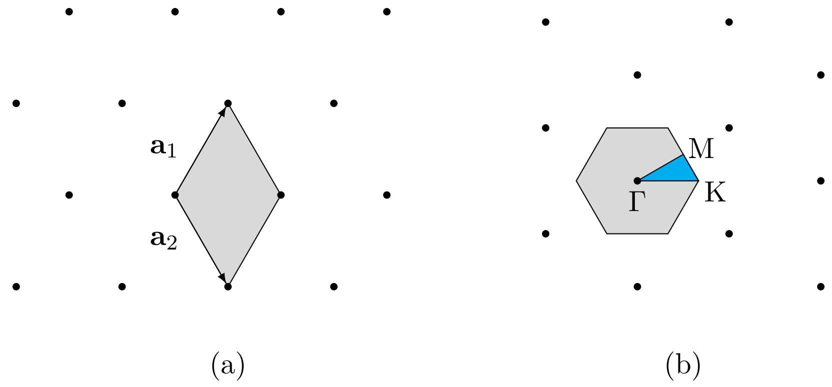

Figure 2.3.: Two-dimensional hexagonal Bravais lattice (a) and its corresponding reciprocal lattice (b). The unit cell is shaded in (a), and the first Brillouin zone in (b). The irreducible BZ is shown in blue.

Two-Dimensional Crystal Structures

Concepts such as Bravais lattices, the reciprocal lattice, and the Brillouin zone will be used extensively throughout this report, and will for that reason be introduced briefly for two-dimensional crystals in the following. The reader is referred to any introductory text about solid state physics for details, for example Kittel [24].

First of all, different ways of periodically repeating identical building blocks give rise to different crystal lattices. The lattice specific to each type is called a *Bravais lattice*, of which there exist five distinct types in two-dimensional crystals [24]. Of these, only the *hexagonal* lattice will be considered in this work, for reasons outlined later. A Bravais lattice is defined by its primitive lattice vectors $\mathbf{a}_1$ and $\mathbf{a}_2$, such that any translation by a linear combination $\mathbf{R}$ of these will translate the lattice onto itself. In other words,

$$\mathbf{R} = n_1\mathbf{a}_1 + n_2\mathbf{a}_2, \tag{2.25}$$

where n_1, n_2 are integers. For the hexagonal lattice, we have $\mathbf{a}_1 = a(\hat{\mathbf{x}} + \sqrt{3}\hat{\mathbf{y}})/2$ and $\mathbf{a}_2 = a(\hat{\mathbf{x}} - \sqrt{3}\hat{\mathbf{y}})/2$, where a is the distance between nearest neighbor lattice points. This lattice is illustrated in Figure 2.3 (a), together with a shaded region that represents the unit cell, which is the area spanned by the primitive lattice vectors.

Suppose now that $f(\mathbf{r})$ is a function that is periodic on the lattice, i.e. $f(\mathbf{r}) = f(\mathbf{r} + \mathbf{R})$. This periodic function can be written as a sum of plane waves of amplitude g and wave vectors $\mathbf{q}$:

$$f(\mathbf{r}) = \int g(\mathbf{q}) e^{i\mathbf{q}\cdot\mathbf{r}} \ \mathrm{d}^3\mathbf{q} \tag{2.26}$$

Since f is periodic, it follows that

$$f(\mathbf{r}+\mathbf{R}) = \int g(\mathbf{q}) e^{i\mathbf{q}\cdot\mathbf{r}} e^{i\mathbf{q}\cdot\mathbf{R}} \ \mathrm{d}^3\mathbf{q} = f(\mathbf{r}) = \int g(\mathbf{q}) e^{i\mathbf{q}\cdot\mathbf{r}} \ \mathrm{d}^3\mathbf{q}, \tag{2.27}$$

which means the Fourier transform g must satisfy $g(\mathbf{q}) = g(\mathbf{q})\exp(i\mathbf{q}\cdot\mathbf{R})$. This is only done if either $g(\mathbf{q}) = 0$ or $\exp(i\mathbf{q}\cdot\mathbf{R}) = 1$. The intuitive interpretation of this is that if a lattice-periodic function is built up of plane waves, only the waves with wave vectors satisfying $\exp(i\mathbf{q}\cdot\mathbf{R}) = 1$ should be included. The vectors $\mathbf{q}$ that satisfy this are called *reciprocal* lattice vectors, and are typically written as $\mathbf{G}$. The set of all possible $\mathbf{G}$ forms a lattice of its own that is called the reciprocal lattice, which is highly important in the study of periodic structures.

As mentioned in Section 2.1, all information about electromagnetic eigenmodes in PhCs is contained within the first Brillouin zone, which is defined as the region in reciprocal space that is closer to one particular reciprocal lattice point than any other. Figure 2.3 (b) shows the reciprocal lattice corresponding to the *direct* lattice in Figure 2.3 (a). The first Brillouin zone is shown as a gray shaded region. Also the irreducible BZ is indicated, which from the sixfold symmetry of the hexagonal lattice becomes a right triangle [19, Ch. 2]. Labels of special high-symmetry points in reciprocal space are included, and it is common to plot band structures of 2D PhCs between these points along the edges of the irreducible BZ, since minima and maxima of a given band almost always occur at the zone edges, and often at corners [18, Ch. 5].

The hexagonal crystal structure is often favored over e.g. square crystals in PhC research due to the possibility of larger band gaps. The high symmetry and near circular Brillouin zone mean that the photonic band gaps arise with nearly the same center frequencies in different crystal directions [19].

In addition to the lattice type, the distribution of dielectric materials on the lattice itself is an important contributor to the properties of photonic crystals. In solid state physics, the building block that is attached to each lattice site is called the *basis*, and one can think of a complete crystal structure as a Bravais lattice multiplied with a basis. As seen from the insets in Figure 2.4, PhC structures can e.g. consist of dielectric rods in air or air holes in a dielectric medium. The geometric shape of the materials that are placed on the lattice is arbitrary, but circles as shown here is the most common choice. One reason for this is that circles have no sharp edges that are difficult to fabricate.

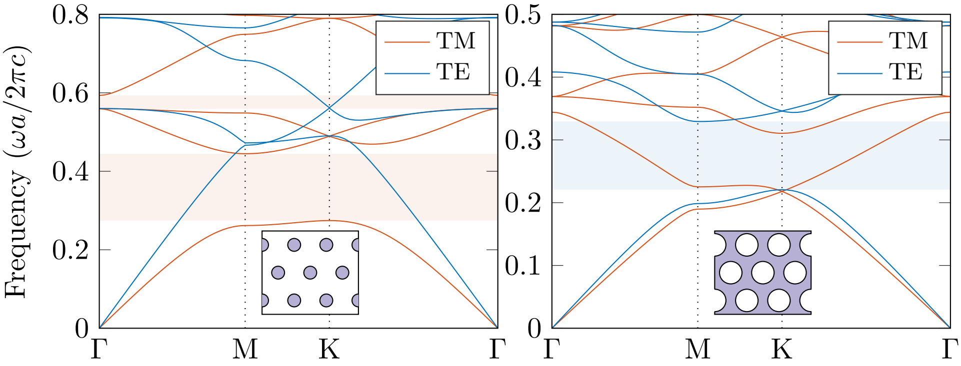

Figure 2.4.: Band structures of 2D hexagonal photonic crystals. Left: dielectric rods with $r = 0.2a$. Right: air holes with $r = 0.35a$. Both simulations used a dielectric contrast of 12:1, and the dielectric functions are shown as insets. Red and blue shaded regions show photonic band gaps for TM and TE-modes, respectively.

Band Structures

Figure 2.4 shows the computed band diagrams of example photonic crystal structures. The band diagrams of the two types of structures are fundamentally different, having band gaps for eigenmodes of opposite polarizations. Crystals with dielectric rods typically have gaps for TM-modes, whereas air-hole structures have TE-gaps. The explanation lies in the boundary conditions of the electric field at material interfaces in combination with whether or not the dielectric material in the crystal is connected. Assuming absence of free charges, the tangential component of the electric field ($E_{||}$) and the normal component of the displacement field ($\varepsilon E_\perp$) must be continuous [25, Ch. 5]. Thus, moving across a dielectric boundary from ε_1 to some $\varepsilon_2 < \varepsilon_1$, the energy density $\varepsilon|\mathbf{E}|^2$ will decrease discontinuously by $\varepsilon_2/\varepsilon_1$ if $\mathbf{E}$ is parallel to the interface ($E_{||}$ continuous), and increase discontinuously by $\varepsilon_1/\varepsilon_2$ if $\mathbf{E}$ is perpendicular to the boundary ($\varepsilon E_\perp$ continuous).

In other words, whenever the electric field lines cross a dielectric boundary, the field energy cannot be strongly confined within the highε material, whereas the opposite is true if the field lines are parallel to a boundary. It is now clear that in order to obtain a large band gap, a dielectric structure should consist of thin, continuous veins along which the electric field lines can run. Then, the lowest bands can be strongly confined, while the upper bands are forced to much higher frequencies because the thin veins cannot support multiple modes. Returning to the band diagrams in Figure 2.4, this heuristic is observed in practice. For the dielectric rods, TM-fields experience the rods as thin, continuous veins along **E**, but the TE-fields see a discontinuous distribution of high-ε material. The opposite is true for the structure with air holes in a high-ε material.

2.3. Photonic Crystal Slabs

The two-dimensional crystals considered above were assumed invariant in the third dimension, meaning they are of limited use for practical purposes. A key application of photonic crystals is for confinement of light in all directions, and although structures having periodicity (and thus photonic band gaps) in all three dimensions can be realized, the fabrication is highly complex and limited to simple structures [18, Ch. 7].

A particularly attractive type of structure called *slab photonic crystal* is obtained by combining 2D in-plane periodicity with a slab waveguide in the vertical direction. Illustrations of slab photonic crystals are shown in Figure 2.5, where linear defect waveguides are depicted. Waves in PhC slabs are confined in-plane via photonic band gaps arising from the 2D periodicity, and vertically via *index guiding*, which is a generalization of total internal reflection. These structures are readily fabricated using standard nanofabrication techniques by growing or depositing thin films, defining a pattern with lithography and etching it into the slab [19, Ch. 2], giving them high potential in a number of application areas.

Although the in-plane periodicity of PhC slabs results in properties that in many ways are analogous to 2D PhCs, the finite thickness introduces qualitatively different behavior. Notably, whereas the in-plane Bloch wave vector $\mathbf{k}_{||}$ is a conserved quantity due to the 2D discrete translational symmetry, the vertical wave vector $\mathbf{k}_z$ is not. Thus, it is useful to consider so-called projected band structures, where the states in the surrounding material are plotted versus their in-plane wave vector components. An example projected band structure for a hexagonal hole slab of thickness $h = 0.5a$ has been simulated and can be seen in Figure 2.6. If the slab is for example suspended in air, the eigensolutions are

$$\omega = c|\mathbf{k}| = c\sqrt{k_{||}^2 + k_z^2}. \tag{2.28}$$

It is clear from Equation (2.28) that modes having $\omega \leq c|\mathbf{k}_{||}|$ have imaginary k_z, which means they decay exponentially away from the slab. Such fields are termed evanescent [25]. Modes above the light line will on the other hand have real out-of-plane wave vectors such that they can extend infinitely into surrounding medium. When plotting the projected band structure, a continuum of modes arise above the line $\omega \geq c|\mathbf{k}_{||}|$ which is referred to as the *light cone*. Only bands inside

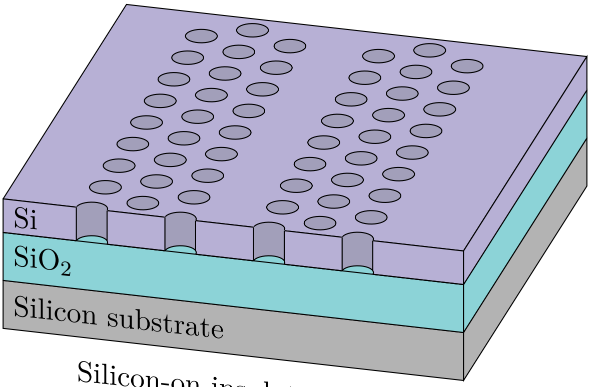

Silicon-on-insulator PhC

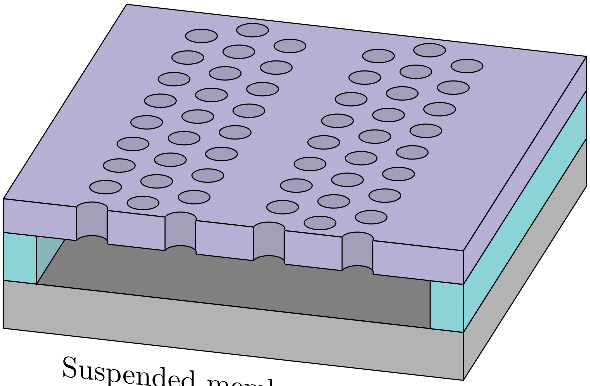

Suspended membrane PhC

Figure 2.5.: Illustration of two types of photonic crystals slabs, here in form of missing-hole waveguides. Top: silicon-on-insulator, bottom: suspended silicon membrane, also called “air-bridge PhC”.

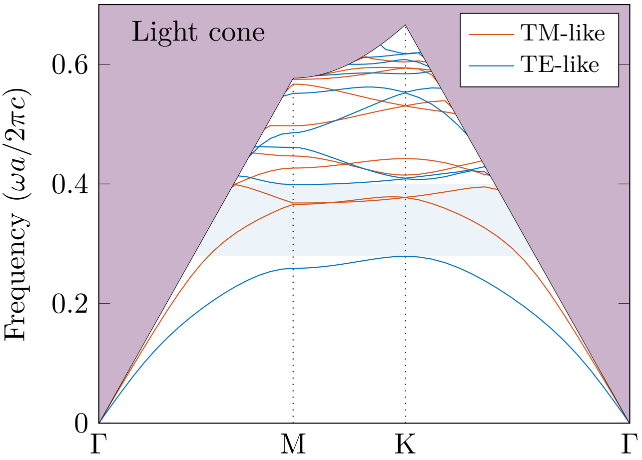

Figure 2.6.: Projected band structure for a hexagonal hole slab with $r = 0.35a$, thickness $h = 0.5a$ and a dielectric contrast of 12:1. The purple shaded area is the light cone, and the blue shaded area shows a band gap for TE-like modes.

this continuum can couple to vertically radiating modes. For that reason, such modes are referred to as *resonant* or *leaky*, in contrast to the *guided* modes below the light line which cannot couple to the radiation continuum unless the in-plane periodicity is broken [19, Ch. 2]. Since there are leaky modes at all frequencies, there are no true band gaps in PhC slabs. The gaps are incomplete since they refer to only guided modes below the light line.

The lack of translational symmetry in the vertical direction also means that eigenmodes in slabs cannot be classified as purely TM or TE polarized, as done for 2D PhCs. Instead, the eigenmodes can be classified after their parity with respect to the $z = 0$ plane intersecting the slab center. This is defined as the expectation value of the mirror-flip operation through $z = 0$. A vertically symmetric slab such as the air-bridge shown in the bottom of Figure 2.5 support non-interacting true even and odd eigenstates with parities of 1 and -1, respectively[5], which are referred to as TE- and TM-like modes from the strong similarities to their 2D counterparts. The symmetry breaking substrate as seen in the upper part of Figure 2.5 gives rise to eigenmodes that no longer are truly even or odd, but will have a hybrid character [26]. Since photonic band gaps normally only occur for one type of polarization, the mode mixing between vertically even and odd modes is an important loss channel in these structures, as elaborated in Section 2.6.

---

[5] The suspended membrane can be considered vertically symmetric since the mirror symmetry must only be preserved where the guided modes have non-negligible field amplitudes [26].

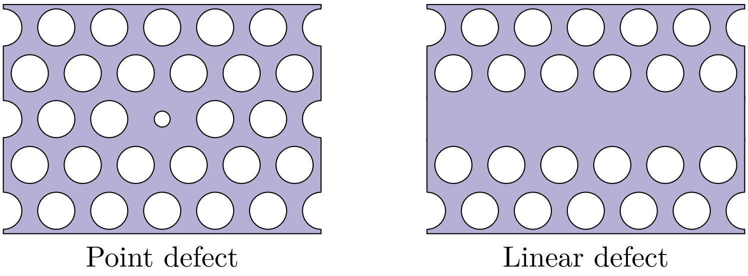

Figure 2.7.: Examples of defects in photonic crystals.

2.4. Defects in Photonic Crystals

In the same way that doping of semiconductor crystals changes their electronic properties, introducing defects of different kinds to photonic crystals gives rise to fundamentally new behavior. In fact, most of the interesting applications suggested for PhCs are somehow related to the introduction of defects. Whereas semiconductors are doped by changing the local electronic potential of an otherwise periodic crystal, photonic crystals are doped by locally altering the dielectric function $\varepsilon(\mathbf{r})$, and examples of possible alterations are shown in Figure 2.7.

Generally, the intended outcome from introducing crystal defects is the creation of states inside the photonic band gap, causing the modes supported by the defects to be localized since no extended states exist inside the band gap. The fact that the dimensions of PhC features are comparable to optical wavelengths means that conventional nanofabrication allows for designing and fine-tuning the properties of such defects. The possibilities are endless, and this flexibility has no analogous counterpart in the field of tuning electronic properties of semiconductors.

Point Defects and Localization of Light

The simplest types of defects one can imagine in a PhC are those formed by altering the dielectric function around a single lattice point, hence “point defect”. Examples of possible alterations are to remove or change the size of one or more rods or holes. By perturbing a lattice site, one or more modes can be created with frequencies inside the band gap [18, Ch. 5]. Since the state(s) lies inside the band gap, the mode(s) is evanescent and decays exponentially away from the defect. One instructive way to understand point defects is as cavities surrounded by highly reflective omnidirectional dielectric mirrors. If the cavity is such that it supports a mode with a frequency inside the band gap, resonators with very high Q-factors can be realized.

Photonic crystal point defects have numerous applications in integrated optics related to e.g. high efficiency lasers [27], controlling spontaneous emission, enhanced non-linear interactions [20] and narrow-bandwidth filters [28]. Also, resonant microcavities in PhCs have been widely studied for use in biosensors [29, 14, 15] based on spectral shifts of defect-cavity resonances.

Linear Defects and Waveguides

Whereas point defects in photonic crystals can be used to trap light, linear defects created by modifying a linear sequence of unit cells are able to guide light from one location to another. The particular example shown in Figure 2.7 of removing a single row of holes is called a “W1” defect, which is a commonly used PhC waveguide implementation. If the defect is made to support a mode with a frequency inside the band gap, the light will be confined to the defect and can only propagate along it.

The mechanism for PhC-based waveguiding is fundamentally different from that in conventional dielectric waveguides, which is based on total internal reflection, or *index guiding*. It is instead the photonic band gap that is responsible for confining the light to the waveguide, through a mechanism referred to as *gap-guiding*. A remarkable property of gap guiding is the ability to guide light confined mostly to a low-index material, whereas conventional waveguides require the light to be confined to the high-index material. Note that in PhCs, the two guiding mechanisms can coexist [30]. Index guided modes can exist in PhCs if waveguides are formed as regions with higher average ε than the surrounding medium. Such modes lie below the extended modes of the crystal.

The introduction of a line defect in PhCs induces symmetry breaking, and translational symmetry only remains in the direction parallel to the defect. This means that the new Brillouin zone is one-dimensional, and the corresponding band structure is found by projecting the k-vectors of the original 2D band structure onto the translational symmetry direction of the defect [30]. The projection of bands of the bulk PhC generally results in the formation of continua of extended bulk states, inside which the defect modes are not localized and thus not guided. In hexagonal PhCs, linear defects are typically formed by altering the crystal along a line in the Γ-K direction, and an example projected band structure for this system can be found in Figure 5.3 in the results-chapter.

Bends and Beam Splitters

Guiding of light generally extends beyond the linear case, and the ability to guide waves around sharp corners with high efficiency is crucial for realizing high density integrated optics. Conventional waveguides relying on total internal reflection for waveguiding must be smooth with respect to the wavelength of light, which severely limits the degree of miniaturization possible. On the other side, gap-guided modes in PhCs are forbidden to escape into the crystal, regardless of how sharp a bend is made. Once light is propagating in a waveguide, it has no other way to go than along it, being either transmitted or reflected at the bend.

A key challenge when designing bends and splitters lies in maximizing transmission and eliminating back-reflections [19]. Clever ways of local junction structuring have made it possible to achieve high and broadband transmission at selectable frequencies [31, 32, 33, 34, 35], which will also be investigated later in this report.

Since components such as bends and splitters break the translational symmetry along linear defect waveguides, $\mathbf{k}$ is no longer a conserved quantity. This means that modes inside the light cone for slab structures can be excited which results in power leakage into the claddings. If there also exist other guided modes at the same frequency, these can be excited. Such mode coupling is usually undesirable, which is an important reason for designing waveguides to be single mode at the intended operating frequency.

2.5. Biosensing

Biosensing in its broadest sense refers to the process of transforming a physical or chemical quantity associated with some kind of biological system into a measurable signal. Several different signal transduction methods exist, and the most common are based on optical, electrochemical or mass-related transduction [36, Ch. 6]. Within optical techniques one can further distinguish between *label-free* detection and *fluorescence*-based detection [17]. The former has the key advantage of not relying on labelling or altering the target molecules, which means that they are detected in their natural form. The small size of photonic crystal sensors means that very small amounts of sample volume is needed for obtaining adequate detection signals. For example, Lee et al. [14] and Dorfner et al. [15] demonstrate detection of target molecules in quantities as low as a few femtograms.

Biomolecules can alter the optical properties of a sensor in many ways, but the focus here will be on changes in refractive index on a sensor surface caused by specific absorption and build-up of target biomolecules. The theory of surface immobilization and biorecognition is rich, and only basic concepts are explained here. As seen in Figure 2.8, biorecognition molecules (antibodies) are immobilized onto the sensor surface. Depending on the hole sizes, it can be challenging to functionalize the inner walls with antibodies, but this is not considered in this theoretical treatment. When target biomolecules (antigens) are added to the system, they can bind selectively to the antibodies through what is known as a “lock and key”-fit. The specificity of the binding is dictated by the particular molecules in question, and is based on characteristics such as size, geometric conformation and active chemical functional groups [36, Ch. 6].

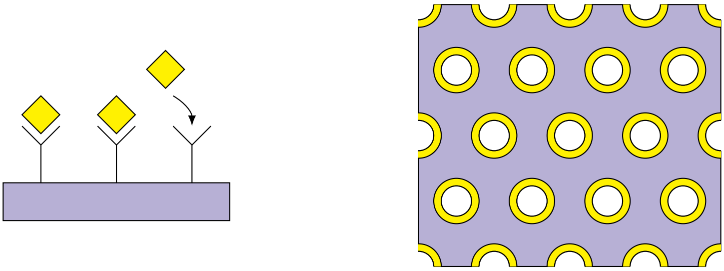

Figure 2.8.: Specific binding of target biomolecules (yellow) to bioreceptors that are immobilized onto the side walls of a photonic crystal slab.

Since the biomolecules generally have a different refractive index than the surroundings (buffer solution or air), the refractive index in close vicinity to the surface is modified by the addition of a biolayer. In the case of a photonic crystal, the change in dielectric environment results in shifts in for example the spectral position of a defect mode. If we consider a system of a slab photonic crystal with air holes as seen in Figure 2.8, the addition of a layer of protein ($n \approx 1.5$) is expected to result in a redshift of spectral resonances since the effective refractive index increases. An alternative transduction principle that will be investigated in this project is the change in optical path length that follows from the change in effective refractive index in one of two arms in an interferometer.

Mach-Zehnder Interferometer

The configuration of the PhC biosensor investigated in this project will be an integrated Mach-Zehnder interferometer (MZI). Previous reports of MZI-implementations in photonic crystal exist, both in theoretical studies [37, 38, 39, 40] and experimental [41]. However, no reports of such fabricated structures used for biosensing applications have been found. Also, most of the theoretical studies consider PhC rod-structures which are much more difficult to fabricate than hole-slabs. Parts of the discussion below is inspired by the rib waveguide MZI-biosensor in Prieto et al. [42] which considers many of the same sensor concepts although it is not implemented on a PhC-platform.

A suggested implementation of a MZI in a hexagonal PhC is shown in Figure 2.9, where it is formed by combining linear waveguide segments, Y-junctions, and 60°

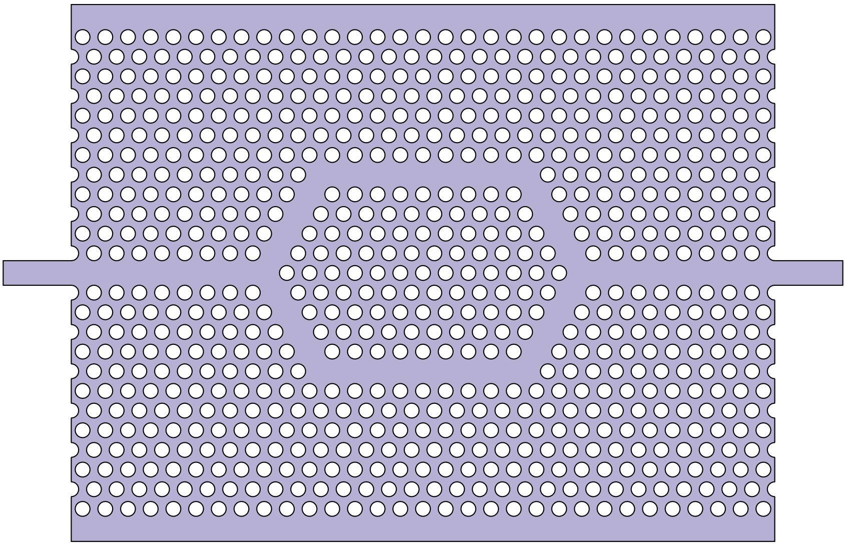

Figure 2.9.: A possible implementation of a photonic crystal Mach-Zehnder Interferometer.

bends. Light is coupled into the structure at one side, and split into two arms that after a certain distance are combined to a single output waveguide from which the output intensity can be measured.

One arm in the interferometer serves as the *sensing* arm and the other as a *reference*. If the effective refractive index of the sensing arm is changed due to e.g. the discussed build-up of biolayers, light traveling in this arm will experience a phase shift ϕ relative to the light in the reference arm. The result is a modulated output intensity I according to

$$I \propto (1 + V \cos\phi). \tag{2.29}$$

The parameter V is called the visibility [25, Ch. 11], and gives the contrast of the interference signal. This will depend on the coupling factor of the junctions as well as possible propagation losses in the interferometer arms. Ideally, the visibility is unity, which requires Y-junctions with a coupling factor of 3 dB in addition to matched losses in the two arms [42]. The phase shift between light in the arms can further be written as

$$\phi = \frac{2\pi}{\lambda} L \Delta n_{\mathrm{eff}}, \tag{2.30}$$

where L is the length of the sensing region and Δn_{eff} is the change in effective index of the sensor arm caused by the biolayer. The output intensity is in other words expected to oscillate when gradually thicker biolayers are added. It is also clear that a larger L gives a more sensitive MZI because it results in larger phase shifts for a given change in n_{eff}. The effective index change that will follow from a particular change in surface dielectric environment will depend on the power fraction of the light that penetrates into the PhC holes surrounding the waveguides.

Much work has been done on investigating photonic crystals for biosensing applications, but primarily related to detection of spectral shifts of resonances in microcavities of different kinds. Such sensors are inherently susceptible to drift and noise caused by for example temperature fluctuations, resulting in refractive index fluctuations (thermo-optic effect) and thermal expansion (thermo-mechanical effect) in both the buffer solution and the sensor itself [17]. The working principle of symmetric or *balanced* interferometers results in an intrinsic reduction of such noise because changes in the sensing arm are canceled from the same change occurring in the reference arm. Thus, the need for temperature controllers and/or solvents having particular thermo-optic coefficients vanishes.

A practical concern regarding fabrication of the suggested device is how to isolate the reference and sensing arms. One suggested method is to cover the whole fabricated PhC slab with SiO_2 except in the region of the sensing arm, as demonstrated for the rib waveguide MZIs [42]. However, this would make the interferometer unbalanced. Alternatively, both arms can be exposed to the test solution if only the sensing arm is functionalized with bioreceptors. A key advantage of this procedure is cancellation of common-mode noise terms related to changes in buffer refractive index and non-specific adsorption since the same buffer is present in both arms [17]. Local immobilization of biorecognition molecules onto specific sensor regions appear as no trivial task, but can be possible e.g. using photo-cleavable linker-molecules [43] or with direct inkjet printing of the desired chemicals [44].

2.6. Loss Mechanisms

There are several mechanisms responsible for loss of optical power in photonic crystals and nanophotonic devices in general. Some are fundamental in that they occur even for ideal devices, others originate from non-ideal fabrication or material properties. Inspired by the discussion in Sparacin [45, Ch. 4], a compact summary of various mechanisms is given below where losses are categorized as either originating from the design or from fabrication.

Design Losses

A number of losses originate from fundamental mechanisms that can be attributed to the design of a device. Depending on the structure, such losses can be unavoidable.

- For slab PhCs, coupling to radiation modes of the cladding can occur for modes that lie inside the light cone [26], or whenever the translational symmetry of a guided mode is broken.
- For vertically asymmetric slab structures such as silicon-on-insulator PhC waveguides, localized TE-like modes can couple to TM-like modes which are extended in the plane of periodicity [19, Ch. 4].
- Power can be reflected at junctions such as bends and beam splitters [19, Ch. 3].

Material and Disorder Losses

In practice, the losses in fabricated devices are dominated by disorder introduced from fabrication, or from intrinsic optical properties of the material used. Fabrication disorder can be introduced through both lithography and etch processes [46].

- Bulk material absorption (possibly also two-photon absorption) occur in all devices, and depend largely on the material type and quality. For SOI devices, monocrystalline silicon is preferred, although hydrogenated amorphous silicon can be used [47], see also Section 3.2.2.
- The surface roughness is a negligible loss contributor for near atomically flat monocrystalline SOI wafers [48], but can introduce losses in amorphous silicon films.
- Sidewall roughness which is introduced on sidewalls during fabrication (lithography, etching) is often the dominating loss mechanism for TE-modes in high index contrast strip SOI waveguides [49, Ch. 4].
- Slanted sidewalls will break the vertical symmetry and enhance coupling between TE and TM modes, both in strip waveguides [45, Ch. 4] and PhC waveguides [50].
- Disorder in position, shape [51] and size [52] of PhC holes can all contribute to losses.

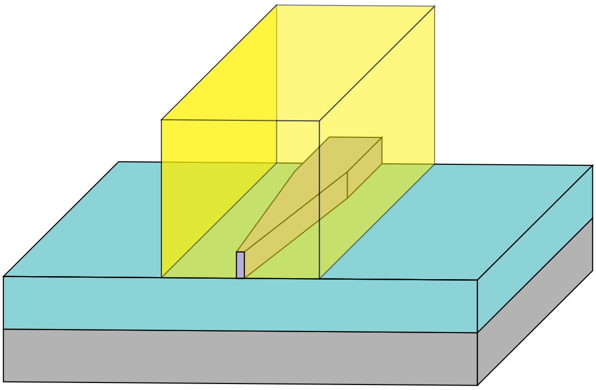

Figure 2.10.: Schematic of the edge facet of an inverted silicon taper covered with a polymer waveguide.

2.7. Fiber-to-Waveguide Light Coupling

The *insertion loss* is the total loss that occurs between insertion and extraction of light from an optical device [45]. In addition to the mechanisms discussed in Section 2.6 which covers losses occurring in the device itself, considerable amount of power can be lost in the process of interfacing the device with external optics, often fibers. In fact, the coupling efficiency from butt-coupling single mode fibers (core diameter ∼9 µm) to typical strip waveguides ($450 \times 220\,\mathrm{nm}^2$) is of the order of 0.1 % [19, Ch. 3], due to the large mismatch in mode size.

Various techniques exist for improving this efficiency. A detailed overview of different methods used for efficient light coupling can be found in Vivien et al. [53, Ch. 3]. The simplest of all are based on *adiabatic* mode size conversion, i.e. slowly expanding the size of a waveguide core until the mode size matches that of a fiber. Such waveguide tapering is readily achieved in-plane by lithographic patterning, but the vertical fiber-slab mismatch remains. Ideally, 3D tapering is used, but this is challenging to achieve with conventional planar processing technologies.

An alternative adiabatic approach of *inverted tapering* is often used, where the silicon waveguide core is narrowed down into a sharp tip overlaid with a lower index waveguide, typically of some polymer material. Figure 2.10 shows a schematic of an inverted taper. The taper causes the mode to expand since it cannot be confined in the narrow core, while the polymer waveguide takes over the light confinement [53]. Losses below 1 dB per coupler over large bandwidths is achievable with inverted tapers [54], and misalignment tolerances are relaxed considerably relative to direct butt-coupling [55].

Chapter 3.

Simulation and Fabrication Methods

This chapter describes the methods and tools that are used in this Master's project – both for computer simulations and for fabrication and characterization. In-depth descriptions of each method are not given since the simulations, fabrication and characterization processes needed for making photonic crystal structures requires a number of different methods and instruments too large for a rigorous discussion of each. Instead, the equipment is described with a level of detail sufficient for understanding the working principles and properties that will be brought forth in arguments and discussions in following chapters.

3.1. Computational Electromagnetism

Computational electromagnetism is the process of computationally approximating Maxwell's equations to model the interaction of electromagnetic fields with some physical environment. In parallel with the last decades of advances in computer science, computational methods have become increasingly valuable tools in photonics research [18]. Computers can be used as a platform where optical structures such as photonic crystals are designed, simulated and optimized before they are fabricated, often with a high degree of consistency between simulation results and experiments.

A general understanding of different methods for analyzing electromagnetic problems is necessary for realizing their advantages and limitations and thus for correct interpretation of simulation results. This section considers therefore computational photonics in general, and descriptions of the specific simulation software used in this project can be found in Appendix A and B. The following brief overview of common numerical techniques for solving Maxwell's equations is based on that in Appendix D of Joannopoulos [18].

3.1.1. Method Classifications

Problems in computational photonics will typically belong to one of three categories [18]: frequency-domain eigenproblems, time-domain simulations or frequency-domain responses. Each category of methods have their distinct characteristics and limitations, which are outlined below. The former two of the methods will be used in this project, and will for that reason be considered more in-depth.

Frequency-Domain Eigenproblems

Band structures $\omega(\mathbf{k})$ and associated field patterns are found by expressing the problem in Equation (2.19) as a finite matrix eigenproblem and using linear algebra techniques to find the first few eigenvectors and -values. In periodic dielectric media, the Bloch envelope of the magnetic field, $\mathbf{u}_{\mathbf{k}}(\mathbf{r})$, is periodic such the computation need only be done over the finite unit cell. This means that frequency-domain eigenproblems are powerful computational methods for finding band structures and eigenfields of photonic crystals.

Several methods are possible for reducing the number of unknowns in the eigenequations from infinite to a finite number, N. One common way of discretizing this kind of eigenproblem is by using a plane-wave expansion. Any reasonable periodic function can be represented as an infinite sum of sines and cosines (Fourier series). By truncating the sum to have N terms, the approximate periodic function can be found by solving a set of linear equations with N unknowns. Although it is straightforward to solve for all the corresponding eigenvectors and -values on a computer, it is typically too resource intensive for practical purposes because N can be very large. Alternatively, it is possible to solve for only the smallest few eigenvalues and eigenvectors using iterative methods. An example of such methods is based on the variational theorem and iterative minimization of the Rayleigh quotient in Equation (2.22). Since the smallest eigenvalues and low order eigenmodes normally are the ones of greatest interest, iterative techniques are commonly employed. This is also the case in the software used for band structure computations in this project, see Section 4.1.1.

For frequency-domain eigenproblems one cannot directly analyze properties such as transmission spectra for finite structures, since such information cannot be directly deduced from band diagrams. However, information about band gaps and eigenmodes are crucial for understanding and interpreting the features of such spectra, which renders frequency-domain eigenproblems highly valuable when used in combination with e.g. time-domain simulations.

Time-Domain Simulations

The most general numerical methods of computational photonics is arguably those that simulate the full time-dependent Maxwell's equations by evolving them over time in some finite computational region [18]. Usually starting with some time-dependent current source $\mathbf{J}(\mathbf{r}, t)$, the fields $\mathbf{E}(\mathbf{r}, t)$ and $\mathbf{H}(\mathbf{r}, t)$ are propagated in time in what essentially can be thought of as a numerical experiment.

A key advantage of time-domain simulations is that they in contrast to frequency-domain methods inherently support both non-linear behavior and broadband sources. The latter means that by simulating the response of the system to temporally short pulses, a single simulation can yield both transmission spectra and information about resonant modes over a wide spectrum of frequencies. The main disadvantage of time-domain methods is the difficulty of resolving sharp spectral features and the requirement of a smooth "turn-on" of sources when steady-state responses are desired. In both cases, the simulations must be run for a large number of time-steps, and frequency-domain methods can often be more efficient for solving such problems.

One specific and commonly used technique for time-domain simulations is the finite-difference time-domain (FDTD)-method, which is further discussed in Section 3.1.3.

Frequency-Domain Responses

These techniques are based on finding the fields $\mathbf{E}(\mathbf{r})e^{-i\omega t}$ and $\mathbf{H}(\mathbf{r})e^{-i\omega t}$ that arise in response to some current source of *constant* frequency, $\mathbf{J}(\mathbf{r})e^{-i\omega t}$. Useful physical quantities such as transmission and reflection through a finite structure at specific frequencies can be determined using this method. By including currents in Maxwell's equations, the following linear equation can be found [18]:

$$\left((\nabla \times \nabla \times) - \frac{\omega^2}{c^2}\varepsilon(\mathbf{r}) \right) \mathbf{E}(\mathbf{r}) = i\omega\mu_0 \mathbf{J}(\mathbf{r}). \tag{3.1}$$

By discretizing this equation into N unknowns, an $N \times N$ matrix equation emerges which can be solved for the unknown fields directly or by using iterative methods. Spatial discretization techniques such as the finite element method are possible to use with frequency-domain responses, which can be powerful since the density of mesh elements can be varied in the simulation space depending on the physics and complexity of the geometry. However, spectral responses require time consuming separate simulations at all desired frequencies. In this project, FDTD-simulations have been found to run faster and with less computer memory in the majority of the simulations of the considered photonic crystal devices, making it the method of choice for simulating finite structures.

3.1.2. Simulating Finite Structures

When considering real optical devices, it is normally desirable to simulate the optical properties of *finite* structures. In practice, this means that the computational region must be truncated, and a common technique that is used for both time-domain methods and frequency-domain responses is a *perfectly matched layer* (PML). In short, this is an artificial absorbing layer that is placed around the edges of the computational region which ensures that there are no reflections from the edge of the material.

Ideal reflectionless PMLs are however only the case when used in combination with the exact wave-equation, and numerical reflections must be accounted for in practice when the problem is approximated through discretization [56]. Furthermore, even in the limit of infinite resolution, PMLs have been shown to fail to be reflectionless in a number of cases such as for periodic dielectrics (photonic crystals) [57], waveguides at oblique incidence [58] and for left-handed media [59]. Different workarounds exist for photonic crystal structures such as not extending the crystal into the PML at all, see e.g. Figure 4.4.

Finite structures cannot be directly simulated from frequency dependent eigenproblems if periodic boundary conditions are used. It is however possible to calculate eigenmodes of simple non-periodic defects in photonic crystals using *supercell approximations* [18, 60], provided that the modes are localized. This works by surrounding the defect by a large computational cell which is periodically repeated in space. When the size of the cell is increased, the solution will converge exponentially towards that of the isolated defect, since the modes themselves decay exponentially away from the defect and thus do not feel the fictive periodicity.

3.1.3. The Finite-Difference Time-Domain Method

The finite-difference time-domain (FDTD) method is a widely used grid-based differential numerical modeling method for problems in electromagnetics [61, 62]. In short, the method consists of dividing space into a discrete grid and evolving the electric- and magnetic fields in time in discrete time steps. Both the spatial and temporal derivatives that appear in Maxwell's equations are approximated by finite differences using central-difference approximations, which become a closer approximation to the continuous equations as the spatial and temporal resolution are made finer. Specifically, the central difference approximation results in second-order accuracy such that an increase in resolution by a factor of 10 gives a reduced error in the approximation by a factor of 100 [62, Ch. 3]. A rule of thumb is that the grid size should maximum be one tenth of the wavelength of light in the medium with highest refractive index, and not larger than the smallest feature of the simulated structure [63].

Commonly, FDTD-implementations store different field components for different grid locations on a staggered grid that is known as a *Yee-lattice* [64]. The fields **E** and **H** are positioned on a rectangular Cartesian grid such that each field component is positioned midway between field components of the other type. During time-stepping, different information such as various field components can be stored and give rise to flux spectra, field profiles and energy density distributions. The computational domain can be truncated in many different ways such as with periodic boundary conditions or perfect electric/magnetic conductors. The latter are normally used in combination with perfectly matched layers to prevent artificial reflections from the edges of the simulation domain.

FDTD is mainly suitable for systems having characteristic dimensions that are too large for quasi-static approximations to be made, but too small for beam envelope approximations [62, Ch. 3]. Typical dimensions of photonic crystal components fall in this range, making FDTD a useful and commonly employed numerical analysis tool. A disadvantage of the FDTD method is that it is highly resource intensive, requiring large amounts of computer time and memory. For this reason, it is common to do 2D and 3D simulations in combination using *effective index methods* as discussed in the next section. The initial optimization of different structural parameters can be done in 2D, while the simulations of the optimized system can be done in 3D for better quantitative results.

For further information on the FDTD method, see e.g. Taflove [61]. A number of technical aspects to consider when performing FDTD-simulations with an example software can be found in Section 4.1.2 and Appendix B.

3.1.4. Effective Index Approximations

Proper theoretical modeling of PhC slab-structures with 2D periodicity requires fully vectorial 3D calculations that are extremely demanding in terms of time and memory requirements. Approximate calculations of the same structure can be done by replacing the slab with a 2D system where the background dielectric medium has the effective refractive index of the fundamental guided mode of the slab system [65, 66].

In this project, the effective index of the SOI-slab silicon in the following 2D simulations is set to $n_{\text{eff}} = 2.87$, based on a COMSOL Multiphysics mode analysis performed in a preliminary project preceding this work [3].

The validity of the effective index method is higher for weakly confining structures like those found in material systems of low vertical index contrast (e.g. InP/GaInAsP/InP) than for high index contrast systems like silicon-on-insulator. In high contrast systems, the method is still valid, only over much narrower frequency ranges [66]. This means that quantitative values for the frequencies of eigenmodes or spectral position of features in transmission spectra must be expected to deviate between 3D simulations and 2D approximations. Qualitatively, such features have nevertheless in many cases been found to be similar in 2D and 3D simulations [67, 68].

The behavior of real-world slab PhCs is as discussed in Section 2.3 fundamentally different from their 2D counterparts, for example in terms of having additional loss channels. This means that although many qualitative optical properties of

PhC slabs can be simulated in 2D, full 3D simulations should always be used for validating result [19, Ch. 2].

3.2. Fabrication

The instruments and materials used for fabrication of silicon photonic crystal structures and polymer waveguides used for fiber-chip light coupling are presented in this section. Trivial instruments such as hotplates, ultrasonic baths and spin coaters are not discussed since their functionality do not affect the way the fabrication processes in this project are performed and developed.

3.2.1. The Silicon-on-Insulator Material System

Silicon-on-insulator (SOI) has in the last decade become an attractive material platform for use in compact photonic devices. Three important reasons for this can be pointed out [10, Ch. 13]. Firstly, crystalline silicon (c-Si) has good optical quality with low absorption above 1200 nm. Secondly, the refractive index contrast between Si and SiO_2 is high and thus allows for strong light confinement and dense component integration. Finally, compatibility with the mature CMOS manufacturing process opens up for mass-production of integrated photonics.

A schematic of the SOI material system is seen in Figure 2.5, and the relevant refractive indices can be found in Table 4.1. A conventional thickness of the silicon membrane is 220 nm, since this thickness only supports a single slab mode for each polarization (TE and TM) at $\lambda = 1550\,\mathrm{nm}$ [10, Ch. 13]. The thickness of the SiO_2 cladding layer depends on the degree of mode confinement in the silicon slab. Generally, TE modes are highly confined and a cladding of $\sim$1 µm thickness is sufficient to avoid substrate leakage, while TM modes require typically 2-3 µm cladding.

The main disadvantages of the SOI system is that silicon cannot be used for conventional light generation since it is an indirect bandgap semiconductor. Furthermore, although the high index contrast allows for dense circuitry, it also causes large scattering losses from fabrication induced roughness, notably from that on etched sidewalls [69]. Finally, crystalline SOI wafers are costly due to a challenging manufacturing process, where the typical procedure involves wafer bonding [10, Ch. 13].

The high cost of SOI wafers has made an alternative material system attractive, where the top silicon layer is substituted by amorphous silicon (a-Si). This layer can be grown onto (cheap) thermally oxidized silicon wafers using e.g. PECVD, or the oxide can be grown with PECVD as well. A brief comparative discussion of the material properties of c-Si and a-Si is given in Section 3.2.2.

PECVD-grown amorphous silicon is the material of choice in this project since it lowers the fabrication development costs. This is a common procedure when fabricating SOI photonic devices for research purposes, since results from process development on a-Si is often transferable to c-Si [70]. Several fabrication tests are however also performed on pure c-Si wafers since crystalline SOI is a relevant platform for future fabrication of high-performance devices.

3.2.2. Plasma Enhanced Chemical Vapor Deposition

Chemical vapor deposition (CVD) is a common process for depositing thin films of a wide range of materials like silicon, carbon, oxides and metals. The precursors are supplied into a reactor in gas phase from an external source and react chemically to produce solid films on the substrate surface [71, Ch. 11].

Whereas high temperature and atmospheric pressure is necessary to drive many CVD reactions, films can be deposited at lower temperatures and at higher rates by utilizing a plasma discharge of the reactant gases in a process known as plasma-enhanced chemical vapor deposition (PECVD). The energy in a glow-discharge plasma helps to create and sustain the CVD reaction by decomposing the gas molecules into a variety of reactive component species [72, Ch. 6].

A schematic of a PECVD chamber is shown in Figure 3.1. In short, PECVD is performed in a vacuum chamber between two electrodes, between which a plasma is created by a radio frequency (RF) alternating electric field[1] or a direct-current (DC) discharge. The reactants are introduced through inlets in the upper electrode known as the shower head. Excited neutrals, radicals and/or charged species are formed in the plasma, and react with the substrate surface to build up a film [72, Ch. 6]. Exhaust gases are removed from the chamber by a vacuum pumping system.

Chemical Reactions

Chemical reaction pathways associated with PECVD are generally very complex, and often not well understood [71]. A thorough consideration falls outside the scope of this thesis, and only simplified net reactions are presented. A few important process parameters that influence the reactions are the electrode configuration and separation, plasma power and frequency, gas composition, pressure and gas flow rate and substrate temperature [71].

Two different materials will be deposited in this project – amorphous silicon (a-Si) and silicon dioxide (SiO_2). Although both materials will be deposited in

---

[1] The RF plasma source commonly operates at 13.56 MHz, which is a dedicated frequency for industrial, scientific and medical applications. Low frequency RF power at some 100 kHz can also be used, resulting in denser films due to increased ion bombardment of the growing film since the ions can respond to the slower alternating field [73].

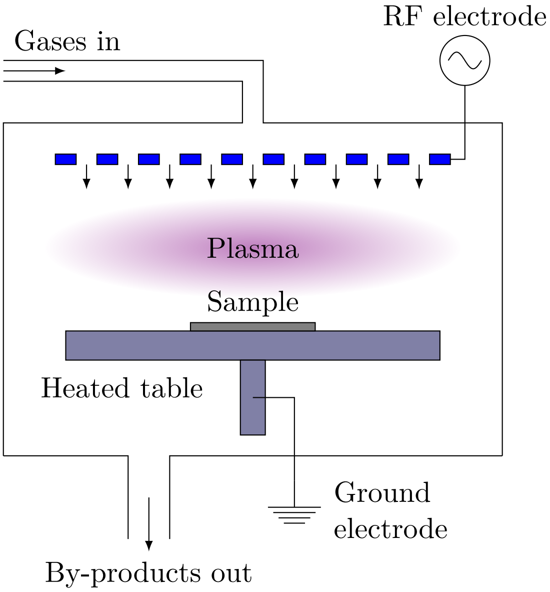

Figure 3.1.: Cross section schematic of a PECVD chamber. Figure courtesy of Ane Tefre Eide.

their amorphous forms, this will not always be explicitly stated in the following chapters of this thesis. Both the a-Si and SiO_2 films use silane gas (SiH_4) as the silicon source, and their net chemical equations are given in Reaction 3.1 and 3.2, respectively.

$$\mathrm{SiH_4(g) + Ar(g) \longrightarrow Si(s) + H_2(g) + Ar(g)} \qquad \{3.1\}$$

$$\mathrm{SiH_4(g) + 2\,N_2O(g) \longrightarrow SiO_2(s) + 2\,N_2(g) + 2\,H_2(g)} \qquad \{3.2\}$$

Further details of the recipes used can be found in Section 4.2.1.

Film Quality

Both structural film properties related to various types of uniformity and intrinsic optical properties of the a-Si material itself can greatly influence the optical performance of fabricated devices.

High optical performance requires film uniformity across the device in terms of small fluctuations in both thickness and refractive index. Surface roughness will reduce performance by introducing scattering losses, although waveguide sidewall roughness from lithography patterning or etching is considered a more severe loss mechanism [45, 49].

Furthermore, the amount of material absorption is highly dependent on the composition and atomic structuring of the silicon material. The structure of atoms in a-Si lack a long range order, which causes high densities of point defects and atoms with dangling bonds. Dangling bonds cause mid-bandgap defect states that result in substantial losses for optical waveguides if present in high concentrations such as in pure a-Si ($> 10^{19}$ cm^{-3}) [74]. It has been found that addition of hydrogen to amorphous silicon reduces the defect density by saturating the dangling bonds down to values of $\sim 10^{15}$ – 10^{16} cm^{-3} [74]. The hydrogenated amorphous silicon is from now denoted a-Si:H.

High performance a-Si:H waveguides with propagation losses for TE modes close to 2 dB/cm have been demonstrated [47], making it a competitive alternative to c-Si where state of the art photonic wires perform between 1 and 2 dB/cm [10, Ch. 13]. A key advantage of a-Si:H is its possibility of being deposited using low temperature (~250 °C to 400 °C) PECVD [74]. The incorporation of hydrogen during PECVD of a-Si depends largely on the deposition process parameters, and the reader is referred to Narayanan [74] for a detailed discussion. Most importantly, the deposition temperature should be about 200 °C to 300 °C in order to retain hydrogen in the films, which means a plasma is necessary for decomposing the SiH_4 gas and sustaining the reaction.

3.2.3. Electron Beam Lithography

Electron beam lithography (EBL) is the process of scanning a focused electron beam over an electron sensitive thin film in order to selectively change its solubility [75, Ch. 2]. After immersing the sample in a chemical called the developer, either exposed or non-exposed regions of the film are selectively removed, leaving behind a patterned surface which typically serves as a mask in subsequent processing steps. The electron sensitive thin films are referred to as “e-beam resists” or simply *resists*, and normally consist of organic polymer materials [76, Ch. 5].

Upon radiation from a beam of high-energy electrons, the resist can become more soluble due to polymer bond breaking, or less soluble if the beam induces cross-liking of organic molecules [76]. The former is the case in a *positive* resist, and the latter in a *negative* resist. The names refer to the appearance of the remaining pattern with respect to the exposed pattern after subsequent processing steps such as material deposition or -removal. Figure 3.2 shows how the patterns from an idealized e-beam exposure of negative and positive resists will appear after development.

A characteristic property of any e-beam resist is its *sensitivity* – the dose per area needed for sufficient exposure, normally given in units of µC/cm^2. Importantly,

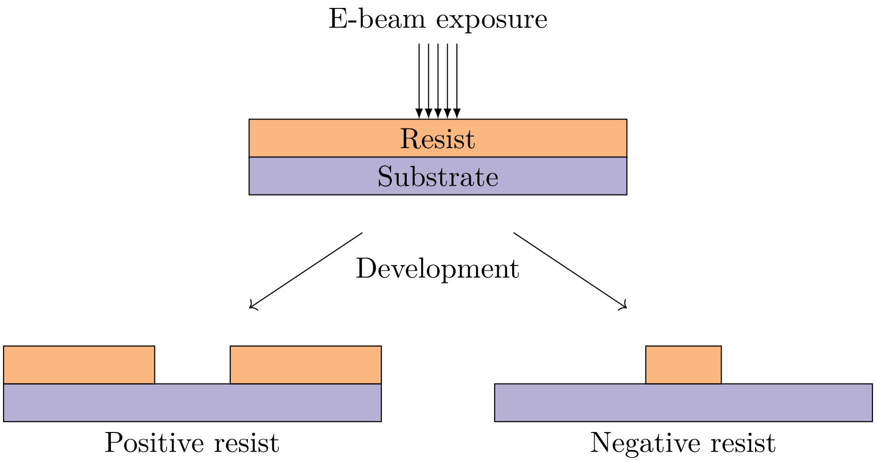

Figure 3.2.: Illustration of resulting resist patterns after development of positive and negative e-beam resists.

the sensitivity depends in a complex manner on several parameters such as the resist material, the resist thickness, the substrate material and the development process (time, temperature, agitation). Furthermore, the e-beam acceleration voltage affects the sensitivity where the required dose increases approximately proportionally with the voltage due to a lowering of the inelastic scattering cross-section for high energy electrons [75, 77].

The main power of EBL is that it is a “maskless” process which renders it flexible for research purposes where low-volume production is not a limitation. Contrary to photo-lithography, the ultimate resolution of EBL is not set by the wavelength of the interacting particles or the resolution of the (electron) optics, but by the resolution of the resist itself and subsequent fabrication processes [78]. Using EBL, patterns can be written with a superior resolution better than 10 nm [75, 79, 80]. The serial writing in the exposure process is however also the biggest disadvantage of EBL, since exposure of large areas can be extremely slow compared to parallel methods such as photo- or imprint-lithography[2].

Instrumental Setup

Typical EBL systems resemble largely scanning electron microscopes (SEM) which are discussed and illustrated in Section 3.3.1. In addition to the electron guns,

---

[2] It is noted that the main use of EBL in the semiconductor industry is precisely that of writing masks for use in photo-lithography [53, Ch. 12].

magnetic lens systems and imaging detectors found in conventional SEMs, highly accurate mechanical translation stages, pattern generators, current meters and beam blanking systems are crucial parts of an EBL.

Translation stages are needed for patterning large areas because the field over which the focused electron beam can be deflected by the magnetic lenses, the *write field*, is of limited size. Typical write field sizes range between 100 µm×100 µm and 1 mm×1 mm [53, Ch. 12]. EBL systems also often operate at higher acceleration voltages than imaging SEMs, because of the resulting straighter resist sidewalls. Although the total size of the sample-beam interaction volume (see Section 3.3.1) increases with the acceleration voltage, electrons with high energies undergo less forward scattering and thus less beam broadening *within the resist layer* [75, Ch. 2]. A common EBL beam energy is 100 keV, which is also that used in this project. The interaction between electron beams and resist/substrate is not discussed in depth here, and the reader is referred to e.g. [75, 76, 81] for further information.

Electron Beam Write Time

The biggest and most straightforward contributor to the write time in an EBL process is usually that spent on exposing the resist, as understood from the simple relation

$$t = \frac{DA}{I}, \tag{3.2}$$

where D is the sensitivity of the resist (minimum required dose), A is the area that is exposed and I is the exposure current. Typical values for sensitivities of commercial e-beam resists are some 100 µC/cm^2 [82, 83], and a typical exposure current can be e.g. 1 nA, although both values can vary by orders of magnitude. Exposing a 1 cm^2 sample using these nominal values would take 28 hours, illustrating the limitations of EBL in high throughput manufacturing.

Additional time is required for mechanically translating the stage between write fields, performing beam corrections and for blanking and un-blanking the beam when exposing non-connected regions. Depending on the design of the exposure pattern and choice of write fields, these steps can in certain cases contribute significantly to the write time.

Resolution Limiting Mechanisms

Several mechanisms act to limit the resolution in EBL patterning. As discussed in Section 3.3.1 for the scanning electron microscope, various kinds of lens aberrations are important contributors. Also, since a typical EBL pattern is divided into many write fields, so-called stitching errors can occur when aligning neighboring fields after discrete stage translations [53]. Furthermore, the overlay accuracy is

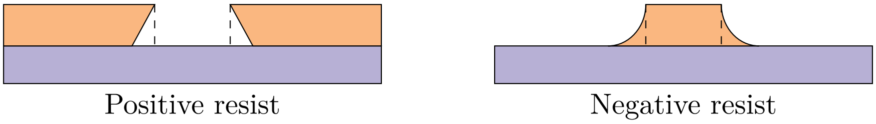

Figure 3.3.: Illustration of typical resist patterns affected by proximity effects. The dashed lines indicate the edges of the intended exposed areas.

important to consider whenever a pattern is written on top of a previously defined structure.

Proximity effects is the phenomenon where the scattering-induced e-beam widening causes resist outside the scanned areas to receive a non-zero dose. These effects manifest themselves differently for positive and negative resists, and are highly important to consider during any EBL process development. For positive resists, proximity effects result in removal of more material than intended during development[3], whereas negative resist patterns get the characteristic side-lobes illustrated in Figure 3.3 from exposure by backscattered electrons. A common way of compensating for proximity effects (in addition to using an appropriate dose) is through software [53]. Monte Carlo simulations of electron beam scattering can be used as input to algorithms that automatically compensate for the effects by adjusting exposure doses in different regions of the pattern.

Pattern Development

The development process in which the patterned resist is selectively removed from the sample is an equally important step for achieving high resolution as the exposure. A detailed consideration of the chemistry and kinetics involved falls outside the scope of this thesis, but schematics of resist patterns expected from different degrees of development are illustrated in Figure 3.4. The transition from profile (a) to (c) can be achieved by either immersing an exposed sample in the developer for longer times, or by using a more aggressive chemical. The different profiles can all be desirable for given applications, and lithography processes are designed accordingly.

The observant reader will note that the resist profiles originating from pronounced proximity effects and over-exposure in Figure 3.3 appear similar to the over- and underdeveloped profiles in Figure 3.4. Indeed, exposure and development are interrelated in a way where short exposure with long or aggressive development can be equivalent to heavier exposure with short development [75].

---

[3] The positive resist pattern in Figure 3.3 exhibits a so-called undercut which is highly desirable for certain processes such as lift-off deposition of metal patterns. Vertical sidewalls are however favored in this project where the resist serves as an etch mask.

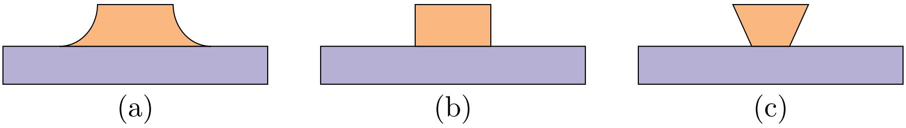

Figure 3.4.: Typical resist profiles resulting from development processes of increasing strength from (a) to (c).

3.2.4. Inductively Coupled Plasma-Reactive Ion Etching

Inductively coupled plasma-reactive ion etching (ICP-RIE) is a commonly used low-pressure dry etching technique for achieving highly anisotropic material removal in high aspect ratio openings. The ICP-RIE uses two independent RF sources, where one is used to strike plasma in a gas mixture and the other to create a DC bias which extracts and accelerates ions and radicals from the plasma towards a sample surface. This gives independent control of ion density and energy, which is desirable for tuning the etching action to yield etch profiles with desired characteristics. The following discussion on this technique and etching in general is based on Chapter 16 of Quirk [71].

The ICP-RIE process chamber resembles in many ways that in Figure 3.1 used for plasma-enhanced chemical vapor deposition, with gas in- and outlets, electrodes and temperature controlled table for supporting the sample. In addition, a spiral coil separated from the plasma by a dielectric plate or quartz tube is used to generate an RF *magnetic* field which serve to densify the plasma, hence the name “inductively coupled plasma”. By applying an RF electric field, charged species in the plasma are accelerated in opposite directions, where a strong DC bias results in the positive ions to accelerate towards and bombard the sample.

In other words, in an ICP-RIE the ion density and -energy are decoupled where the ICP power controls the density of the plasma, whereas the RF electric field power referred to as the capacitively coupled plasma (CCP) power controls the energy of incident ions.

Etching Action

Dry etching in general refers to etch processes induced by the the presence of a plasma discharge, giving rise to etch mechanisms that are both physical and chemical in nature. The physical part consists of sputtering from positive ions that are ionized in the plasma and accelerated towards the sample by strong electric fields. In addition, the plasma generates reactive species (free radicals, excited neutrals, charged species etc.) from the process gases introduced to the chamber, which can react chemically with the material of the sample. The gases

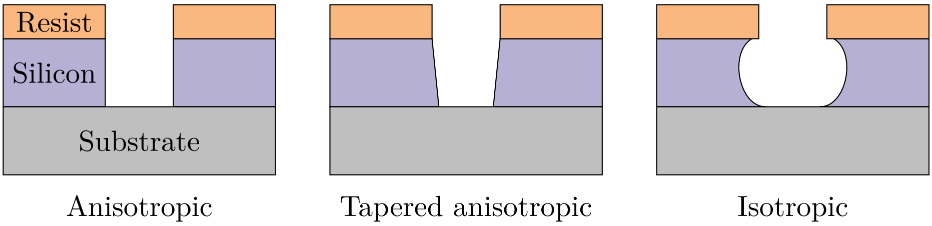

Figure 3.5.: Sketches of typical sidewall profiles from different types of etching processes.

are carefully chosen based on which chemistries that give high material etch selectivity. For example, fluorine chemistry is commonly used for etching silicon and SiO_2, and normally supplied in gases like CHF_3 and SF_6.

Physical and chemical etching mechanisms are normally used in combination, and tuned using different process parameters to yield specific desired etching profiles. For example, increased ICP power will increase the ion density (but not the energy), resulting in a more pronounced chemical etch. Increased CCP power will on the other hand increase the physical character of the etch due to the increased ion energy. Temperature, pressure and gas flows are other important parameters that influence the etch process.

Etch Profile

An etch profile refers to the sidewall shape of an etched feature [71], and it is common to divide profiles into two categories: isotropic and anisotropic. Both are illustrated in Figure 3.5, along with a tapered anisotropic profile. The appearance of an etch profile is directly related to the dominant etch mechanism. Wet chemical etching normally results in equal etch rates in all directions and thus isotropic profiles, while anisotropic profiles are commonly achieved using dry etching with a significant amount of physical sputtering. Furthermore, a high directionality of the ion bombardment is required to drive the plasma into high-aspect openings, which is achieved using high-density plasma sources such as those found in ICP-RIE systems [71]. For waveguiding purposes, vertically etched sidewalls are highly important since slanted profiles breaking the vertical symmetry lead to coupling between TE and TM modes [45].

Etch Rate and Selectivity

The etch rate describes how fast material is removed from a sample surface during etching, and will in this project be given in units of nm/min. Several process parameters influence the rate such as the material in the sample, etching chemistry and concentration, CCP power and ICP power.

Importantly, the rate can also depend on the geometric pattern density where a phenomenon called *microloading* refers to a reduced etch rate in structures having high aspect ratios. The explanation for this is the difficulty of getting etchant ions into and etch by-products out of these small openings [71, 84], causing a decreased etch rate as the features become deeper.

Etch selectivity is defined as the ratio between the etch rates of two materials etched under the same conditions. Most processes intend to etch only a single material, and the selectivity quantifies to which degree this is achieved. The selectivity sets a lower limit for the required resist layer thickness. A rule of thumb is that wet chemical etching yields high selectivities of e.g. 100:1, whereas dry etching can have poor selectivity down to 1:1 or worse. The latter would be the case where the resist mask is etched at the same rate as the film itself.

Polymer Sidewall Passivation

Organic etch masks such as photo- or e-beam resists can lead to deposition of polymer chains onto the sidewalls of etched features when they react with etching gases such as CHF_3. These sidewall polymers can be highly chemically stable due to strong carbon-fluorine bonds, meaning they form an etch-resistant sidewall-layer that prevents lateral etching [71]. The result is improved etch anisotropicity, which is desirable for structures such as waveguides and photonic crystal holes where vertical sidewalls are important. Furthermore, the sidewall passivation serves to minimize sidewall roughness which as discussed in Section 2.6 is a key contributor to optical losses in high index contrast waveguides [45].

The strong bonds in the polymers render them difficult to remove after etching. A common method for achieving this is with an O_2-plasma treatment, which is a widely used technique in the semiconductor industry for removing organic surface contaminants. Often, this process is referred to as *plasma ashing* [71].

3.3. Characterization

The characterization performed in this project consists of various types of device inspection performed during fabrication and development of fabrication processes. As for the fabrication processes described in Section 3.2, the most trivial instruments used for characterization (e.g. optical microscopes) are not discussed in this report.

3.3.1. Scanning Electron Microscopy

Scanning electron microscopy (SEM) is a widely used imaging technique for visualizing micro- and nanostructures. High energy electrons in focused beams that are raster scanned across a specimen enable topographic imaging with spatial resolution of approximately 1 nm – orders of magnitude beyond the fundamental diffraction limit of far field optical microscopy ($\sim \lambda/2$) [76, Ch. 1]. The theory behind this imaging technique is extensive, and only a selection of the most important aspects are considered here. Also, since the method forms the basis for the electron beam lithography-technique, it is important to know its working principles.

Electron Beam

Figure 3.6 (a) illustrates a typical SEM setup, where it is noted that different implementations are possible. In short, an electron gun[4] provides a source of electrons that are accelerated to energies typically ranging from 1 keV to 30 keV. The electrons pass through a number of magnetic lenses and apertures which focus the beam. The beam reaches the scanning coils which serve to deflect and raster scan the beam in the sample plane. The final lens (the objective) forms a very small electron probe that hits the sample, typically with diameters between 1 and 10 nm [76].

Interaction Volume and Signal Detection

When the electron beam penetrates the specimen surface, electrons are scattered from a range of different depths, commonly called the interaction volume. Figure 3.6 (b) illustrates some interactions that occur and at which depths they can be detected from, but it is noted that the shape and size of this volume will depend on acceleration voltage and sample material. Various kinds of signals from these interactions are detected by different detectors as the beam is raster scanned, where the two most common signals are generated from *secondary electrons* (SE)

---

[4] A few commonly used electron guns are thermionic tungsten emitters, LaB_6 cathode sources and cold/Schottky field emitters [81].

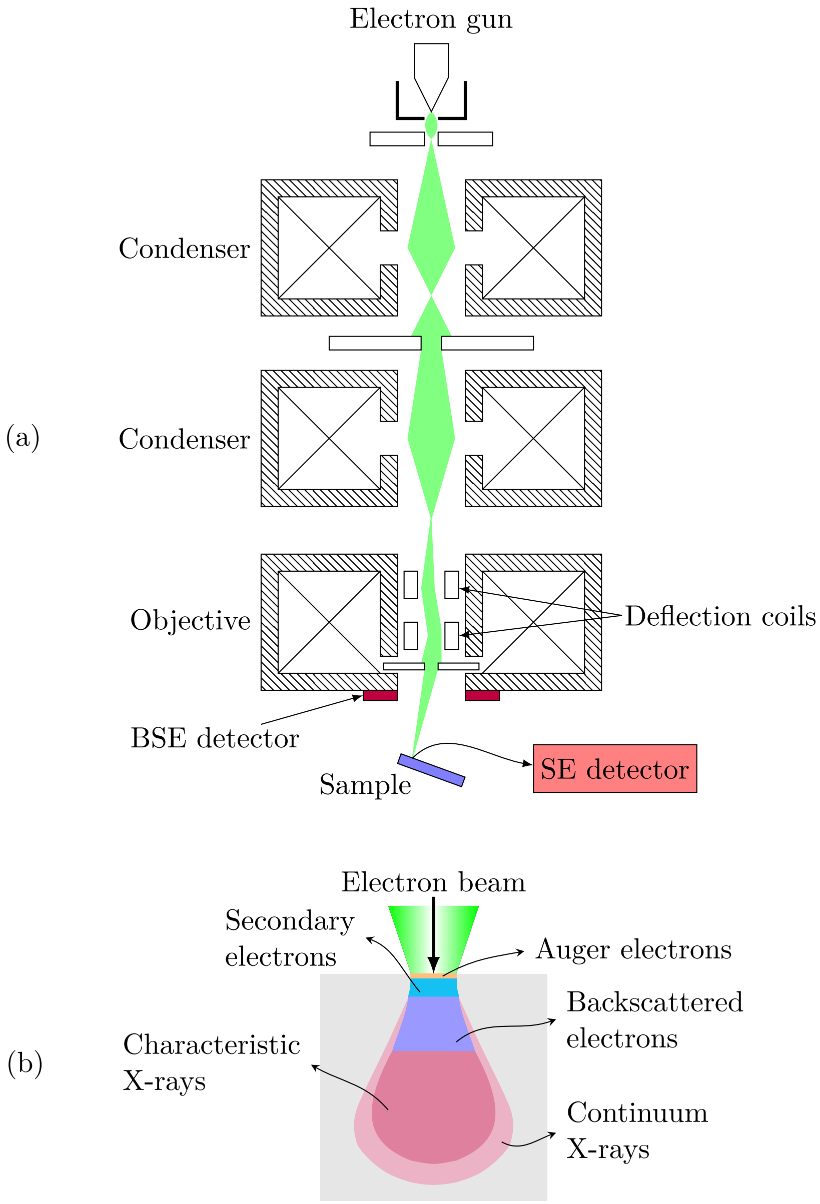

Figure 3.6.: Top: Schematic of the setup of a scanning electron microscope. Bottom: Sketch of the beam-sample interaction volume showing from which (illustrative) depths different particles can escape and be detected. Figures courtesy of Ane Tefre Eide.

and *backscattered electrons* (BSE). In addition, element-specific X-ray photons and Auger electrons can be used for chemical analysis of a substance, but these contrast modes are not covered here.

Secondary electrons are formed in inelastic collisions between the incident (primary) electrons and the atoms in the sample. Although being generated in the entire interaction volume, only those formed in a very shallow region within $\sim 2\,\mathrm{nm}$ from the surface are able to escape since they have low energy, by definition $< 50\,\mathrm{eV}$ [76]. This means that SE gives high topographic contrast, and will therefore be the most commonly used imaging mode in this project. The SE-signal is obtained by applying a positive bias to a detector to draw the SEs onto it, as can be seen in Figure 3.6 (a).

Backscattered electrons are obtained when primary electrons are elastically scattered back towards the surface. Similarly, elastic low-angle (forward) scattering results in beam widening as depicted in Figure 3.6 (b). Since these collisions are elastic, the BSE energy is much higher than SEs and they can escape from deeper regions below the surface. This reduces the resolution, but gives more information about what lies deeper into the sample. Additionally, the elastic scattering process is highly dependent on atomic number Z since the probability of high angle scattering is proportional to Z^2 [76]. This makes BSE an imaging mode with enhanced elemental contrast compared to SE. Due to the high energy of BSEs, their trajectories can be well approximated by straight lines ejecting from the sample surface. Therefore, the BSE detectors are placed close to the entrance of the electron beam.

Resolution Limiting Mechanisms

The spatial resolution of a SEM is dictated by the incident-probe diameter and can be significantly limited by lens aberrations such as chromatic aberration, astigmatism and spherical aberration. Careful alignment schemes of the lens systems are necessary to reduce the effects of these when operating a SEM, but will not be discussed further. Electron-electron interactions are stronger for low acceleration voltages, which means high beam quality is easier to achieve with high voltages. However, the size of the interaction volume increases with the electron energy due to increased mean free paths, which means that the spatial resolution is reduced. There is thus a trade-off between small interaction volumes and high beam quality, and the parameters giving the best images in a particular situation will depend on the sample and the features of interest.

For insulating samples, the electrons from the primary beam are not easily conducted to ground, which means that charging of the sample occurs. Electric fields build up and severely limit the resolution and image quality through electrostatic interactions with the incident electrons. In this case, operating at low emission currents is advantageous.

3.3.2. Reflectometry

Reflectometry is a non-destructive, fast and simple technique used to determine the thickness and optical constants (refractive index and extinction coefficient) of thin films. A reflectometer measures the spectral reflectance from a sample surface upon normally incident illumination from a wide-band source. Film parameters are then deduced from fitting the measured reflection spectra to theoretical models specific for the material combinations in question. In short, these models are determined by considering how light propagates through and reflects from interfaces between materials of different optical constants.

Reflectometry is restricted to measuring films that are optically smooth and at least partially transmitting at wavelengths within the source bandwidth. Furthermore, the films should be thick enough to allow at least one reflectance oscillation to occur over the bandwidth of the reflectance spectra. In other words, reflectometry measurements are mainly applicable to simple structures of semiconductors and dielectric thin films. For structures having either numerous and/or very thin layers, more complex methods such as spectral ellipsometry are required. If used within the bounds mentioned above, determination of film thickness with nanometer accuracy is achievable [85].

3.3.3. Atomic Force Microscopy

Atomic force microscopy (AFM) is a conceptually very simple high resolution imaging technique in the family of scanning probe microscopy methods. Based on the deflection of a cantilever caused by the force between an atomically sharp tip and a sample surface, topographic mapping with sub-atomic resolution is possible [86, Ch. 5].

Figure 3.7 shows a typical AFM instrumental setup. A laser irradiates the cantilever which reflects the beam onto a detector. The deflection of the cantilever is measured by monitoring the position of the reflected beam as the cantilever is scanned across a sample (or vice versa) using piezoelectric elements. By recording the sample height as a function of horizontal tip position, AFM measurements can yield three-dimensional topographic surface maps.

Topography maps can be used to determine the roughness of a surface, conventionally stated as the root mean square (RMS) deviation in height from the average. In this project, AFM measurements are used to find and compare the RMS roughness of various surfaces since fabrication-induced roughness results in undesirable optical scattering losses that should be minimized.

The theory of different operating modes and application areas of AFM is both rich and interesting, but not of relevance in this work. The interested reader can find further information in e.g. references [87, 86].

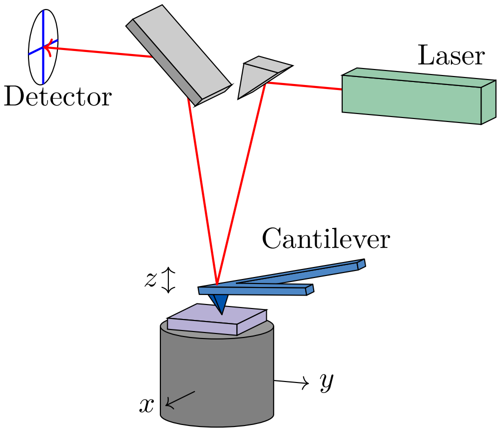

Figure 3.7.: Schematic of an atomic force microscope. Figure courtesy of Ane Tefre Eide.

Chapter 4.

Experimental Procedure

This chapter describes the experimental procedure followed in this project for computer simulations, fabrication and characterization of photonic crystal devices. The level of detail in describing the fabrication and characterization processes is intended to be sufficient for reproduction, but also with a concise amount of motivation in terms of stating the purpose of various steps and procedures. The simulations are described and motivated more rigorously, since the they are as much a design process as a straightforward “do this, then do that”-procedure.

4.1. Simulations

The photonic crystal structures considered in this project are investigated using two methods in computational electromagnetism – frequency-domain eigenproblems for computing band structures and time-domain simulations (FDTD) for computing transmission spectra of finite-sized structures and devices. In both cases, 3D simulations and 2D approximations of the same systems will be performed. Since 2D simulations are much less computational expensive, they allow for simulation of systems with higher grid resolution, larger structures and/or more complex iterative simulation schemes in optimization procedures. Nevertheless, only 3D simulations describe the systems fully and are needed for validating 2D results [19, Ch. 2].

General Simulation Parameters

Many of the photonic crystal structures investigated in this project have a number of parameters and dimensions in common. In dimensionless units, the crystal period a is used as the reference length scale by choosing $a = 1$. Furthermore, the radius of air holes and the thickness of the PhC slabs are chosen to be $r = 0.3a$ and $h = 0.55a$, where the latter only applies to the 3D simulations. These particular choices are motivated in Section 5.1.1. The refractive indices of the materials used in the simulation geometries are summarized in Table 4.1. Note that all of the

Table 4.1.: Refractive indices at 1.55 µm for all the materials used in simulations. The values are obtained from [88], except for the 2D effective index of a-Si which is discussed in Section 3.1.4.

Material	Refractive index
Air	1
a-Si	3.48
a-Si (2D)	2.87
SiO_2	1.44

2D simulations are intended to approximate 3D slabs, and for that reason use an effective index for silicon that is discussed in Section 3.1.4.

In order to maintain consistency between simulations, the same computational grid resolution is used for problems of the same type. Especially for the 3D simulations, it is desirable to use the lowest possible resolution that still gives satisfactory results. An investigation of the grid resolution requirements for accurate FDTD simulations of PhC waveguide components can be found in Lavrinenko et al. [89], where it is concluded that calculations with a resolution of 16 mesh points per period is sufficient in order to reveal the main features of transmission spectra. Only minor differences are expected to appear compared to simulations at much higher resolutions such as $a/64$. Thus, 3D FDTD-simulations are performed with a spatial resolution of $a/16$. Two-dimensional simulations require much less memory and time, which means they can be performed at higher resolutions. The 2D FDTD-simulations in this project use a resolution of either $a/24$ or $a/32$.

The specific software used for the band structure calculations allows for different resolutions in different directions. For that reason, the 3D simulations are performed with an in-plane resolution of $a/32$, and a vertical resolution of $a/16$ since the fundamental slab mode is expected to vary slowly in the vertical direction. The 2D band structures are calculated with a grid resolution of $a/64$, or $a/48$ in the case of large linear defect supercells.

4.1.1. Band Structures

All band diagrams in this project are computed using the freely available software package MIT Photonic Bands (MPB). In short, MPB computes fully-vectorial eigenmodes of Maxwell's equations with periodic boundary conditions by preconditioned conjugate-gradient minimization of the block Rayleigh quotient in a plane-wave basis [1].

The general procedure for computing electromagnetic eigenmodes with MPB is

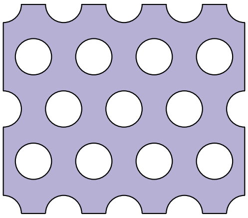

Figure 4.1.: Dielectric function showing four periods of an infinite bulk hexagonal 2D photonic crystal made of silicon with air holes of radius $0.3a$.

to define a unit cell with a particular spatial distribution of different dielectric media, and then for the desired **k**-points compute a desired number of lowest order eigenmodes.

The simulations of the most important systems that are investigated are briefly explained in the following, but further information about MPB and the physics it solves can be found in Appendix A and Section 3.1, respectively. Aspects of the simulations such as grid resolution, calculation of mode parities and various output possibilities are considered in Appendix A.

Bulk Photonic Crystals

MPB uses periodic boundary conditions to truncate the computational domain, which means that the unit cell (dielectric function) is repeated indefinitely in all directions in space. This makes the software convenient for simulating photonic crystals and other periodic media. The unit cell for a 2D air-hole silicon PhC is defined by setting silicon as the default material, before placing an air-hole of a particular radius in the center. For this to correspond to e.g. an hexagonal crystal, the basis vectors of the lattice are set to those in Section 2.2, such that the unit cell is translated by these vectors to yield a structure like the one illustrated in Figure 4.1.

Only TE modes have photonic band gaps and are thus of interest in these structures, which means only eigenmodes having this symmetry are computed. The band structures of bulk photonic crystals are computed for **k**-points along the edge of the irreducible first Brillouin Zone, i.e. along the Γ-M-K-Γ-path in reciprocal space, see Section 2.2 for further information.

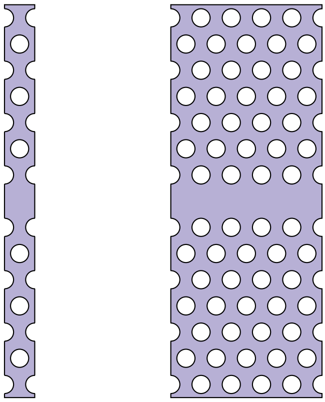

Figure 4.2.: Dielectric function used for simulating PhC line defects, here with seven cladding periods in the direction perpendicular to the defect. Left: Unit supercell. Right: The same dielectric function drawn with five periods along the defect to illustrate how the unit cell corresponds to a linear missing-hole waveguide.

Linear Defects

The periodic boundary conditions used by MPB means that periodicity-breaking features such as linear defects must be simulated using supercell approximations as explained in Section 3.1.2. A unit (super) cell for a missing-hole linear defect in the Γ-K direction is shown in Figure 4.2, which has a number of additional periods in the direction perpendicular to the waveguide. In this project, a cladding of seven periods is used, which is the same as used by Johnson et al. [60]. In other words, adjacent waveguides are separated by $14a$, and the waveguide modes are sufficiently localized so that the adjacent waveguides introduced by the supercell have a negligible effect on the mode frequencies [60].

The eigenmodes of linear defects are computed at **k**-points along the direction of the defect, which is the nearest neighbor-direction (Γ-K). Importantly, the edge of the line defect Brillouin zone does not correspond to the K-point of the bulk BZ, but instead a point referred to as K' that lies between Γ and K. This subtlety for linear defects in hexagonal crystals occurs when the reciprocal lattice of the slab is projected onto the direction along the defect [60]. Using the correct projection is of importance in terms of correctly computing the band structures, and it is accounted for in the simulations.

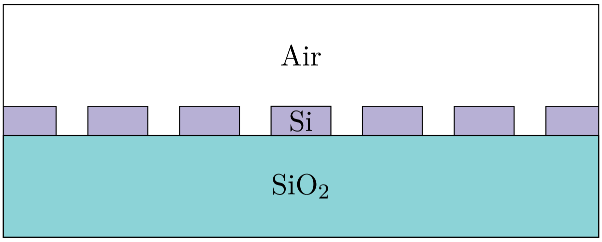

Figure 4.3.: Cross section of the dielectric function used for computing eigenmodes in silicon-on-insulator photonic crystal slabs.

Photonic Crystal Slabs

Figure 4.3 shows a vertical cross-section of a 3D PhC slab used for supercell eigenmode computations of such structures. A supercell is used to approximate the eigenmodes of individual slabs by imposing a vertical periodicity at large intervals. As for the linear defects, this artificial periodicity has a negligible effect on eigenmodes that are strongly localized – only in this case to the slab in the vertical direction. The height of the computational domain is set to $5a$, which gives cladding thicknesses of $2.225a$ on each side of the silicon slab. In the illustration, the bottom cladding material is drawn as SiO_2, although most 3D simulations in this project are performed for both SOI slabs and the corresponding vertically symmetric structures having air on both sides.

Notably, for 3D structures having a symmetry breaking oxide, the eigenmodes cannot be separated into vertically even or odd (TE- or TM-like) modes, which means that these simulations are performed without this assumption. Instead, the parity of the modes in the vertical direction is explicitly computed in the simulations.

Linear defects in photonic crystal slabs are simulated by using a supercell in both the vertical direction (z) and the direction normal to the defect (y), in other words by combining the supercells in Figure 4.2 and Figure 4.3. Although readily done, these computational domains can become large such that the simulations are demanding in terms of computer memory and time.

4.1.2. Transmission Spectra

Transmission spectra of photonic crystal structures with finite size are simulated using the finite-difference time-domain (FDTD) method with the freely available software package Meep [2].

A schematic of the general design of the computational domain used for the FDTD-simulations is shown in Figure 4.4. Simulations of structures other than

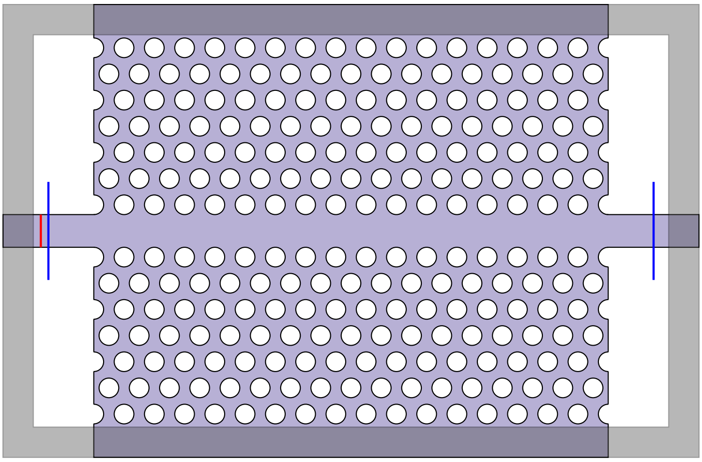

Figure 4.4.: General simulation setup used for FDTD transmission simulations. The red line corresponds to an excitation current source, and the blue lines to flux planes through which the transmission is computed. The outer shaded region is an absorbing PML.

this straight PhC waveguide are done by altering the central region of the domain. A perfectly matched layer (PML) with a thickness of one crystal period surrounds the cell in order to prevent reflections. As seen in the figure, the layer does not overlap with the holes of the crystal since PMLs fail when the material is not an analytic function in the direction perpendicular to the boundary [57]. In the case of 3D simulations, the schematic represents a slice through the center of the PhC slab. The cladding layers of air and possibly SiO_2 will look like that in Figure 4.3, only with PML-layers of thickness 1 at the edges of the cell instead of periodic boundary conditions.

A TE-wave is excited in the incoupling waveguide (left side) by a line or plane current source, depending on whether the simulation is performed in 2D or 3D. The source is a Gaussian pulse having a selectable bandwidth that is individually chosen in different simulations to investigate the transmission at specific frequencies of interest. A flux plane three times the width of the outcoupling waveguide is positioned at the output, and the accumulated Fourier transforms of the fields in this region are used to determine the frequency dependent transmission through the structure. All transmission spectra are normalized to the transmission through a reference structure, which is simply a straight waveguide extended across the entire computational domain, with a width equal to that of the incoupling waveguide, which is $\sqrt{3}a - 2r$.

The flux plane positioned before the photonic crystal structure is used in simulations where reflection spectra are computed in addition to the transmission. In order to separate the incident and reflected fields at this plane, it is necessary to save the Fourier-transformed fields from the normalization run and loading them (negated) before the final simulation. In this way, the Fourier-transformed incident fields are subtracted from the Fourier transform of the scattered fields.

There are numerous technical aspects to consider when performing FDTD-simulations with Meep, and a more in-depth discussion can be found in Appendix B. For example, concepts such as different types of current sources, exploitation of symmetries in the simulation domain, source cutoff and simulation stop conditions are discussed.

Photonic Crystal Waveguides

Transmission spectra of PhC waveguides are computed from FDTD simulations of structures like that in Figure 4.4 for both 2D PhCs, 3D air-bridge slabs and 3D slabs on oxide substrate. See Figure 2.5 for a visualization of these structures. Propagation losses in the different structures are investigated by computing the transmission through 21 equidistant flux planes positioned along a PhC with a length of $101a$.

Bends and Y-junctions

The simulation domains used for measuring transmission through 60° bends and Y-junctions differ from Figure 4.4 in that the outcoupling waveguide(s) exits at an angle to the incoupling waveguide. The flux planes are thus shifted and rotated accordingly, but further changes to the simulation setup are not made.

The main purpose of simulating the bends and beam splitters is to optimize their transmission as much as possible at relevant operating frequencies of the Mach-Zehnder interferometer. This is done through structural tuning of the local area around the component of interest. Poor power transmission is often related to a multi-mode nature of the junction, and the optical volume should be reduced to ensure that only a single mode is guided. This is supported by the investigation by Chutinan et al. [35] where the band structure in the Γ-X direction is found to be multi-modal, which causes large mode mismatch to the single modes that are guided in the linear defects.

Several possible methods for reducing the optical volume exists, where two main approaches are based on either designing a resonant structure tuned to high transmission at the desired frequency, or using steering approaches to smoothly split the light and guide it into both arms [19, Ch. 3]. The cavity approach has the disadvantage of yielding limited bandwidths, and also high local field amplitudes which enhance out-of-plane scattering. Thus, the approach of steering the light is

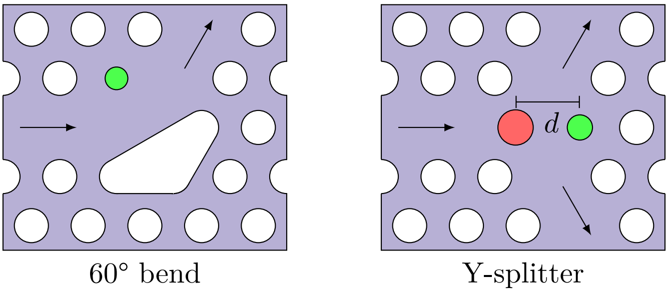

Figure 4.5.: Suggested designs for improving transmission characteristics of PhC bands and 3 dB Y-splitters.

chosen in this project. Although unconstrained optimization as demonstrated by Frandsen et al. [34] or Lu et al. [90] is assumed to yield the highest performance of a given component, a simple brute force optimization procedure is chosen in this project. A predetermined set of parameters are tested in all chosen combinations and sorted after which yield the best performance.

For the Y-splitters, three degrees of freedom is chosen, loosely based on the procedure of Wilson et al. [91]. An additional hole is introduced to the junction, and both its position in the x-direction and radius are allowed to vary. The final degree of freedom is the radius of the junction corner hole. For the bends, an approach inspired by Bogaerts [19, Ch. 3] is used where the intention is to gently steer the light around the bend in a total internal reflection-like manner. A slot is etched between two holes, which forms a corner reflector. One degree of freedom is used in the radius of the corner hole on the opposite side of the bend. The characteristics of the suggested designs of bends and splitters are illustrated in Figure 4.5.

Structural tuning requires iterative simulations, which is highly resource intensive and time consuming if performed on 3D structures. Thus, structural optimizations are performed using 2D simulations, which is commonly done for this type of performance optimization [19, 34]. After optimizing in 2D, simulations of corresponding 3D systems are done to investigate the transferability of the results.

Mach-Zehnder Interferometers

By combining waveguide segments, 60° bends and Y-junctions, photonic crystal Mach-Zehnder interferometers can be created. An example structure can be seen

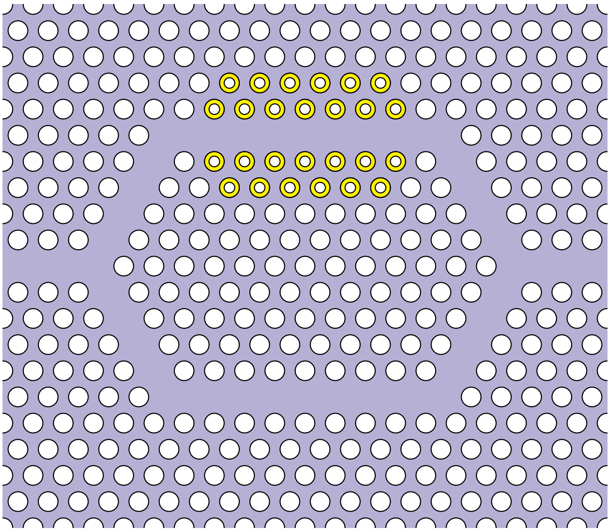

Figure 4.6.: Schematic of a Mach-Zehnder interferometer where a biolayer is added on the hole walls in the sensing arm. The thickness is exaggerated for illustrative purposes.

in Figure 2.9, which will serve as the simulation domain used for investigating MZIs. It is noted that features such as the length of the two arms and their separation are chosen merely as a first guess of what can be appropriate, and that different choices may result in better performance. Initial simulations are performed to investigate the transmission properties of MZIs where the two arms are identical (balanced). Then, the effect of adding the structurally optimized bends and Y-splitters is investigated, still with balanced arms.

Addition of Biolayers

A simple model for biomaterials is used in this project, analogous to that used by Lee et al. [14]. Figure 4.6 illustrates the method which consists of adding non-absorbing layers with a refractive index of 1.45 of specific thicknesses on the inside of photonic crystal holes in the sensing arm. The holes in the two nearest cladding rows are coated, although later investigations found that negligible changes in sensor response were obtained when coating only one cladding row with biolayers.

4.2. Fabrication and Characterization

The fabrication procedure used in this project for making silicon-on-insulator photonic crystal structures is summarized in Figure 4.7. The figure serves as an overview of the fabrication procedure in general, as well as a list of the instruments used. Instruments used for characterization are not shown in Figure 4.7, but are discussed later in this section. To aid the readability, the various steps in fabrication and characterization are presented predominantly in the order they are performed.

The overall fabrication procedure is partially the same as those followed in previous projects at NTNU [4, 5, 6, 7, 8], and is also commonly used in the field of silicon nanophotonics [53, Ch. 12]. In short, the fabrication consists of making SOI wafers in-house by depositing SiO_2 and a-Si onto silicon wafers using plasma enhanced chemical vapor deposition (PECVD), writing PhC patterns in an electron-beam resist using electron beam lithography (EBL), developing the resist and finally etching through the patterned silicon slab using inductively coupled plasma-reactive ion etch (ICP-RIE) with fluorine chemistry. In addition, polymer waveguides for use in mode-size converters for increasing fiber-chip coupling efficiency are fabricated using EBL.

4.2.1. Thin Film Deposition

The PECVD system used in this project is an Oxford Instruments Plasmalab System 100, installed at the NTNU NanoLab. The workflow and recipes used for depositing $\sim$1 µm SiO_2 followed by $\sim$220 nm a-Si onto silicon wafers is summarized in the following.

Cleaning: Wafer pieces are immersed in an ultrasonic bath with acetone for 2 min and then for 2 min in ethanol, in order to remove dust from scribing and cleaving. The pieces are then rinsed with isopropanol (IPA) and finally dried with N_2 gas.

Chamber preconditioning: If the previous user of the chamber used a different PECVD chemistry, a short deposition (1 min to 5 min) onto a dummy wafer with the intended recipe is done to stabilize the growth rate and -conditions.

Deposition: The SiO_2 and a-Si films are deposited using recipes with the parameters listed in Table 4.2. Different deposition times are tested, but they are approximately 14 min for SiO_2 and 150 s for a-Si. The samples are placed on 4 inch silicon carrier wafers during deposition.

Thickness measurements: After both depositions, reflectometry is used to measure the film thicknesses.

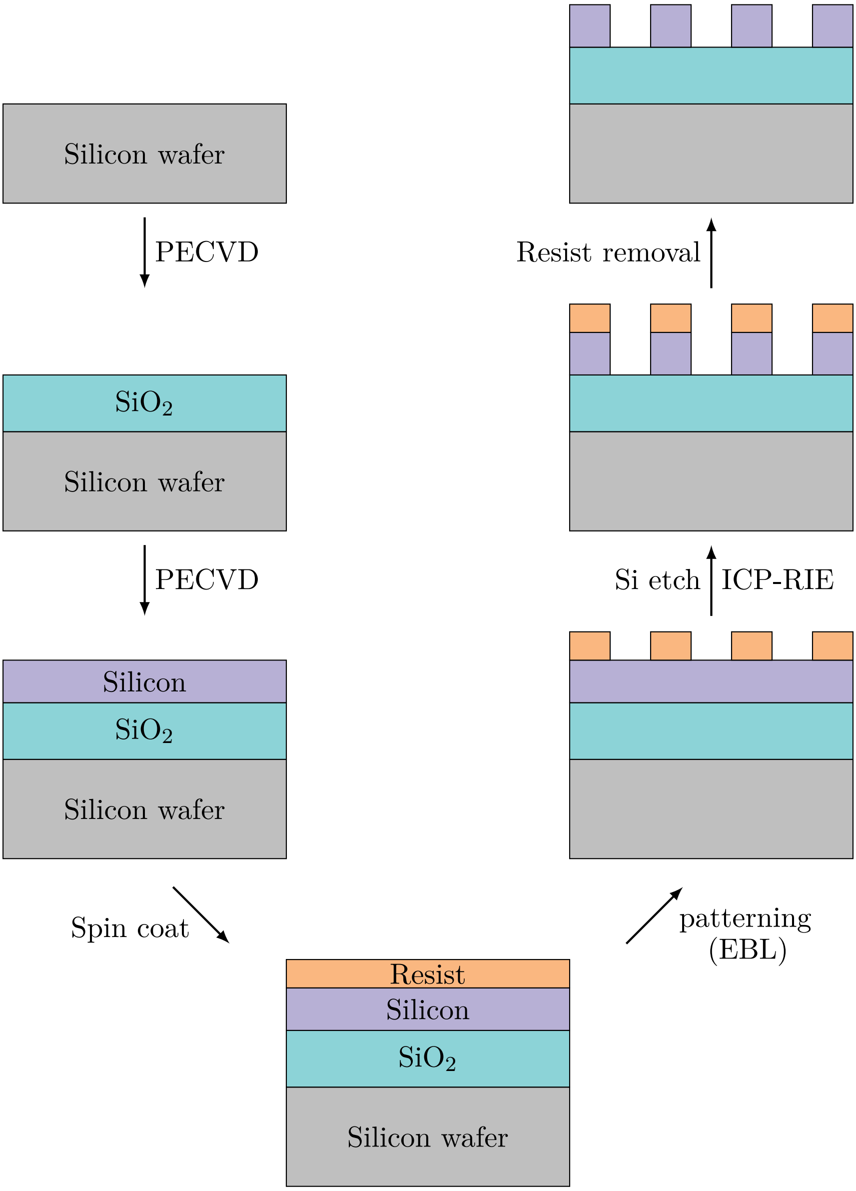

Figure 4.7.: Schematic cross-sections showing the main processing steps used in the fabrication of silicon-on-insulator photonic crystals. The relative thicknesses are not to scale.

Table 4.2.: PECVD parameters for growing SiO_2 and a-Si

Parameter	SiO_2	a-Si
SiH_4	8.5 sccm	50 sccm
N_2O	710 sccm	-
N_2	161.5 sccm	-
Ar	-	150 sccm
Pressure	1000 mTorr	500 mTorr
RF power	20 W	-
LF power	-	200 W
Temperature	300 °C	300 °C
Growth time	~14 min	~150 s

Film Thickness Measurements

Thin films of SiO_2 and a-Si with approximate thicknesses of 1 µm and 220 nm are measured using reflectometry. This material combination and thicknesses fall within the restrictions of reflectometry in general (see Section 3.3.2), and the capabilities of the specific instrument used – a Filmetrics F20 Tabletop Film Thickness Measurement System [85].

Before each measurement, the instrument is calibrated by measuring the reflectance of a reference silicon wafer, the unknown sample, and the background. Measurements are made at a number of positions across the samples to investigate thickness uniformity. The SiO_2-films are measured both before and after deposition of the succeeding a-Si.

In addition to reflectometry, cross-section SEM showing the stack of thin films is used to measure film thicknesses. This is used to evaluate the accuracy of the reflectometer, which is especially relevant when both SiO_2 and a-Si films are present since more complicated film stacks can be challenging to measure due to the high number of degrees of freedom when fitting the reflectance spectra to model spectra.

Film Roughness Measurements

The Veeco diMultimode V atomic force microscope installed at the NTNU NanoLab is used to map the topography of different samples. Most importantly, the roughness of SiO_2-films grown in-house using PECVD is compared to commercial wafers with a thermally grown oxide layer.

The AFM measurements were performed by Ane Tefre Eide, and consisted of cleaving the samples to sizes of $1\times1\,\mathrm{cm}^2$, mounting them in the sample holder and aligning the optics used to measure cantilever deflection. Scans are performed over ranges of different sizes (between $500\times500\,\mathrm{nm}^2$ and $10\times10\,\mu\mathrm{m}^2$) to get both overviews and detailed views of the surface topographies. The recorded topography data is post-processed with the NanoScope Analysis scanning probe microscopy software.

4.2.2. Sample Patterning

The SOI-samples are patterned for etching using electron beam lithography with an Elionix ELS-G100 100 kV EBL system installed at the NTNU NanoLab. The workflow used in this project is a fairly standard EBL processing scheme, and the steps are described below. A number of chemicals are used, and these are for reference listed in Table 4.3. The process outlined is the result of an optimization procedure in Section 5.2.3 where different exposure currents and doses were tested.

Cleaning: Wafer pieces are cleaned using (in this order) acetone, ethanol and IPA, before drying with N_2 gas. For pieces coming directly from scribing, sonication baths of 2 min in both acetone and ethanol are performed.

Spin coating: E-beam resist (CSAR 62 [82]) is spin coated onto the samples at 3000 RPM for 60 s (including acceleration time) with an acceleration of 500 RPM/s. This gives films of thickness ~490 nm.

Soft Bake: The sample is baked on a 150 °C hotplate for 60 s to evaporate the solvents in the resist.

Exposure: The acceleration voltage is set to 100 kV, and an area exposure dose of $350\,\mu\mathrm{C/cm}^2$ is used as found appropriate in Section 5.2.3. Write fields of $500\times500\,\mu\mathrm{m}^2$ size are used, and a beam current of 100 pA. A higher current of 5 nA is occasionally used to expose bulk regions without critical features.

Development: The sample is immersed and lightly agitated in the developer for 60 s. The sample is transferred to a beaker containing development stopper for 30 s, and finally to a beaker with deionized water for 30 s.

Inspection: Using an optical microscope with magnification up to 100x, the quality of the developed sample is assessed. If not satisfactory, the resist is removed and the process is redone from the beginning.

4.2.3. Etching

The 220 nm layer of a-Si is etched down in a Oxford Instruments Plasmalab System 100 ICP-RIE 180 installed at the NTNU NanoLab. Due to instrument down-time in the second half of the project, etching of later structures was performed in a similar instrument of the same model name, but which uses a liquid nitrogen cryogenic cooling system instead of water cooling.

The etching is done using a recipe developed by L. Vigen [6], and the important steps in the etching procedure are described below.

Chamber preconditioning: This is done by etching a dummy Si wafer for 3 min if the previous user of the instrument used a different etching chemistry.

Etching: The sample is etched with the recipe in Table 4.4. Different etch times are tested, but they are approximately 30 s for etching 220 nm. The sample is placed on a 4 inch silicon carrier wafer during the process.

4.2.4. Polymer Waveguides for Inverted Taper Coupling

As discussed in Section 2.7, inverted tapered waveguides are fabricated to increase the coupling efficiency between lensed fibers and silicon waveguide devices. The polymer waveguide is made directly in the NANO™ SU-8 epoxy-based negative tone photoresist [92]. Although conventionally being used as a photoresist, it can also be exposed and cross-linked using electron beam lithography [93, 94], which is done in this project.

The overall EBL processing scheme is similar to that described in Section 4.2.2, only with different parameter values appropriate for SU-8 as well as some additional baking steps. A specific blend called SU-8 2 is used since it together with the spin coating process described below yields films with the desired thickness of 2 µm. The processes below are developed using a combination of the information found in the resist datasheet [92], SU-8 processes developed by Jonas Ribe at the NTNU NanoLab [95] and work done by the author as described in Section 5.2.5. The chemicals used for this lithography process are listed in Table 4.3.

Cleaning: If the sample has a CSAR 62 resist film from silicon etching, it is stripped by sonication for 5 min in the resist remover in Table 4.3. It is then rinsed with IPA, acetone and IPA again before it is dried with N_2 gas.

Dehydration bake: The sample is baked on a 150 °C hotplate for 5 min.

Plasma ashing: Directly before spin coating, an O_2 plasma treatment is performed for 30 s.

Spin coating: SU-8 2 is spin coated onto the samples at 2000 RPM for 30 s with an acceleration of 500 RPM/s (adding 4 s to the spin time). The resulting films have a thickness of ∼2 µm.

Table 4.3.: List of chemicals used for the two electron beam lithography processes for patterning silicon and for making polymer waveguides. The chemicals are produced by Allresist GmbH, MicroChem and micro resist technology GmbH.

Chemical	Silicon patterning	Polymer waveguides
E-beam resist	AR-P 6200.13 [82]	SU-8 [92]
Developer	AR 600-546	mrDev 600
Development stopper	Isopropanol	Isopropanol
Resist remover	AR 600-71	PG remover

Table 4.4.: ICP-RIE parameters for etching a-Si.

Parameter	Value
SF_6	7.5 sccm
CHF_3	50 sccm
Pressure	15 mTorr
CCP power	40 W
ICP power	600 W
Temperature	20 °C
Etch time	~30 s

Soft Bake: A two step baking process is used to evaporate solvents in a controlled way which gives better coating fidelity, substrate adhesion and reduced edge beads [92]. The first step is a 60 s bake at a 65 °C hotplate, and the second is at 95 °C for 120 s.

Pattern alignment: Two registration marks are included in the exposure mask used for the silicon etch, which serve as references for aligning the polymer waveguide pattern. The marks are separated from the waveguides by 3 mm to 5 mm since the resist in these regions is manually removed using a swab soaked with acetone, see Section 5.2.5 for further information.

Exposure: An acceleration voltage of 100 kV, a beam current of 100 pA and write fields of $1{\times}1\,\mathrm{mm}^2$ size are used. The area exposure dose is set to $10\,\mu\mathrm{C/cm}^2$ as found appropriate in Section 5.2.5

Post exposure bake: This baking step is needed to selectively cross-link the exposed regions of the resist, and consists of several steps in order to minimize stress and resist cracking. The sample is put on a 65 °C hotplate for 60 s. Then, the temperature is ramped to 95 °C which takes ca. 90 s, and it is left at 95 °C for 60 s. Rapid cooling after the post exposure bake is avoided by turning off the hotplate and waiting for it to reach 30 °C to 40 °C (ca. 20 min).

Development: The sample is immersed in the developer for 45 s and lightly agitated. The sample is rinsed in fresh developer and then in isopropanol.

4.2.5. Sample Cleaving and Resist Removal

This step consists of cutting samples into smaller pieces for characterization. This is necessary both for inspecting the structure using SEM at intermediate steps in fabrication, and for future optical characterization in the laser lab. If polymer waveguides are not included for a given device, the scribing and cleaving is performed *prior* to removing the e-beam resist after silicon etching, in order to reduce the amount of scribing dust sticking to the sample.

Scribing and Cleaving

A Dynatex DX-III combined scriber and breaker installed at the NTNU NanoLab is used to scribe and cleave samples into smaller pieces along the {100}-planes of the silicon wafers. When cleaving samples to reveal cross-sections for succeeding light coupling or SEM cross-section analysis, the instrument is operated in an “edge-scribe mode”. In this mode, the samples are scribed only a small set distance inwards from opposing edges before cleaving. Features in the center such as waveguides are thus not struck by the diamond scriber tip, yielding high quality cleaved facets in the critical regions. The instrument is operated with continuous scribing when there are no structures on the surface that must be protected.

Resist Removal

The e-beam resist and dust from scribing is removed from the cleaved samples by sonication for 5 min in the resist remover for the silicon patterning process listed in Table 4.3. The samples are finally rinsed with ethanol and IPA and dried with N_2 gas.

In cases where scribing is performed after fabrication of polymer waveguides, there is no resist that needs to be removed. However, dust from scribing is removed with an ultrasonic bath in ethanol for 2 min.

4.2.6. SEM-analysis

The Hitachi S-5500 S(T)EM installed at the NTNU NanoLab is used to inspect fabricated photonic crystal devices. The "(T)" refers to the instrument's capability of imaging in transmission mode, which is not used in this project. Samples are predominantly examined after etching and resist removal, but occasionally also at intermediate steps during fabrication. The samples are mounted in either conventional or cross-section sample holders to allow for imaging of both structured surfaces and cleaved cross-sections of waveguides or etched holes.

The instrument is operated in the secondary-electron (SE) imaging mode for highest possible topographic contrast, as discussed in Section 3.3.1. Different acceleration voltages from 5 kV to 30 kV and beam currents from 5 µA to 20 µA are used depending on which yield the best image quality for a particular sample. Low currents and electron energies are generally used when imaging polymer resists since these were found to evaporate during imaging at high currents.

Chapter 5.

Results and Discussion

This chapter presents the findings from computer simulations, fabrication and characterization of photonic crystal devices. Since a large number of different simulations and fabrication processes are considered, it is decided to discuss the results directly as they are presented, instead of doing this in a separate chapter which would require excessive cross-referencing. Summarizing discussions are included at the end of each main section.

5.1. Simulations

The simulation results presented consider both full 3D structures and their 2D effective index approximations. Given that results from 2D simulations are to some degree transferable to 3D systems, they are an attractive method for structural optimization procedures due to their much lower time- and memory requirements. Most of the structures optimized in 2D are then simulated in 3D to observe the properties of real structures by including losses into radiation modes inside the light cone. Three-dimensional PhC structures both with and without a bottom oxide substrate (see Figure 2.5) are investigated since it is highly important to understand the consequences of introducing this symmetry-breaking cladding.

After discussing general goals and guidelines for designing PhC devices, a natural starting point is to consider band structures, both for bulk photonic crystals and linear defects. The band structures reveal band gaps and guided eigenmodes, and thus point out the frequencies of greatest interest for the following FDTD-simulations of finite sized PhC structures. Simple straight waveguides are initially investigated in terms of comparing 2D FDTD-results to 3D, and the additional losses induced in 3D by a symmetry-breaking oxide substrate. Being present in almost all PhC-based optical circuits, waveguides are important components that can be used as general performance probes. Succeeding simulations consider 60° waveguide bends and Y-junctions, which are discrete components of the Mach-Zehnder interferometer. Attempts are made of improving the transmission properties of these components through structural optimizations. The final simulations are of complete MZI-structures, where the effect of adding biolayers to the interferometer sensing arm is investigated.

5.1.1. Design Guidelines and Choice of Structural Parameters

The particular choices of the photonic crystal structural parameters used in this work are better motivated if the goals and challenges with the PhC band structure characteristics are explained in advance. A list of requirements for the band structure is given below, and will serve as a guideline for the simulation procedures done in the following sections. Some of the points are inspired by discussions in Bogaerts [19, Ch. 3], others by work done prior to this project [3]. Note that these requirements are developed with this project's particular photonic crystal device in mind, and they do not necessarily apply for all PhC applications.

1. A large bandgap will better confine guided modes and should thus be maximized [96]. This points in the direction of a hexagonal PhC with air holes.
2. There should only be a single defect mode at the frequencies of interest, which suggest the use of W1 waveguides (remove one row of holes) as a starting point.
3. The linear defect mode should lie close to mid-gap for maximum confinement [96].
4. The linear defect mode should operate below the light line of both the air- and oxide cladding to reduce out-of-plane losses [19].
5. The defect mode should have a large group velocity because a small one results in a narrow transmission window and susceptibility to structural disorder [97][1].
6. The defect mode should have little chromatic dispersion within the frequency range of operation to achieve a fixed oscillation period in the transmitted intensity of the interferometer [41].
7. The integrity of the crystal lattice should be maintained to enable integration and alignment of several discrete components such as waveguide, bends and splitters [19].

---

[1] Small group velocities do however increase the light-matter interaction time [19] which can be useful for the refractive index based sensing [98].

Several of the requirements in this list happen to contradict, and the choice of structural parameters must be made as a compromise. For instance, a large band gap is achieved using large holes of $r \sim 0.4a$ or bigger [96], but this has been found to give W1 linear defect guided modes of undesirable dispersion characteristics in terms of nearly flat bands that lie close to the lower edge of the band gap, as well as the presence of defect modes above the light line for all frequencies [96, 3]. Smaller holes have been found to give reduced band gaps, but also linear defects that support modes with a frequency range of single mode operation, have less chromatic dispersion and cover wider frequency bands below the light line. Furthermore, smaller holes result in less edges from which fabrication induced roughness can cause scattering losses.

Hole radii in the range of $0.275a$ to $0.35a$ are commonly used in reported designs of SOI PhC slab devices, and have been demonstrated both experimentally and through simulations to yield good waveguiding dispersion and transmission characteristics [68, 19, 96, 97, 99, 52, 55, 100]. For that reason $r = 0.3a$ is chosen for the devices in this work, although other hole sizes can at later stages be relevant to try depending on specific design requirements. Furthermore, the thickness of the silicon slab is chosen to be $h = 0.55a$ which ensures support of only a single vertical mode. This value is also close to $0.6a$ which is shown in Johnson et al. [26] to maximize the band gap for hexagonal lattice hole slab PhCs.

It is possible to etch PhC holes either through only the silicon membrane, or also into the underlying SiO_2 cladding in so-called *deep etching*. A deep etch has the advantage in SOI PhC devices of reducing the vertical asymmetry, thus reducing the losses caused by interaction between TE-like and TM-like modes. However, in practice, deep etching introduces significantly greater sidewall roughness, which is a principal source of losses [19], and shallow etching is often the etch method of choice.

Although W1 waveguides do satisfy many of the requirements listed above, the lowest-lying defect mode, from now referred to as the *ground mode*, lies well below mid-gap in the frequency range where it lies below the light line [96, 97]. Also, this part of the dispersion curve is very flat, making these waveguides narrow-band. A number of methods for structural tuning of linear defects have therefore been suggested for pushing the ground mode to higher frequencies near mid-gap. In general, such methods have been based on pushing modes to higher frequencies by reducing the amount of high dielectric material which forms the waveguide, and examples can be seen in Figure 5.1.

Although techniques for structural tuning of W1 defects have been demonstrated to yield ground modes at mid-gap frequencies, they all come with significant drawbacks [19, Ch. 3]. The method from Notomi et al. [97] in Figure 5.1 (a) violates point 7 in the list by shifting regions of the lattice, making integration of waveguides with other components such as bends difficult. The latter two methods in Figure 5.1 (b) and (c) show promising theoretical results in Lončar

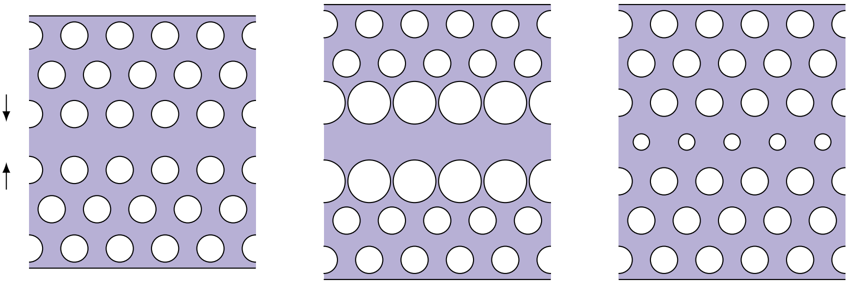

(a) (b) (c)

Figure 5.1.: Methods suggested in references [96, 97] for tuning of linear defect mode dispersion by reducing the amount of high dielectric material: Narrowing of the line defect (a), increasing the radius of holes adjacent to the line defect (b) and varying the radius of holes inside the line defect (c).

et al. [96], but in practice reduce the optical volume by introducing additional sidewall surface, which makes them sensitive to fabrication quality and scattering losses. For these reasons, simple W1 linear defects are used as waveguides in this work. Such waveguides have also been extensively investigated in the field of research both through simulations and experiments, which make them an attractive choice in terms of comparing findings to the work of others.

To summarize, the PhC devices considered in this project are designed with a hexagonal lattice of air holes with radius $r = 0.3a$ in silicon slabs of thickness $h = 0.55a$, and simple W1 linear defects (single missing row of holes) are used for waveguiding. The holes are chosen to only perforate the silicon core, due to the resulting practical advantages in succeeding fabrication. Most of these characteristics are illustrated in the upper part of Figure 2.5.

5.1.2. Band Structures

The band structure of bulk photonic crystals and the dispersion of guided modes in line defects are important to investigate for PhC devices of any kind. It is natural to perform such simulations at an early stage in order to provide an understanding of the fundamental features of light propagation and confinement in the PhC structures that will constitute the interferometric sensor device considered in this project.

Bulk Photonic Crystals

Figure 5.2 shows the computed band structures of hexagonal lattice air-hole photonic crystals with $r = 0.3a$ and slab thickness[2] $h = 0.55a$. The upper figure shows the band structure of a true 2D structure, where an effective index of silicon is used to better approximate the properties of slabs having a finite extension in the vertical direction. The lower two plots show the band structures of PhC slabs, where (b) corresponds to a vertically symmetric air-bridge structure, and (c) is the equivalent structure with a bottom SiO_2 cladding, see Figure 2.5.

A number of observations are made from Figure 5.2 which agree with the discussions made in Section 2.3. Firstly, both of the slab structures have shaded regions corresponding to a continuum of radiation modes inside the light cone. Notably, the light line of SiO_2 lies at lower frequencies than that of air by a factor $n_{\mathrm{SiO}_2} = 1.44$. Since radiation modes exist at all frequencies, any band gaps found in slab structures will be incomplete, and will only be frequency ranges where no *guided* modes exist. A true band gap as that for the 2D structure in Figure 5.2 (a) is thus not achievable. Since $\mathbf{k}$ is not a conserved quantity whenever the in-plane translational lattice symmetry is broken, optical power can be lost from guided modes through excitation of leaky modes inside the light cone with the same ω. As discussed in Section 2.4, this is an inherent loss mechanism which follows from introducing e.g. bends and splitters.

Furthermore, the band structures in Figure 5.2 (a) and (b) both exhibit band gaps for TE(-like) polarization, indicated as a shaded region of blue color. This is as expected for an air-hole hexagonal PhC, where the thin veins running between holes force higher order TE-modes to much higher frequencies than those of the lowest band, forming a band gap.

Lastly, whereas guided modes can be classified as vertically purely even/odd (TE-like/TM-like) for the air-bridge slab, this is not the case in the band diagram of the vertically asymmetric SOI slab in Figure 5.2 (c). The guided modes can nevertheless be classified after their z-parity, which was computed during the simulation. As discussed in Section 2.3, a true even or odd eigenstate will have a parity of 1 or -1, while other states will have something in between. A color coding scheme is used in Figure 5.2 (c) to show which bands are nearly even/odd or of significantly mixed character. The colormap is for comparison purposes designed to resemble the colors used for TE/TM modes in Figure 5.2 (a) and (b).

It is seen that the z-parities of the bands in Figure 5.2 (c) are similar to the true even/odd parities in Figure 5.2 (b), which is explained by the oxide cladding only weakly perturbing the eigenmodes relative to the air-bridge slab modes. Heuristically, this is due to the small difference in refractive index between air and SiO_2 compared to the much higher index of silicon. Although the vertical

---

[2] The slab thickness obviously only applies for the 3D simulations, but is accounted for in the 2D simulations through the choice of silicon effective refractive index.

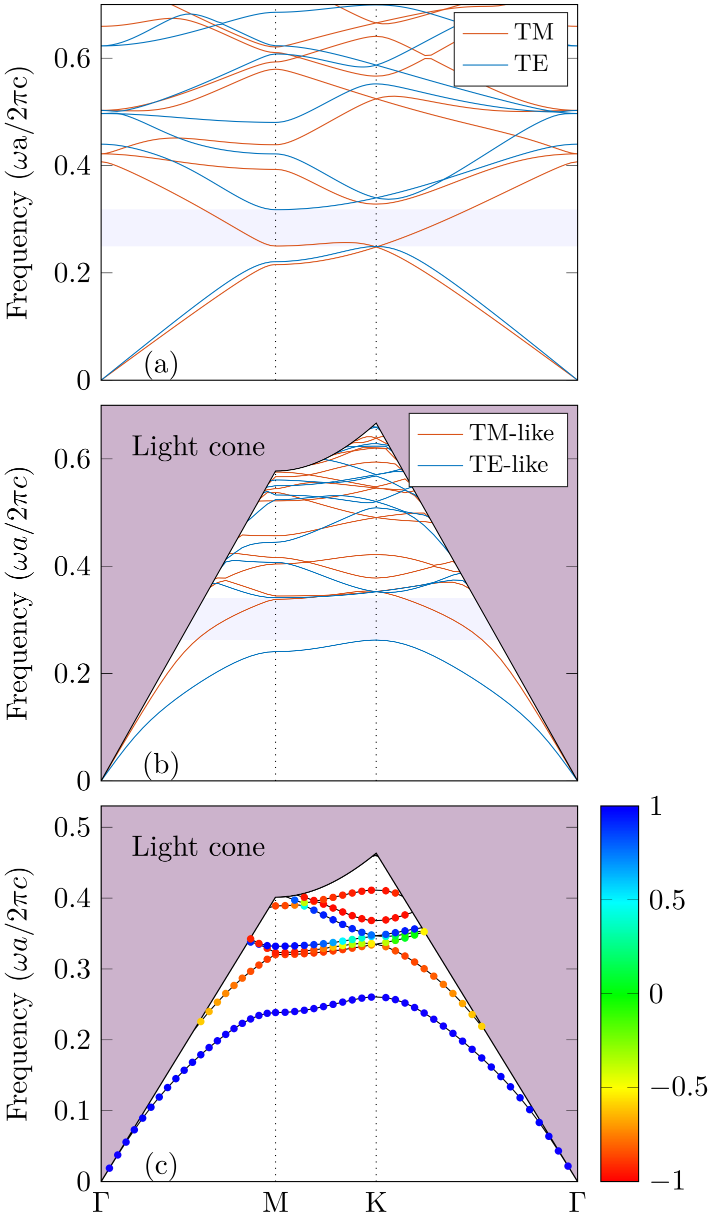

Figure 5.2.: Bulk band structures of air-hole hexagonal photonic crystals for (a) 2D PhC, (b) air-bridge slab PhC and (c) SOI slab PhC. The colorbar in (c) refers to the computed z-parity of a given eigenstate.

asymmetry indeed destroys the band gap that exists for TE-like modes in air-bridge slabs, some effects of the band gap will persist if the TE-like and TM-like modes are only weakly interacting [26]. The perturbation caused by the symmetry breaking substrate for waves that are strongly localized to the core can be small, and this is is normally the case in high-index contrast material systems such as SOI [30].

In addition to qualitative band structure considerations, the frequency positions for the bands in Figure 5.2 can be considered. Although not clearly observable from visual inspection, the bands of the SOI slab are confirmed to be shifted to slightly lower frequencies than those for the air-bridge slab. This is as expected because the SiO_2 cladding reduces the effective mode indices even though they are mostly confined to the silicon core.

The 2D band structure also resembles those for 3D slabs in terms of the size and position of eigenmodes and band gaps. The gap center positions in Figure 5.2 (a) and (b) are measured to be at the dimensionless frequencies 0.2834 and 0.3019, respectively, and the gap sizes are 24 % and 26 %. It is pointed out that the effective index of silicon chosen in the 2D simulations was determined for an SOI-slab, and not a suspended membrane. Still, the band structures appear both qualitatively and quantitatively similar, which illustrates the usefulness of approximate 2D simulations in situations where computational power is a limiting factor. For comparison, the gap center and -size for a 2D band structure computation where no effective index corrections were made were found to be 0.2397 and 28 %, respectively, demonstrating the importance of using an effective refractive index when approximating 3D slabs with 2D simulations.

Linear Defects

Figure 5.3 shows the band diagram of a W1 linear defect in an air-bridge photonic crystal as depicted in the bottom half of Figure 2.5. Only TE-like modes are shown, since the vertical symmetry of the air-bridge means that they cannot interact with TM-like modes. As explained in Section 2.4, the band structure is projected onto the spatial direction of the linear defect (Γ-K), which gives rise to continua of bulk states depicted as gray shaded regions in the diagram. These regions support TE-like states that are extended in the plane of periodicity, which means that any confinement-based waveguiding must use modes that lie outside these. As for the bulk crystal band diagrams in Figure 5.2, there is also a continuum of states above the light line which can leak out into the air claddings.

It is seen that there are discrete defect modes both below the projected bulk states and in the gap between two separate bulk mode continua. The former corresponds to so-called index-guided modes, and the latter to gap-guided modes, see Section 2.4. Only gap guided modes are suitable for waveguiding around tight corners and splitters, and following band diagrams will for these reasons focus

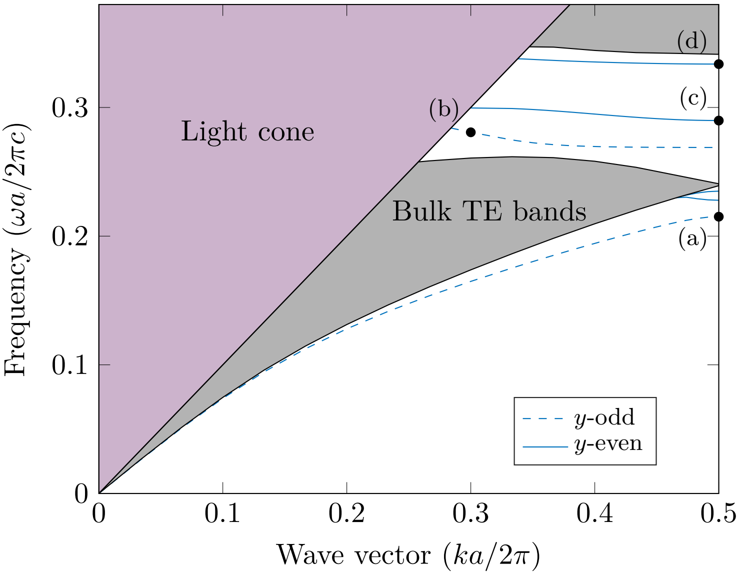

Figure 5.3.: Projected band structure of a W1 linear defect in an air-bridge PhC slab. H_z mode profiles in the slab center cross-section are shown for the labeled points (a) to (d) in Figure 5.4.

on the gap guided modes at **k**-vectors where they lie below the light line of their respective cladding materials.

Cross-sections of the H_z-field at the points (a) to (d) marked in Figure 5.3 are shown in Figure 5.4 to illustrate a few key properties of the various defect modes. The results are found to correspond well with those from a similar simulation discussed in Joannopoulos [18, Ch. 8]. Firstly, it is seen that the higher the frequency of a mode, the more nodes are observed in the y-direction, which is explained by the requirement of orthogonality for non-degenerate eigenstates in Hermitian eigenvalue problems, see Section 2.1.

Secondly, modes (a) and (b) are observed to have the opposite parity compared to (c) and (d) under reflections in the $y = 0$ plane intersecting the waveguide center. Although (a) and (b) appear to be y-even and (c) and (d) y-odd, the opposite is actually the case since **H** is a pseudovector [18, Ch. 7]. Following band diagrams will not depict the y-parity of defect modes since these will be the same as those in Figure 5.3.

Finally, the mode field patterns in (a), (c) and (d) are observed to perfectly match the periodicity of the lattice, which is because they according to Bloch's theorem are the product of a lattice-periodic function and a plane-wave which

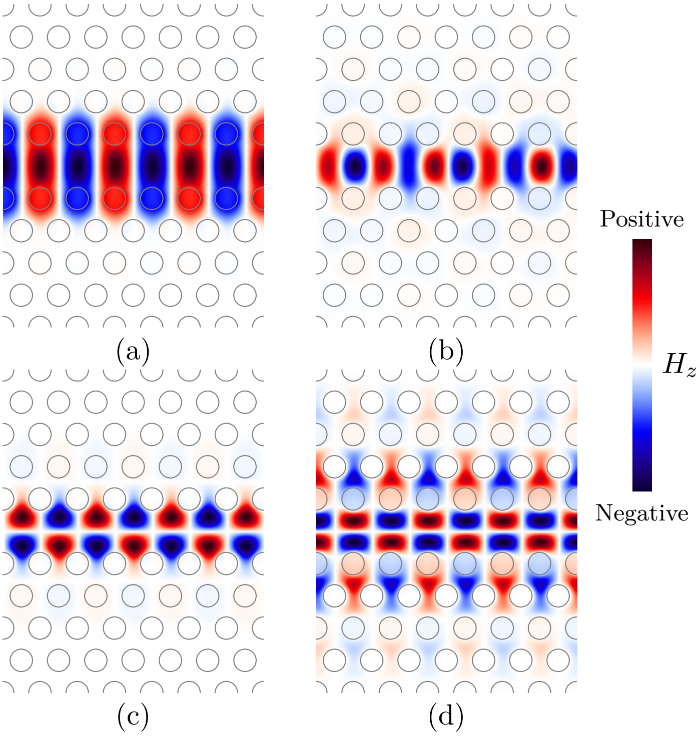

Figure 5.4.: H_z mode profiles in the center plane of an air-bridge slab missing-hole waveguide. The modes (a) to (d) correspond to the labeled points in the band diagram in Figure 5.3.

in this case (at the edge of the first Brillouin zone) has a spatial periodicity of $2a$. These modes are furthermore standing waves as seen from the zero slope dispersion in the band diagram. The mode in (c) is observed to be modulated by a plane-wave of a lower spatial frequency.

It is the ground mode in Figure 5.3 (b) which is of interest for waveguiding, since this has the largest frequency range below the light line, and, equally important, the appropriate y-parity for efficient excitation by a plane-wave input beam [18, Ch. 8]. Furthermore, it is also the mode with the largest frequency range of single mode operation. This is not observable from the band diagram computed using a supercell approximation with a fictive vertical periodicity, since this means that the eigenfrequencies computed for states that are inside the light cone are not valid (hence the purple shading). However, the fact that the ground mode is single also inside the light cone has been observed when using alternative computational methods which provide information about eigenstates above the light line, see e.g. Jamois et al. [30]. Alternatively, approximative 2D effective index simulations of linear defects as seen in Figure 5.5 (a) can be used to observe this since these do not assume a fictive vertical periodicity.

Figure 5.5 shows the band diagrams of W1 defect modes for the following PhC structures: 2D (a), air-bridge (b) and SOI slab (c). The wave vectors of interest range all the way to zero to the edge of the first BZ for the 2D structure, whereas the range is limited to the region below the light line for the finite-height 3D slabs. As before, the purple shaded regions depict the light cones for the respective cladding materials, and gray shaded regions correspond to continua of bulk TE states projected onto the Γ-K direction. Associated with each band diagram is an FDTD-simulated transmission spectrum through corresponding waveguides of finite length ($86a$). These spectra will be only briefly considered here, and are discussed further in Section 5.1.3.

The SOI band diagram in Figure 5.5 (c) shows a yellow shaded region which compared to the gray shaded regions is the equivalent projection of bulk TM states. This must be included since TE and TM modes can interact in this vertically asymmetric structure. A number of discrete modes of TM-like parity are observed inside the yellow shaded region, but this is merely an artifact of using a finite sized supercell in the direction normal to the waveguide (y). In reality, there is a continuum of TM-like eigenstates in this region, which would be obtained if using an infinite number of cladding periods between artificially separated waveguides in the supercell approximation. The discrete modes are however shown here to explain the presence of hybrid modes (green) where they interact with the guided TE-like modes.

The various linear defect band diagrams in Figure 5.5 have both similarities and important differences. Firstly, the ground mode is of the same character in all diagrams, having even z-parity[3], odd y-parity and a flat dispersion at the edge of the 1BZ. The main difference for the ground modes is that whereas the 2D structure shows a wide frequency range where it is useful for waveguiding, the presence of the light cones in the slab diagrams limits this range significantly.

Particularly the SOI waveguide ground mode is severely cut off by the SiO_2 light cone and bulk TM modes, leaving only a narrow range of width 5×10^{-4} below these continua of lossy states to which the mode can couple. For comparison, the ground mode for the air-bridge slab has a range below the light line of width 0.016, where a transmission of near unity is observed from the FDTD simulation. Furthermore, since the 2D structure has no light cone, all states within the band gap can propagate losslessly even when the translational symmetry is broken in bends and splitters. This range of high transmission across the 2D band gap is

---

[3] The ground mode for the SOI slab in Figure 5.5 (c) is found to have a z-parity close to unity (~ 0.994) near the band edge, making it almost z-even.

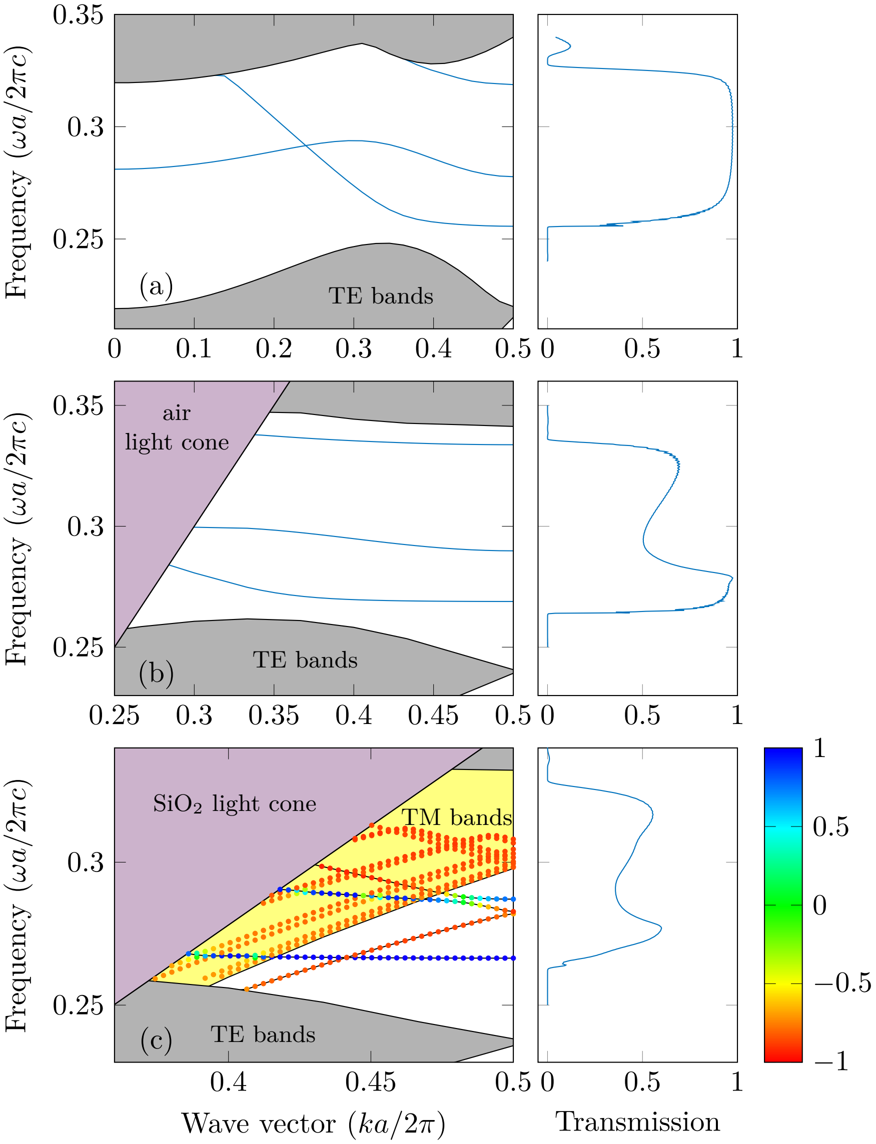

Figure 5.5.: Left: Band diagrams for W1 linear defects in a 2D PhC (a), air-bridge slab PhC (b) and SOI slab PhC (c). Right: FDTD simulated transmission spectra through corresponding waveguides of length $86a$. The colorbar corresponds to the computed z-parity of eigenstates in (c).

indeed observed in the FDTD-spectrum, and is fundamentally different from what is possible in slab waveguides where vertical losses occur for modes inside the light cone.

Also, all the ground modes in Figure 5.5 are as pointed out in Section 5.1.1 positioned near the lower end of the band gap, and improved light confinement in bends and splitters is expected if they were shifted closer to mid-gap. It is left as a suggestion for future work to investigate methods for dispersion tuning by structurally alternating the W1 defects. Importantly, the effects on waveguiding properties must be considered experimentally in addition to through simulations, since many suggested workarounds are based on introducing additional sidewalls [96] and thus possibly losses from fabrication induced roughness.

The frequencies for the onsets of FDTD transmission are observed to correlate well with the position of the ground modes – particularly for the 2D simulation. Small offsets of 9×10^{-4} and 3×10^{-3} are found in Figure 5.5 (b) and (c), which are attributed to the relatively coarse discretization of the computational domain used for 3D simulations ($a/16$ in all directions). As discussed in Kappeler et al. [101], coarse discretizations can result in differences in effective hole sizes. Nevertheless, important spectral features are only slightly shifted when comparing eigenmode computations with FDTD simulations, which for investigations of fundamental guiding/loss mechanisms is considered satisfactory.

An interesting effect is observed near the BZ edge in Figure 5.5 (c), which is an anticrossing between the index-guided TM-like mode (red) and the second lowest TE-like gap guided mode (blue). The two bands that are expected to intersect couple to one another and the bands repel, since there is no (absolute) opposing z-symmetry which prevents the bands from interacting. The observant reader may wonder why no anticrossing is observed where the ground TM-like mode intersects the ground TE-like mode, and the explanation is that these modes have opposite y-parities (y-even and y-odd, respectively), thus allowing an eigenmode degeneracy.

The undesirable small range where the SOI ground mode lies below both the light line and the projected TM-bands can be increased by changing the dimensional parameters of the structure. By choosing a thicker slab and smaller holes, the effective index of guided modes is expected to be increased such that they are positioned further below the light line. This is demonstrated in Settle et al. [100], where they use $h = 0.6a$ and $r = 0.25a$. Although low experimental propagation losses of 14 dB/cm are reported, the resulting reduced band gap size from these structural changes means that confinement in other functional components such as bends and splitters becomes less efficient. Also, since an important purpose of this investigation is to compare the properties of air-bridge and SOI slabs, the same dimensions are used for both systems even though different and better combinations of h and r may exist.

Table 5.1.: Physical parameters for the PhC design obtained when fixing the dimensionless operating frequency of 0.27 to the wavelength 1.55 µm.

Parameter	Dimensionless value	Physical value
a	1	420 nm
r	$0.3a$	125 nm
h	$0.55a$	230 nm

Introducing Physical Units

From the computed band diagrams in Figure 5.5, it is possible to determine a dimensionless frequency at which the device should operate. A natural choice is a frequency matching the guided mode below the light line, which will depend on whether air-bridge or SOI slabs are considered. However, the physical units serve mainly the purpose of translating simulated features to approximate but realistic physical parameters, and small differences in this choice does not fundamentally change these. Therefore, a dimensionless frequency of 0.27 is chosen, which serves to lock the structural device parameters to the physical values listed in Table 5.1, after determining the lattice constant as

$$\frac{\omega a}{2\pi c} = \frac{a}{\lambda} = \frac{a}{1.55\,\mu\text{m}} \quad \Rightarrow \quad a = 420\,\text{nm}.$$

It is pointed out that this choice of operating frequency is only an example, and that it can be adjusted at any point to tune features in band diagrams to any wavelength of choice. The only limitations lie in which structural dimensions that are possible to fabricate, and the optical properties of the material of choice at the given wavelengths.

To summarize the discussion of W1 linear defect waveguides, it is seen that suspended membrane PhCs support a significant frequency range below the light cone of intrinsically lossless propagation. For the physical dimensions determined for operation at 1.55 µm, this translates to a bandwidth of approximately 90 nm. The SOI waveguide does not share these characteristics, due to both the reduced size of the window below the SiO_2 light line and the presence of TM-like modes to which the ground mode can couple. In physical units, the bandwidth of the ground mode below the light line is ~ 9 nm, and also below the projected bulk TM modes, only 3 nm. This means that alternative SOI structures using different dimensional parameters (smaller holes, thicker slab) should be investigated to increase the available frequency range where efficient waveguiding can occur. Finally, the simulated 2D structure shares many of the fundamental features of the 3D slabs, which make them useful for e.g. qualitatively understanding the dispersion of guided modes inside the light cone.

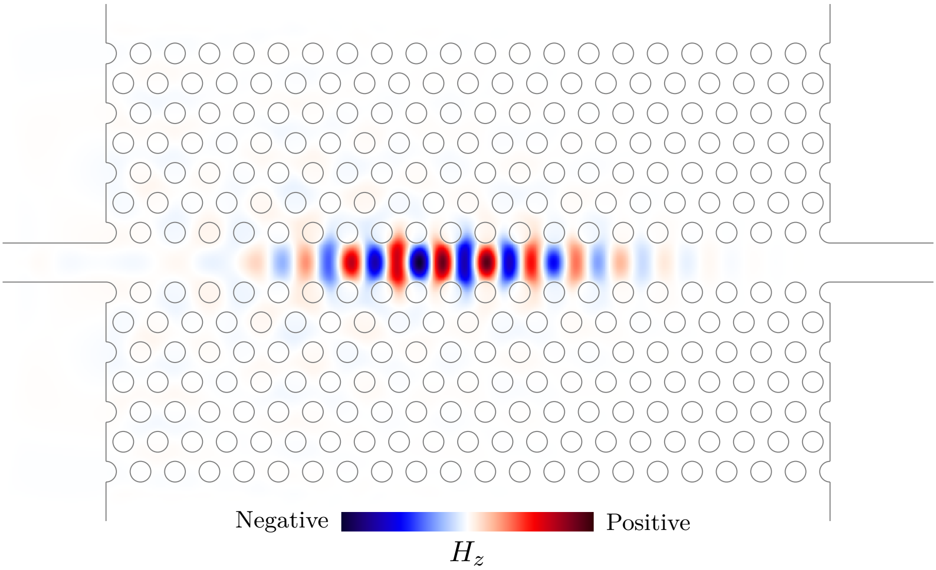

Figure 5.6.: Magnetic field profile time-slice of a Gaussian pulse propagating from left to right in a photonic crystal W1 waveguide.

5.1.3. Transmission Spectra

A general goal for most photonic crystal-based applications is to achieve high transmission through various structural components. In this section, transmission and propagation losses in linear defect waveguides are investigated using FDTD-simulations. Later, bends, power splitters are considered, before everything is combined to form complete Mach-Zehnder interferometers.

Using the simulation domain depicted in Figure 4.4, a Gaussian source with a center frequency of 0.29 and a bandwidth of 0.12 resulted after 60 (dimensionless) time units in the H_z-field profile seen in Figure 5.6. This frequency and bandwidth were chosen since it according to Figure 5.5 (a) is sufficient to cover the 2D band gap, and thus all frequencies of interest. At this particular time slice, the wave packet is seen to have propagated approximately halfway across the domain.

The frequency-dependent transmission through the structure is found by accumulation of the Fourier transformed fields at the defined output flux plane as the wave leaves the computational domain. This spectrum can be seen in Figure 5.7. As discussed in Section 4.1.2, it has been normalized to the transmission through a straight waveguide of the same width as the incoupling waveguides, meaning that transmission below one implies losses related to either reflections or propagation

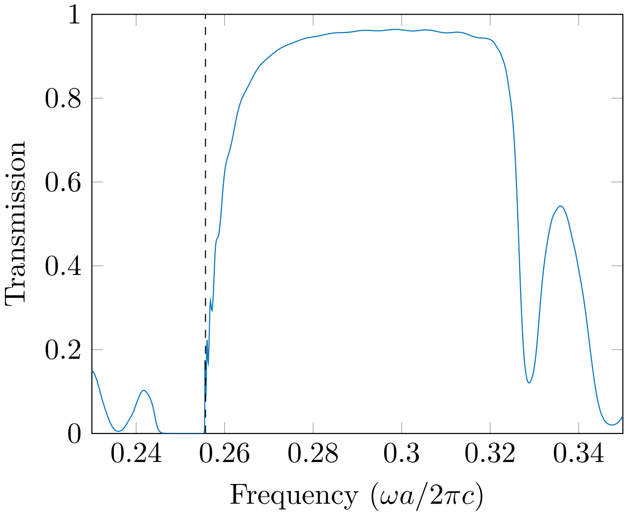

Figure 5.7.: FDTD-simulated transmission spectrum of a 2D PhC W1 waveguide of length $21a$. The dashed line corresponds to the lowest frequency of the ground mode in Figure 5.5 (a).

losses. Slight ripples in the spectrum are observed – particularly near the frequency onset of the ground mode. These features have been confirmed to be nonphysical computational artifacts caused by truncating the time domain-simulation before all frequency components have decayed to negligible values. A discussion of this is given in Appendix B.

Figure 5.7 serves in addition to demonstrating these numerical artifacts the purpose of introducing features in transmission spectra used in the following section to investigate PhC propagation losses. For instance, the frequency onset of the ground mode found from the band diagram in Figure 5.5 (a) shows an excellent agreement between the frequency-domain eigenmode computations and the time-domain simulated transmission spectra. Also, although not seen with this linearly scaled transmission axis, the transmission at frequencies between the ground mode and the lower edge of the bandgap drops to $\sim 10^{-7}$, even for this fairly short waveguide of 21 crystal periods. The transmission peaks observed below the band gap correspond to the index-guided modes seen in Figure 5.3.

Propagation Losses in Photonic Crystal Waveguides

An important property of photonic crystal waveguides is the losses experienced by propagating waves. Not all types of losses are caused by non-ideal experimental factors, but can be present even without material absorption or fabrication disorder. Both the magnitude and physical origin of such fundamental losses are crucial to understand and control in order to design functional PhC-based optical devices. In this section, focus is put on correlating the observed features in FDTD transmission spectra to the band structures computed in the previous section.

As discussed in Section 2.3, the nature of the losses will depend on the dimensionality of the simulations and on the possible presence of a symmetry-breaking substrate. Therefore, simulations of waveguides in both 2D, SOI slabs and air-bridge slabs are considered, see Figure 2.5 for illustrations. The simulation procedure for all three cases is identical: propagating a wave through a long PhC waveguide and measuring the flux spectra at several planes along the waveguide path. A waveguide length of $L = 101$ crystal periods was chosen, and flux spectra at 21 equidistant planes along this were computed. This waveguide length is chosen since it is significantly longer than many suggested designs of PhC devices, but still small enough to yield a manageable computation time on the equipment available (1-2 days for the 3D simulations).

Figure 5.8 shows a selection of these flux spectra computed at distances $0.2L$, $0.5L$ and $0.8L$ from the input. Distinct differences are observed for the different structures, and they are found to correlate excellently with the presence of the various loss mechanisms discussed in the following.

For the 2D PhC waveguide in Figure 5.8 (a), it is evident that the transmission is unchanged with distance in the frequency range corresponding to the band gap of the line defect band diagram in Figure 5.5 (a). This is as expected for a 2D PhC waveguide where only losses caused by poor in/out-coupling and evanescent penetration through a finite number of transverse cladding crystal periods are possible. The former is observed to be present since the transmission is slightly lower than one (approximately 0.97), but unchanged for different positions along the waveguide. The latter can be avoided by using “enough” cladding periods. In this case, seven cladding periods were used, which is observed to be sufficient from the lack of propagation losses in the spectra.

The 3D air-bridge waveguide in Figure 5.8 (b) differs from the 2D case by the presence of propagation losses for frequencies above ~ 0.28. This is seen in Figure 5.5 (b) to correspond to the frequency where the ground mode crosses the light line. These spectra thus demonstrate the vertical loss mechanism caused by radiation modes that lie above the light line. As discussed in Section 2.3, modes inside the light cone are not confined to the plane of the slab, and can leak into the background. There is nevertheless a band between the frequencies 0.265 and 0.281 where propagation losses theoretically vanish, since the only guided TE-like mode lies below the light line in this region. The transmission in this range is approximately 0.95, and the offset from unity is attributed to non-ideal incoupling from the strip waveguide into the slab. The *propagation losses* are however close to zero in this range since the transmission is independent of position along the

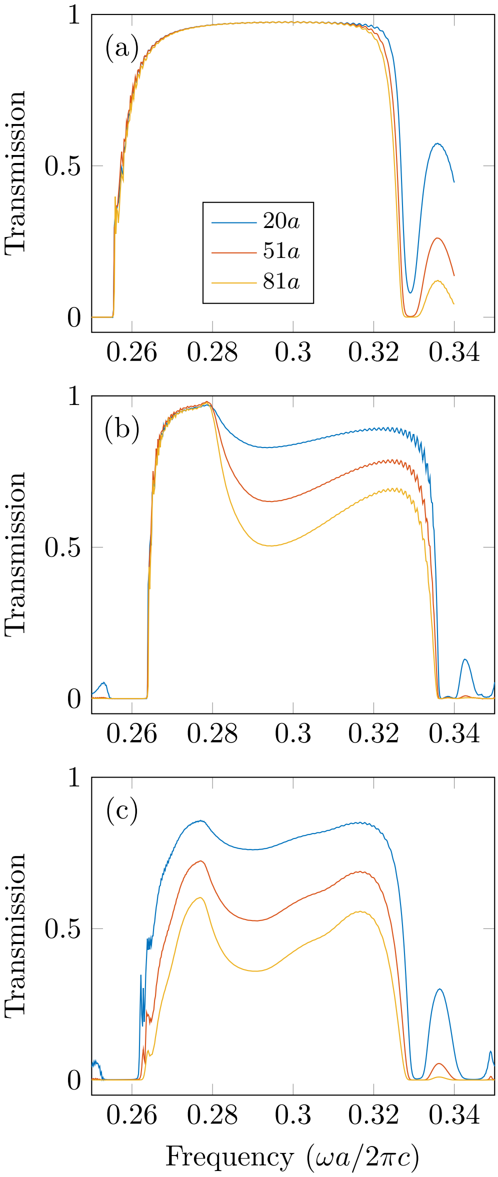

Figure 5.8.: Transmission spectra computed after three lengths of propagation for different types of PhC waveguides: (a) 2D, (b) air-bridge slab (c) SOI slab. The legend in (a) applies to all plots.

PhC waveguide.

Whereas the air-bridge waveguide shows a frequency range of near lossless propagation, losses are evident at all frequencies for the SOI waveguide in Figure 5.8 (c). The explanation is that the symmetry-breaking bottom oxide allows for the TE-like modes used to excite the system to couple to TM-like modes. There is no band gap for TM-like modes in this type of hole-slab photonic crystal, which means they are extended in the plane of the slab for all frequencies. The energy thus radiates away within the plane of periodicity into the PML-layers that lie outside the seven waveguide cladding periods seen in Figure 4.4. Two distinct drops in transmission appear to be present near the onset of the ground mode. The first is assumed to correspond to the point where the ground mode enters the continuum of projected bulk TE-modes in Figure 5.5 (c), and the second to the frequency where the mode enters the light cone.

It is emphasized that the above discussion of losses in 3D systems caused by coupling to radiation modes and TM-like modes is of qualitative nature. The leakage rate and magnitude of propagation losses depend not only on the presence of such modes, but also on how strong the polarization mixing is at a particular frequency and the dispersion characteristics of the guided modes inside the light cone [30]. Losses are for example particularly strong for leaky modes that have small group velocities, which can be observed for example in the SOI-waveguide at the onset of the ground mode which has a nearly flat dispersion at that frequency.

The polarization mixing caused by the vertical asymmetry in SOI-slabs is weak because the oxide cladding has a refractive index close to one. This supports the observation in Figure 5.8 (c) of only slightly higher losses in the SOI waveguide compared to the air-bridge waveguide. Propagation losses from the SOI vertical asymmetry can indeed for many practical purposes be small enough to be acceptable, depending on the particular application of interest [18, Ch. 8]. The waveguide investigated here has a length of $101a$, which is significantly longer than many suggested designs for PhC devices. Thus, the results motivate that – depending on the application – the simplicity of fabricating SOI slab structures may outweigh the problem of increased losses.

A quantification of propagation losses is done using a simulated cut-back technique. The approach is similar to those used by others [101, 102]. It is conventional to use dB per distance to quantify propagation losses, where the power loss α is given by

$$\alpha = 10\log\left(\frac{P_{\text{out}}}{P_{\text{in}}}\right). \tag{5.1}$$

At each frequency in the transmission spectra, the transmission after different lengths of propagation is fitted to an exponential decay[4]. An example is shown for

---

[4] The curve fitting is done in MATLAB® using a non-linear regression (least square error minimization) to single exponentials prior to converting the values to dB.

the frequency 0.29 in Figure 5.8 (c), where the corresponding position dependent transmission is plotted in Figure 5.9. Note that the transmission was computed at more than the three distances depicted in Figure 5.8. In principle, only two points are sufficient for using the cut-back method, but more points are used to reduce the effects of computational noise. The exponential decay of the fitted curve is used to extract the propagation loss at this particular frequency.

Using the same procedure for all of the sampled frequencies, the frequency dependent propagation losses for the air-bridge and SOI waveguides are found and can be seen in Figure 5.10. The 2D waveguide did not show any propagation losses within the numerical noise present in the spectrum (as expected), and is for that reason not considered. The losses are presented in physical units corresponding to the lattice constant $a = 420\,\text{nm}$, to get physical values that can be compared to the work of others.

The SOI waveguide is observed to have propagation losses at all frequencies, as expected from previous discussions. The minimum loss is found at the frequency 0.277 to be 59 dB/mm. This may appear unreasonably high, but it is noted that the physical length of PhC devices can be on the order of only some 10 µm, in which case it can be acceptable. The air-bridge slab shows a frequency range of intrinsically zero propagation losses, although some noise in the loss spectrum is observed. The performance of devices designed to operate in these regions will thus be governed by experimental limitations in terms of non-ideal fabrication processes. It is also seen that the losses that are introduced above the light line are acceptable in the case of small devices, with a maximum loss of 84 dB/mm occuring near mid-gap. The frequency dependent losses for the air-bridge slab are observed to agree both qualitatively and quantitatively with the results reported in Cryan et al. [102] where a similar structure was investigated.

Bends and Splitters

A functional Mach-Zehnder interferometer requires bends and power splitters in addition to linear waveguides. The hexagonal lattice used in this project dictates a bend angle of 60°, and splitters of 120°, as depicted in Figure 2.9. The structures formed this way by simply removing the appropriate rows of holes will from here be referred to as *generic* bends and splitters.

It is not straightforward to introduce PhC bends and splitters whilst maintaining the broadband transmission that exists for unperturbed linear waveguides, since strong back-reflections and increased out-of-plane losses typically result in small and narrow band transmission. Figure 5.11 demonstrates this by showing the transmission through generic bends and splitters for 2D PhCs, air-bridge slabs and SOI slabs. The transmission through the splitters correspond to the *combined* output from the two arms. Using the 2D transmission spectra as references, particularly two undesirable features are observed. Firstly, the Y-splitter

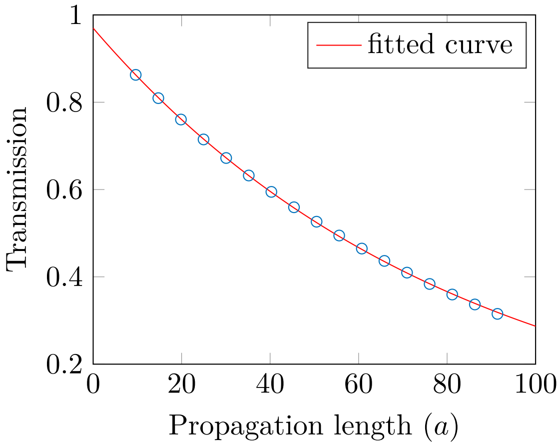

Figure 5.9.: Measured transmission for an SOI waveguide at the frequency 0.29 after different propagation lengths (see Figure 5.8 (c)). The solid line shows the corresponding single-exponential fitted curve.

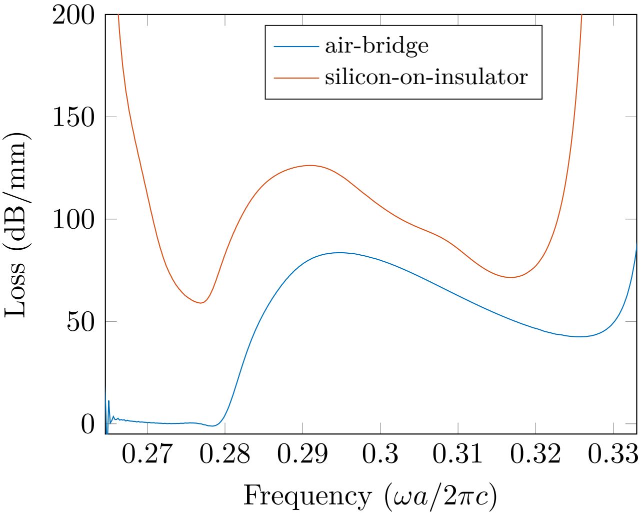

Figure 5.10.: FDTD-simulated propagation losses for W1 waveguides in air-bridge and SOI photonic crystals.

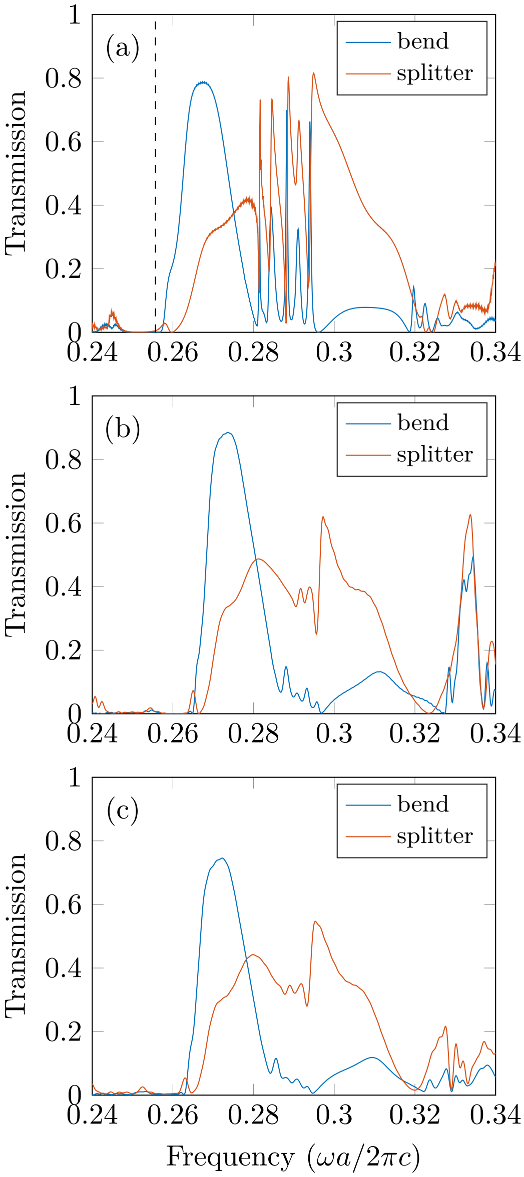

Figure 5.11.: Transmission spectra for generic 60° bends and Y-splitters for (a) 2D PhC, (b) air-bridge PhC and (c) SOI PhC. The dashed line in (a) marks the onset of the ground mode found from eigenmode computations in Figure 5.5 (a).

transmission at frequencies near the onset of the ground mode is small, where more than half of the incident power is reflected for frequencies below 0.28.

Secondly, for frequencies between 0.28 and 0.295, both spectra have an erratic appearance of sharp peaks and valleys. From inspection of the band diagram in Figure 5.5 (a), this is confirmed to correspond to the frequency range where the ground mode is not single. Since the translational symmetry along the linear defects is broken in the bend/splitter, $\mathbf{k}$ is not a conserved quantity and the second-lowest gap guided mode can be excited. This particular mode has an even y-parity, which means that it couples poorly to the y-odd mode that is supported in the strip waveguides used for in/out-coupling to the photonic crystal. Thus, most of the power in the y-even mode is reflected back into the crystal, causing the observed sharp Fabry-Pérot resonances in the transmission spectra.

Regarding the transmission in the slab structures, most of the same features are present as those seen for the 2D simulation. One notable difference is the much less pronounced resonances at the frequencies where the ground mode couples to the second lowest (y-even) mode. Since the modes lie inside the light cone at these frequencies, the excited y-even modes are assumed to leak into the vertical cladding (or couple to TM-like modes in the SOI slab), preventing the strong resonances.

The conclusion from observing mode coupling is that the device must be designed to operate at frequencies where the ground mode is single. In 2D, this can be both below and above mid-gap, but for real 3D slabs, the low frequency side is highly preferred because of the presence of the slab cladding light cones. A complete Mach-Zehnder interferometer built with generic bends and splitters is assumed to have poor transmission characteristics, primarily due to the poor Y-splitter transmission characteristics.

A structural optimization procedure with the goal of increasing the transmission for bends and Y-splitters at low frequencies (< 0.28 in 2D) is thus attempted, as described in Section 4.1.2. The procedure was for simplicity based on brute force simulations of several combinations of the chosen structural parameters. For the splitters and bends, 700 and 100 combinations were tested, respectively. The averaged transmissions in the single mode range of the ground mode (between frequency 0.2557 and 0.2777) were then sorted to detect the structural parameters that gave the highest transmission. The resulting optimum structures and their transmission spectra are shown in Figure 5.12. For comparison purposes, the transmission spectra of generic bends and splitters are also included. The performance is observed to be considerably improved in both cases, having a broadband and high transmission of approximately 0.8 in the desired frequency range of operation.

When investigating the sorted lists of structures that gave the highest transmission, focus was put on detecting trends in the structural parameters. All the structures with the best results were found to have similar parameters to the ones

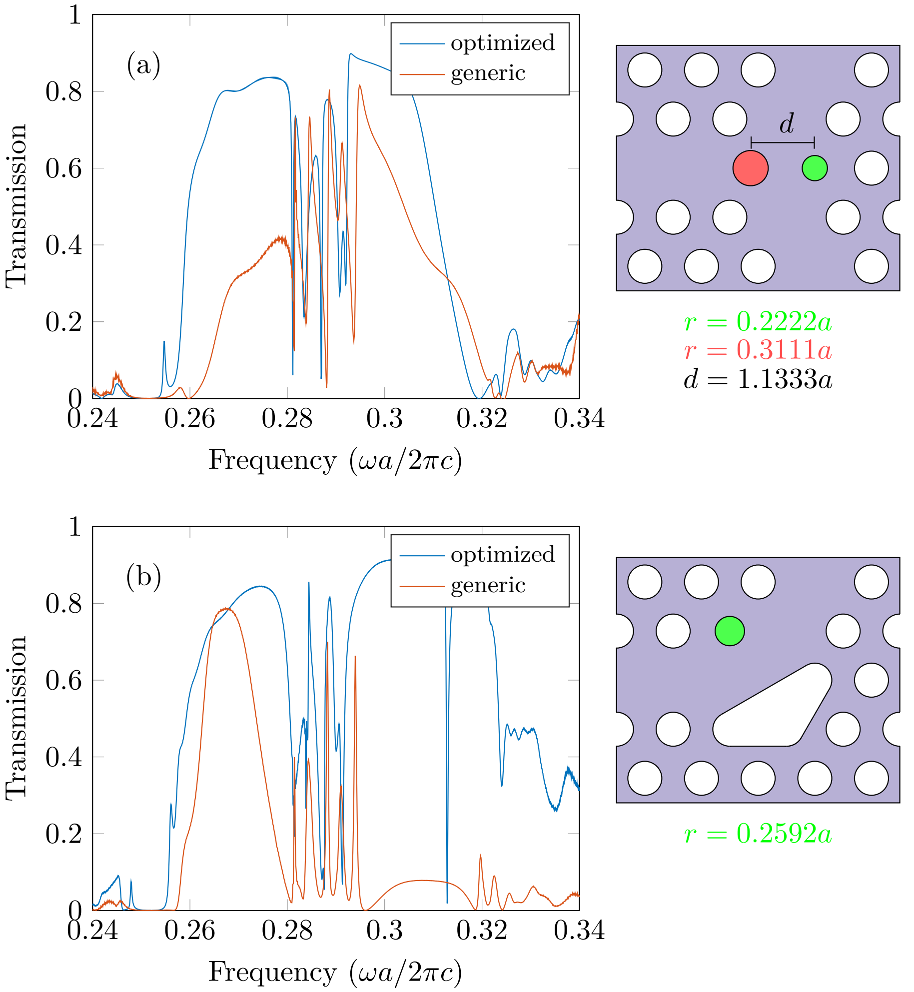

Figure 5.12.: Transmission spectrum of an optimized Y-splitter (a) and a 60° bend (b). The optimized structural parameters are indicated in the corresponding schematics to the right.

in Figure 5.12, and also similar-appearing transmission spectra. This indicates that the suggested designs are not highly sensitive to structural changes, which is advantageous in terms being tolerant to fabrication errors. It is pointed out that this brute force method of testing different parameters can be improved by clever algorithms that search some specified parameter space automatically instead of testing “all” combinations. More advanced approaches for structural optimization can give better results, and this is left as a suggestion for future work. Still, the spectra in Figure 5.12 have already promising characteristics.

Since out-of-plane losses can occur for real 3D slabs, it is important to simulate the performance of the optimized components also for these structures. The transmission spectra are found in Figure 5.13 together with the corresponding spectra of their generic counterparts. The transmission is as expected lower than in 2D, but nevertheless improved compared to the generic implementations, with broadband transmission above 0.6 for both structures. Thus, the procedure of optimizing the structure in 2D is seen to yield results that are to a large degree transferable to the 3D slabs.

Mach-Zehnder Interferometer

After combining linear waveguide segments, 60° bends and Y-junctions in the way illustrated in Figure 2.9, the transmission spectra in Figure 5.14 were obtained. Only the frequency region below the onset of the second-lowest guided mode is considered, since this is the desired range of operation.

All structures in Figure 5.14 show broadband transmission of sufficient magnitude to be easily measured in practice. Converted to the physical units corresponding to a lattice period of 420 nm, the 2D MZI has a 3 dB bandwidth of 99 nm. The same trend as observed in other simulations of reduced transmission is evident when going from 2D to air-bridge slabs and finally to SOI slabs. The air-bridge MZI is found to have a 3 dB bandwidth of 53 nm, and the SOI MZI a 6 dB bandwidth of 69 nm. Large bandwidths are desirable since they reduce the sensitivity to fabrication disorder, although quantitative considerations of this is outside the scope of this work.

Figure 5.15 shows electric field energy density and H_z-field profiles at a frequency of 0.27, and illustrate the improvements in transmission properties when using optimized bends and Y-splitters in the MZI. In Figure 5.14 (a), a significant improvement is observed from separate narrow transmission peaks for the generic implementation to a broadband high transmission for the optimized structure. The limiting component that is mainly responsible for the narrow transmission peaks is the generic Y-junction which reflects most of the incident power. This is as expected from the transmission spectra of generic Y-splitters in Figure 5.11 (a), and can be directly observed in the uppermost field profile in Figure 5.15.

The lower two field profiles in Figure 5.15 show that the optimized Y-splitters

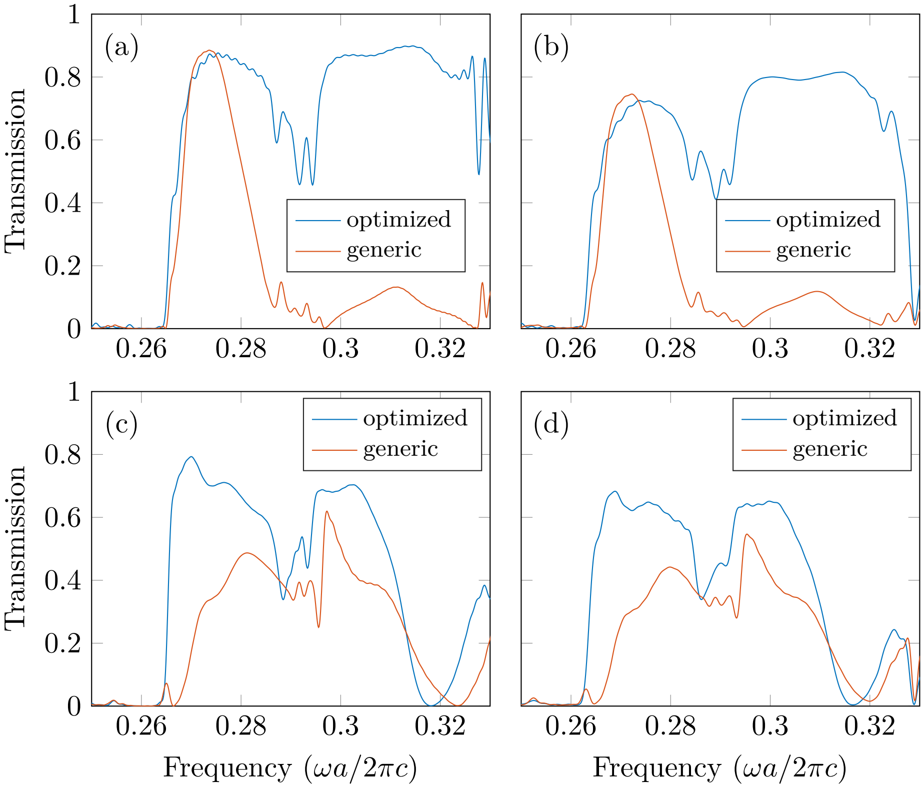

Figure 5.13.: Transmission spectra of structurally optimized bends and Y-junctions from 3D simulations. (a): air-bridge bend, (b): SOI bend, (c): air-bridge Y-splitter, (d): SOI Y-splitter. Spectra of generic components are included for comparison.

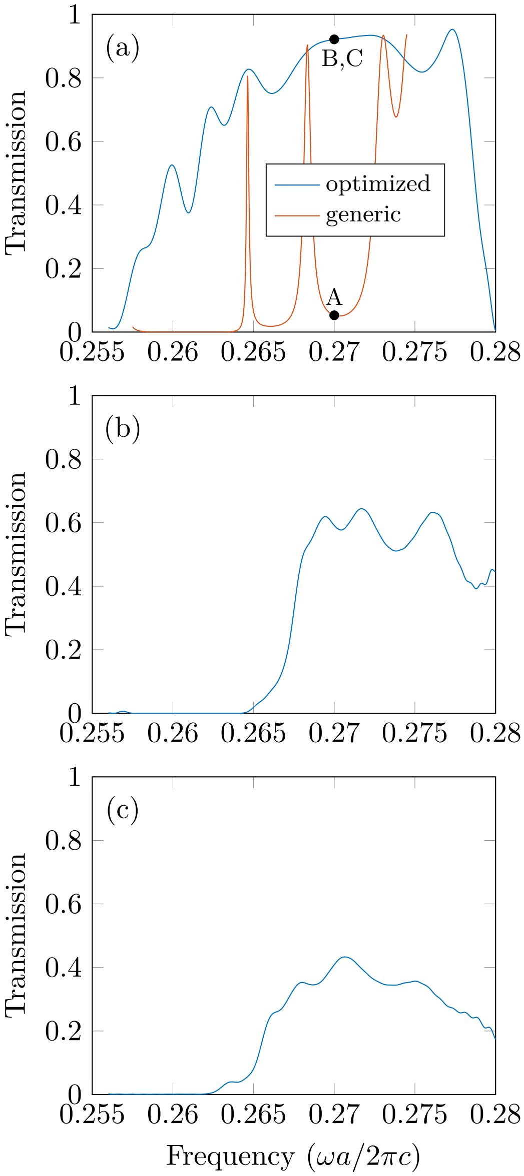

Figure 5.14.: Transmission spectra of balanced Mach-Zehnder interferometers for (a) a 2D structure, (b) air-bridge slab and (c) SOI slab. In (a), spectra for structures with both generic and optimized Y-splitters are shown. Field profiles at the points A-C are shown in Figure 5.15.

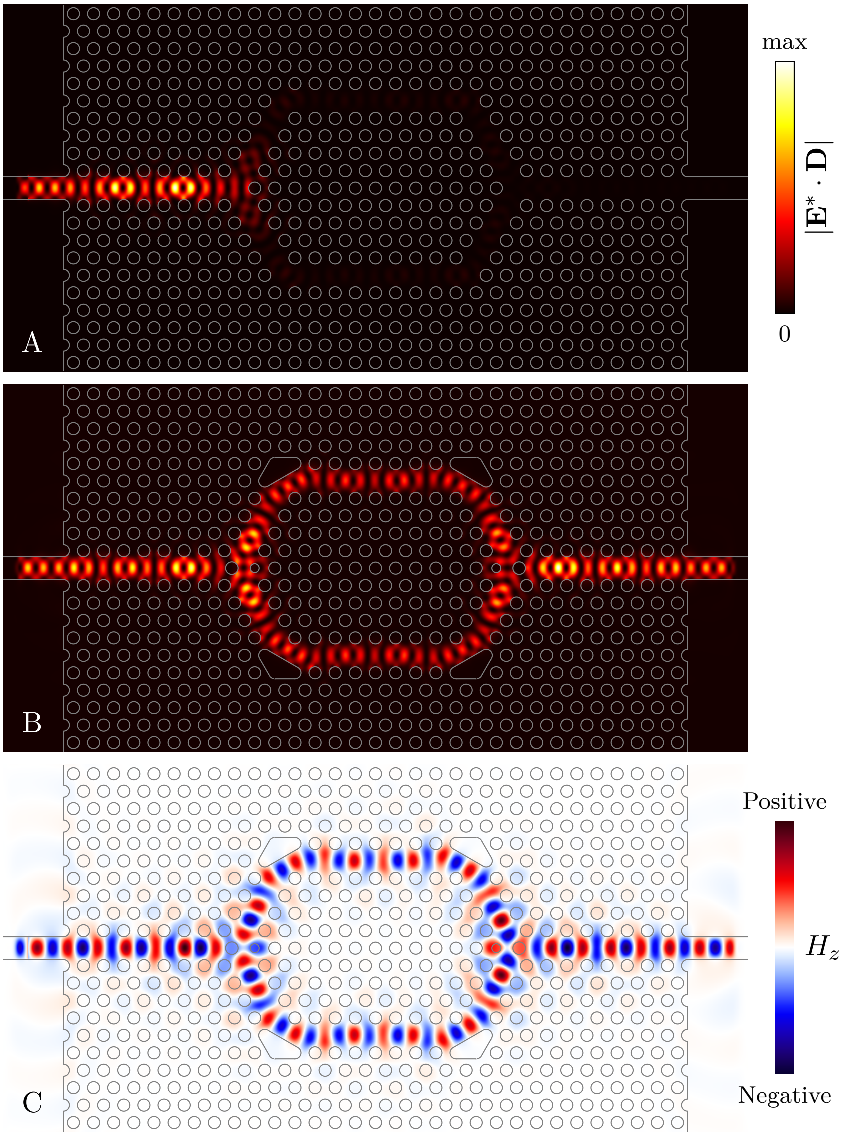

Figure 5.15.: E-field energy densities and H_z-field mode profile for the points A-C marked in the transmission spectra in Figure 5.14 (a).

and bends perform as they were designed to, by gently steering the light and not relying on tuned resonant cavities resulting in strong field enhancements. Also, only the ground (single) mode is guided around the bends, and the H_z field profile in the straight waveguide sections appears similar to that found from eigenmode computations of linear defects in Figure 5.4 (b).

Although the transmission spectra in Figure 5.14 all show high and broadband transmission, there are still oscillations that are believed to correspond to cavities formed between bends and splitters due to remaining reflections. Is it believed that more advanced structural optimizations can improve this, but it is not attempted in this project.

5.1.4. Biosensing

The idea behind utilizing the Mach-Zehnder interferometer in a biosensor is to functionalize one of the arms with receptors. A layer of biological material can then build up on the walls of this *sensing* arm, which is illustrated in Figure 4.6. The biolayers change the surface refractive index, such that waves propagating in the sensing arm experience a phase shift relative to waves in the *reference* arm. This section aims to investigate the effects of adding such biolayers to the inner walls of photonic crystal holes, and explore this technique as a transduction method for optical biosensing.

All simulations in this section are performed in 2D, since the spatial resolution needed for resolving differences in thin biolayers with realistic thicknesses around 10 nm was found too high for 3D simulations with the computational equipment available. However, the high degree of correspondence between simulation results from 2D and real 3D slabs presented so far indicate that qualitative findings may be largely transferable.

After adding a model biolayer of dimensionless thickness 0.05 to the holes in the sensing arm of a structurally optimized Mach-Zehnder interferometer, the transmission spectrum in Figure 5.16 was obtained. In physical units, this layer thickness corresponds to 22 nm. The spectrum of the balanced interferometer is included for reference, and a drastic change in appearance is observed, where sharp dips in transmission have occurred at several frequencies.

The physical origin of the transmission dips is clarified from observing the H_z-field profile at a simulation time long after the source is turned off. The field profile is shown in Figure 5.17 from which it is evident that the central part of the device functions as a ring resonator, which at certain frequencies couples no power into the output waveguide. It is observed that the H_z phase at the output is such that a y-even mode is excited into the outcoupling PhC waveguide[5]. As evident

---

[5] As mentioned in Section 5.1.2, a H_z field pattern that appears to have odd y-parity is actually a y-even mode.

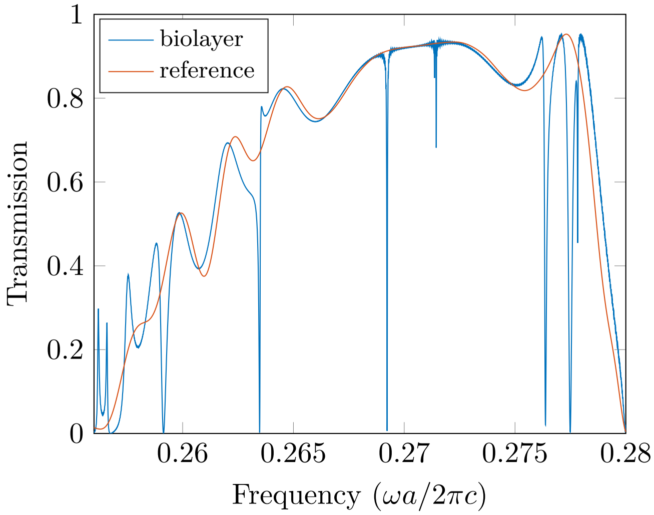

Figure 5.16.: Transmission spectrum of a Mach-Zehnder interferometer with a biolayer of thickness 0.05 added to the sensing arm. The reference spectrum of the balanced MZI is also shown.

from the linear defect band diagram in Figure 5.5 (a), no such defect modes are supported at the simulation frequency (< 0.28), resulting in an evanescent decay away from the ring.

Noise in the spectrum is observed near the dips, which is caused by truncation of the simulation before all fields have decayed to negligible values, see Appendix B. Although the simulation was run for as much as 40 000 dimensionless time units, some of the resonant modes have very high Q-factors and thus decay slowly. In fact, during the simulation, a harmonic inversion was invoked to investigate properties of these resonance modes. The computational method of harmonic inversion is briefly outlined in Appendix B. Of all the resonances, the two centred around the frequency 0.27 have the highest Q-factors of 9200 and 22 000 at frequencies 0.2692 and 0.2714, respectively, which explains why considerable amounts of power remained in the computational domain after 40 000 time units.

It is noted that the dip at 0.2714 is expected to be deeper than seen in the trasmission spectrum due to a frequency sampling too wide to fully capture the narrow resonance. It is also expected that these resonances are weaker for 3D structures due to cladding losses from excitation of radiation modes.

Compared to the balanced interferometer in Figure 5.15 (c) where the waves in the two arms are seen to add in phase to launch a y-odd propagating mode, it is

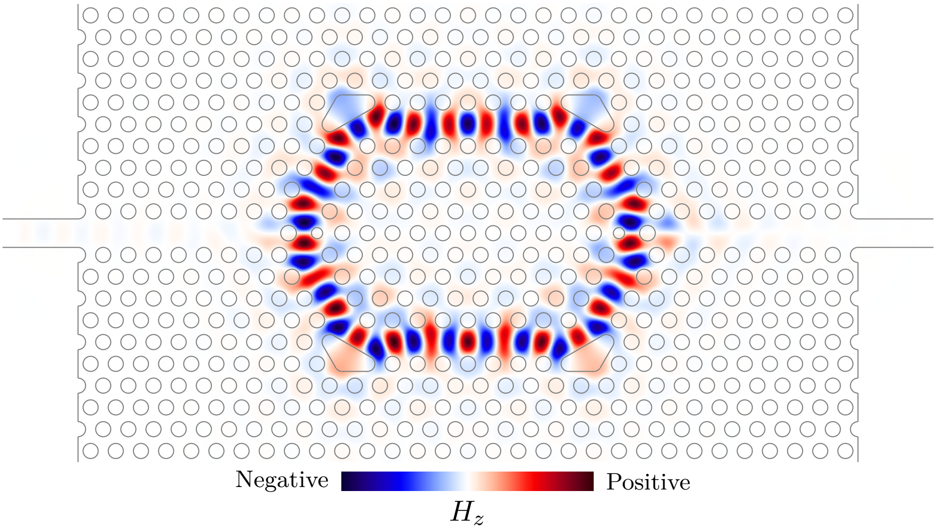

Figure 5.17.: H_z field profile of a Mach-Zehnder interferometer having a 22 nm thick biolayer on the hole walls in the sensing arm.

clear in Figure 5.17 that the phase of the wave in the sensing arm (top) is shifted approximately by π relative to the field profile in the reference arm (bottom). In simpler words, the sign of H_z is flipped. How did this happen? Although the biolayers in the sensing arm cause a phase change relative to the reference arm upon propagation, it is not believed to amount to π for a single pass through the structure. Firstly, if this was the case, a more conventional interference spectrum would be expected where the intensity varies sinusoidally as a function of frequency. The picture would be somewhat obscured by the presence of group velocity dispersion in the PhC waveguides, but this can not explain the distinct dips in transmission. Also, multiple roundtrips for the two counter-propagating waves in the ring cannot explain the phase difference, since both waves pass the sensing arm once per roundtrip which prevents a phase difference accumulation.

Secondly, investigations of wave propagation in straight PhC waveguides with and without biolayers like those used above resulted in a phase shift of approximately $0.01\pi/a$. In other words, 100 periods would be necessary to achieve full modulation with this biolayer thickness at the simulation frequency 0.27, which is a factor 14 longer than the length of the biolayer-coated part of the sensing arm. From this, it is believed that resonant enhancement in cavities formed between the bends and/or Y-junctions is responsible for the accumulation of a π phase difference between the two interferometer arms.

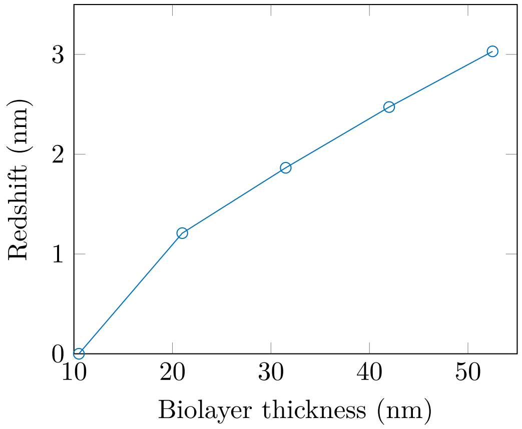

Figure 5.18.: Redshift of the transmission dip near frequency 0.269 in Figure 5.17 for biolayers of different thicknesses.

Figure 5.18 shows the spectral dependency of the transmission dip near frequency 0.269 for biolayers of different thicknesses in the sensing arm, where physical units are used. The resonance wavelength for all thicknesses is referenced to that for the thinnest coating of 11 nm, since there are no resonance dip without the biolayer. The redshift $\Delta\lambda$ is seen to increase almost linearly with the coating thickness t, which is also demonstrated by Lee et al. [14] in similar simulations and experiments with a cavity-based PhC biosensor. The slope of the curve $\Delta\lambda/\Delta t \approx 0.07$ means the resonance wavelength varies little with the thickness of the added biolayer, and indicates that the guided modes are highly confined to the silicon slab and only interact with the innermost part of the coating. For comparison, the sensitivity obtained by Lee et al. [14] was $\Delta\lambda/\Delta t \approx 1.4$ when they covered the entire sensor, and ~ 0.34 when only covering the local region around their cavity defect. Despite a lower sensitivity when comparing the pure resonance-based transduction with the signal from the MZI, the strength in the latter lies in possible cancellation of common-mode noise such as thermal expansion and changes in the bulk refractive index of a test solution. These sensing aspects are not discussed in Lee et al. [14], but are expected to be significant contributors to resonance shifts in addition to changes from specific binding of biomaterials, which require careful environmental control and instrumental setups.

There are a number of parameters that can be adjusted with the goal of enhancing the sensor sensitivity, and a few are suggested here. Firstly, it is imaginable that 3D simulations where coatings are added also to the top surface can result in higher sensitivity. It is also possible to design waveguides with the purpose of maximizing the interaction between the field and biolayers by increasing the fraction of optical power in the regions where the layers build up. This has already been demonstrated by using novel photonic crystal slot cavities, where the optical field is localized in slots of a low index medium (air/buffer solution) by utilizing photonic band gaps [103]. The sensitivity can furthermore be increased by using longer sensing pathlengths, however at the expense of increasing the device size. Finally, it is suggested to add resonators side-coupled to the sensing arm to enhance the interaction, which has been investigated numerically [104].

The investigation of the sensor device is left as a proof of principle of how a photonic crystal Mach-Zehnder interferometer can detect the build-up of biomaterials on functionalized sidewalls through modulations in output power. Among the promising characteristics are the drastic changes occurring in the transmission spectrum from the presence of small amounts of material, and the small size of the device ($\sim 10 \times 10\,\mu\text{m}^2$) which make multiplexed sensing possible with dense arrays of sensors functionalized differently and tuned to resonate at different frequencies. Several challenges exist for realizing working devices similar to that suggested. Many apply to nanophotonic label-free refractive index sensors in general, such as integration with microfluidics, surface biofunctionalization and possible destructive sensitivity to fabrication disorder. In addition, challenges that are more specific to PhC-based sensors and the interferometric device must be considered. For example, the functionalization must be local, with an accuracy on the order of a few µm, which is slightly lower than the ~10 µm currently achievable resolution with inkjet bioprinting [44]. Biomaterial infiltration into narrow photonic crystal holes may also be challenging.

5.1.5. Simulations Summary

The simulations in this work have been based on building a photonic crystal Mach-Zehnder interferometer from basic structural components – waveguides, Y-splitters and 60° bends. These components have been simulated individually and optimized for high transmission in desired overlapping frequency regions, before being combined to a complete MZI where the effects of adding coatings of biomaterial to the sensing arm have been studied. Eigenmode computations of guided modes in photonic crystals have been done together with complementary FDTD-simulations to find transmission spectra of finite structures. Focus has been put on correlating 3D simulations of PhC slabs with their 2D effective index approximations, since the latter is a commonly used method for structural optimization of nanophotonic devices due to the much lower requirements of computational power.

The most basic part of any waveguiding-based photonic circuit is of course the waveguides. Therefore, single missing-row (W1) waveguides were considered thoroughly with the goal of revealing intrinsic loss mechanisms and their relationship to the design of different waveguides. In particular, 2D PhC waveguides were found to, as expected, only suffer from losses caused by non-ideal incoupling, whereas additional loss channels are introduced for finite-thickness slabs. For vertically symmetric *air-bridge* slabs, coupling to a continuum of modes in the air cladding (radiation modes) was demonstrated for guided modes above the light line. The same mechanism exists for the SiO_2 cladding of silicon-on-insulator PhC slabs, however the vertical asymmetry breaks the absolute opposing z-parity of TE-like and TM-like modes such that they are no longer orthogonal. In hexagonal air-hole slab PhC, there is normally only a band gap for TE modes, which means that TM modes are extended in the plane in periodicity and thus constitute a loss channel whenever there is polarization mixing. Band diagrams of eigenmodes in linear defect waveguides were used to understand features of FDTD-simulated transmission spectra, and excellent correspondence between the two complementary computational methods have generally been found.

In addition to qualitative studies of fundamental loss mechanisms, numerical FDTD cut-back simulations of PhC waveguides were used to quantify propagation losses. Lossless propagation was demonstrated for 2D PhC waveguides. Also, a frequency range lossless propagation of 90 nm bandwidth was demonstrated for the air-bridge slab, which was assigned to the frequency range where the ground guided mode lies below the light line. For the SOI slab, losses were observed for all frequencies due to coupling between TE-like and TM-like modes, and the minimum loss of 59 dB/mm was obtained. Although appearing unreasonably high, the power of PhC integrated photonics lies in miniaturization such that the losses can be tolerable for structures with lengths on the order of 10 µm.

The transmission properties of bends and beam splitters formed without any structural optimization were found from FDTD-simulations to be poor. Particularly for the splitters, the transmission was low for frequencies where the guided modes lie below the light line, which is the desired frequency range of operation. Through local junction structuring with the goal of suppressing higher order mode excitation by reducing the optical volume, the transmission properties of both components were considerably improved. Although these optimizations were performed in 2D, the results were found to be transferable to 3D slabs. With waveguides, beam splitters and bends combined to a complete Mach-Zehnder interferometer, the optimized components resulted in high and broadband transmission through the complete device. Specifically, the 3D air-bridge MZI had a 3 dB bandwidth of 53 nm, whereas the SOI MZI had a 6 dB bandwidth of 69 nm.

The final simulations investigated the possibility of using the suggested MZI as a biosensor detecting the build-up of material in the sensing arm. High-Q resonances with values up to 22 000 (2D simulations) of the MZI ring were formed from the presence of biolayers of thicknesses down to 11 nm, with distinct dips in transmission at these frequencies. The phase of the standing waves were seen to be shifted by π in the two interferometer arms, which lead to poor coupling into the output PhC waveguide at the resonance frequencies due to symmetry mismatch between the fields in the resonator and the guided mode supported in the waveguide. A redshift of the resonance frequencies was observed for increasing thicknesses of the biolayer, however with a sensitivity lower by more than an order of magnitude than that achieved in similar work of others [14]. Methods to increase the sensor sensitivity by increasing the overlap between the optical field and the region where the layer forms was suggested, e.g. by introducing side-coupled cavities to the sensing arm, or using slot PhC waveguides. The current design is mostly suitable for threshold-based detection, where the advantage of the sensor principle lies in the drastic change in transmission spectra between the balanced MZI and in the presence of biolayers.

5.2. Fabrication

This section presents results from fabrication of silicon-on-insulator photonic crystal devices. First, the results from early fabricated structures are presented. Since several of the processes used are based on previous work in the research group on optimizing the fabrication of silicon nanophotonic structures, it was desirable to perform the entire fabrication scheme in order to get an overview of possible problems and processes that could require further optimization. Despite previous attempts, successful light coupling through fabricated devices had not been achieved prior to this work, which pointed in the direction of one or more steps needing considerable improvement. Succeeding subsections present results from systematic attempts of improving the quality of individual processes compared to the preliminary devices.

5.2.1. Early Fabricated Structures

The scanning electron micrographs shown below serve to illustrate the quality of the entire initial fabrication process and discuss problems and their possible origins. This will serve to motivate the upcoming sections on improving the processes.

Line Edge Roughness

Common for all initially fabricated samples was the presence of considerable line edge roughness. This is shown in Figure 5.19, where it is seen both in PhC holes and strip waveguides. For typical strip waveguides, the RMS roughness was measured to be approximately 5 nm using the image analysis method discussed in Appendix C. The roughness was early assumed to be caused by a poor lithography process, since the etch recipe used has previously demonstrated sidewalls of far better quality [6]. Specifically, the EBL exposure dose and the development process are believed to be the main factors, which is further investigated in Section 5.2.3.

Varying Pattern Quality

Initial devices fabricated with nominally identical processes resulted in large variations in pattern quality – even for different regions on a single sample. As an example of this, Figure 5.20 shows etched hole patterns in different positions on a sample where the pattern in (a) is horrible, whereas that in (b) is much better, apart from considerable edge roughness.

Inconsistencies of this severity are believed not to originate from the exposure or etching processes, which should be fairly even across a sample within a

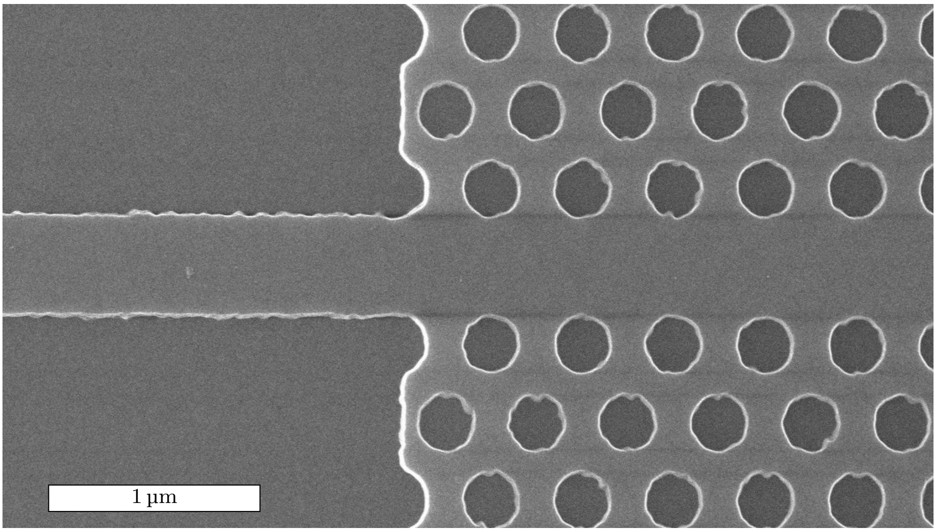

Figure 5.19.: SEM image of the coupling region between a strip waveguide and photonic crystal waveguide, showing ragged sidewall edges.

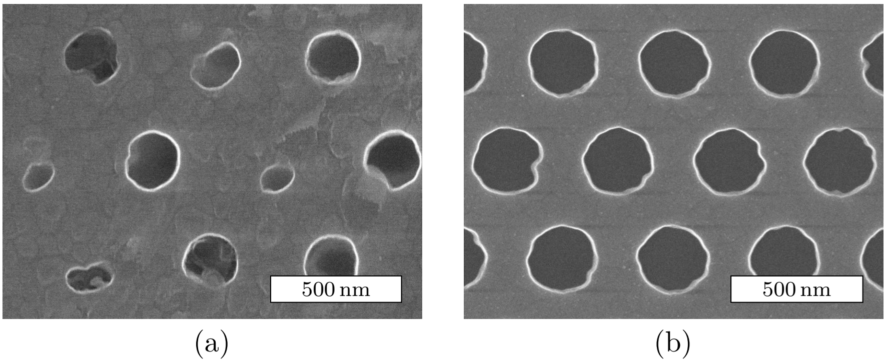

(a) (b)

Figure 5.20.: SEM images of photonic crystal hole patterns on a single sample with largely varying quality.

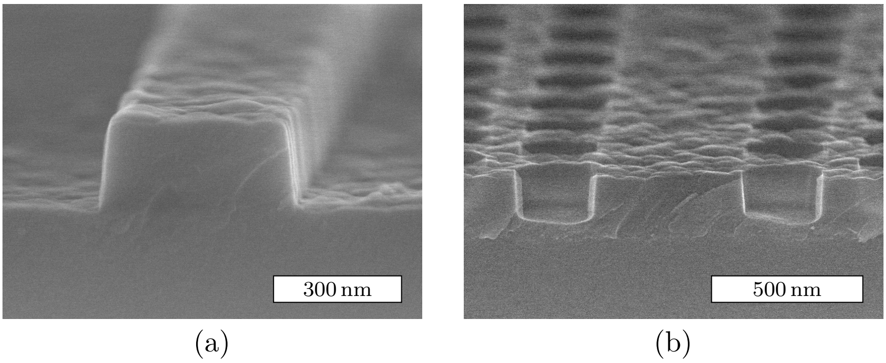

Figure 5.21.: SEM cross sections of a strip waveguide (a) and a PhC waveguide (b), showing significant surface roughness.

single process. Instead, it is assumed that a poor development process leaving resist patterns of deformed holes is the cause, and this is further investigated in Section 5.2.3.

Surface Roughness

The initial SOI samples were made by depositing both the SiO_2 cladding and the a-Si membrane with PECVD. As can be seen in the cross-section SEM images in Figure 5.21, the resulting films are notably rough compared to the features of the nanophotonic structures. Overview images revealed that the roughness appeared to originate primarily in the SiO_2 layer and were transferred to the a-Si. Surface roughness is rarely a limiting factor for device performance since it can be practically removed if e.g. using monocrystalline SOI wafers, but the roughness seen here is substantial and a real concern, and for that reason further investigated in Section 5.2.2.

It is furthermore observed in Figure 5.21 (b) that the holes are not etched all the way through the a-Si membrane, which is discussed in Section 5.2.4.

5.2.2. Thin Film Deposition

During this work, deposition of SiO_2 and a-Si was done with PECVD on a number of samples. The exact deposition rates and conditions have been found to differ between runs due to variations in chamber conditions. Particularly, the ~1 µm SiO_2 films could vary by some 10 nm. This makes it challenging to accurately hit a target film thickness, which can be important in specific device designs. However, for the purpose of developing fabrication processes it does not matter if

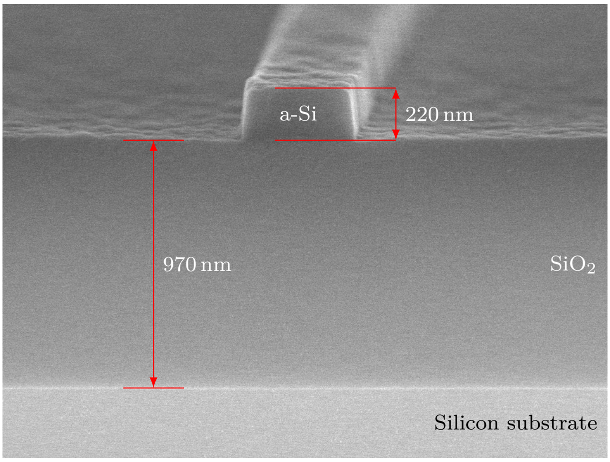

Figure 5.22.: SEM cross section of a silicon-on-insulator waveguide showing the full film stack.

thicknesses are not perfect, and the flexibility to grow films of different thicknesses has been found valuable.

Film Thickness Measurements

Figure 5.22 shows a SEM cross section of a strip a-Si waveguide on top of a SiO_2 cladding and the silicon substrate. This sample has been patterned and etched to better distinguish the two top layers, but thickness measurements of the full film stack were also made in regions that were not etched. As indicated in the figure, the SiO_2 cladding has a thickness of 970 nm, and the silicon film is 220 nm thick. Reflectometry measurements of the same film stack prior to patterning gave similar thicknesses of 987 nm and 200 nm. The discrepancy between reflectometry and SEM measurements for these types of film stacks has been previously observed in the research group, and is believed to relate to material models that do not properly match the optical properties of the thin films. Thus, reflectometer measurements are only regarded as approximate, and SEM measurements are considered more reliable.

On this particular sample, the thickness of the a-Si is as intended, but the SiO_2 came out 30 nm thinner than the 1 µm setpoint. A cladding of insufficient thickness will result in enhanced substrate leakage, but is not discussed further since it can be easily fixed by depositing for longer times. However, the introduction of additional surface roughness follows with thicker films, which means that alternative solutions discussed below are better for obtaining specific thicknesses.

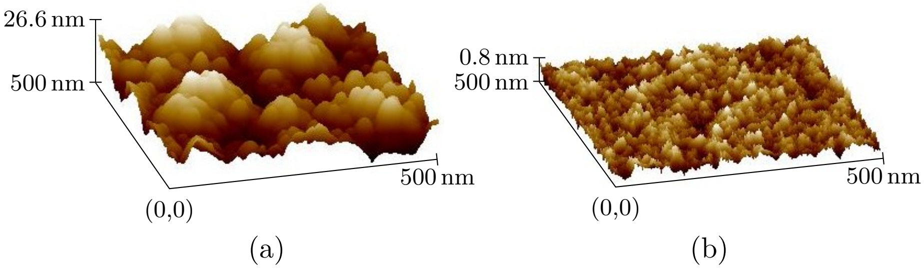

Figure 5.23.: AFM-measured topography of (a) 1 µm thick PECVD-grown SiO_2 and (b) commercial wafer with 1 µm thermally grown SiO_2.

Film Roughness Measurements

In SOI photonics research, surface roughness is rarely pointed towards as an important contributor to optical losses. Commercial monocrystalline SOI wafers are essentially atomically flat, so that surface roughness is often negligible compared to that of etched sidewalls [48]. Alternatively, chemical-mechanical polishing (CMP) can be used to reduce surface roughness of films grown with PECVD down to values around 0.5 nm, and in these cases the top surface scattering should contribute to the losses by only a few tenths of a dB/cm [45, Ch. 6]. From observing the a-Si and SiO_2 surfaces in Figure 5.21, it is however evident that the deposited PECVD films are far from ideal, thus quantification of the roughness using AFM was found necessary.

The surface topographies measured with AFM for a sample with thermal SiO_2 and one with PECVD-grown SiO_2 are shown in Figure 5.23. It is pointed out that the vertical scales for illustrative purposes are not the same in the two cases, and that the respective vertical scalebars indicate the maximum measured peak-valley difference in the scanned areas. Numerical analysis of the root mean square height fluctuations yield 0.16 nm and 5.1 nm for the thermally and PECVD-grown films, respectively. These measurements were found to be consistent when performed over scan areas of different sizes from $500\times500\,\mathrm{nm}^2$ up to $10\times10\,\mu\mathrm{m}^2$. Peak valley height differences of more than 20 nm are observed in Figure 5.23 (a), which correspond to approximately 10 % of the thickness of the silicon slab that is succeedingly deposited.

Zhu et al. [47] demonstrate propagation losses for TE modes in strip waveguides of 5 dB/cm for a PECVD-grown a-Si film having RMS roughness of 2.6 nm. In other words, the measured roughness of the SiO_2 film is higher than desirable, and measures must be taken to reduce it. The roughness of PECVD SiO_2 compared to thermal SiO_2 is of such magnitude that it is believed to explain the failure of previous attempts [8] of device light coupling in the research group. In fact, in parallel with this work, PhD student Jens Høvik was the first in our group to succeed in coupling light through a strip waveguide – after switching to substrates with thermally grown oxide.

Since CMP equipment is currently not available at the NTNU NanoLab, depositing a-Si onto thermally oxidized wafers are considered to be the best alternative to expensive commercial SOI wafers. While it is believed that CMP can be an easy and efficient method of reducing the PECVD SiO_2 roughness, results from Zhu et al. [47] indicate that this method may be less applicable for polishing the a-Si film due to introduction of absorptive surface defects. However, the silicon core is thinner than the oxide cladding by a factor ~ 5 which means that less roughness is likely to appear during deposition of this film, reducing the need for a roughness reduction in the first place.

5.2.3. Lithography Process Development

The features of photonic crystal devices designed to operate in the near IR range are rarely smaller than some 100 nm, which is not considered challenging in terms of EBL resolution. However, nanophotonic devices are sensitive to roughness-induced scattering so that the accuracy of fabricated structures should be on the order of 10 nm or less [19, Ch. 5]. This tightens the requirements of the patterning and subsequent etching, and means that well-designed processes are needed. This work is the first (in parallel with others) performed at the NTNU NanoLab with the newly installed 100 kV Elionix EBL system, and any change to a lithography process intended for fabrication of high resolution structures needs careful consideration.

As discussed in Section 3.2.3, there are several parameters available for adjustment in an electron beam lithography process. Most important in terms of obtaining well-defined patterns are the exposure dose and the strength of the development process. Their influence on resulting patterns are interrelated, where for example a slight under-exposure can be compensated by a more aggressive or longer development [75, Ch. 2]. In other words, it is the combination of all the processes which ultimately determines the final result, and there can be more than one set of combinations that give satisfactory pattern quality.

Patterns with a large number of different exposure doses and currents can be efficiently written on a single sample, whereas development optimization requires one patterned sample for each set of development parameters tested. Thus, for practical purposes, it was decided to fix the development procedure to a given process suggested by the e-beam resist manufacturer [82], and only experiment with different exposure doses and currents.

Optimum Exposure Dose

The overall goal of testing different exposure doses is to find that which is as low as possible, while still having a sufficient margin towards under-exposure. The former is desirable for reducing proximity effects, and the latter for having a process where small changes in other processing parameters do not severely influence the final result. Examples of such changes are drift in the EBL exposure current and the exact development conditions (time, temperature, strength of agitation).

To separate artifacts introduced by the lithography and etching processes, the developed resist was imaged *prior* to etching. Devices that were etched are however also shown here to further correlate the quality of etched structures to that of the lithography process. Crystalline silicon substrates were used in these experiments to remove the effect of roughness in the a-Si originating from the PECVD process.

A sample was patterned with various test-structures similar to those of the final photonic crystal devices (hole arrays, waveguides of different widths, tapers etc.). Based on initial fabrication attempts where an exposure dose of 300 µC/cm^2 was used with a fair degree of success, doses from 200 to 500 µC/cm^2 in steps of 50 µC/cm^2 were tested. Evaluation of the doses was done with optical microscopy of the developed resist, followed by SEM-imaging of the same structures to allow resolution of finer details.

Figure 5.24 shows optical micrographs of 1 µm wide strips exposed with doses of 200, 250 and 300 µC/cm^2. They were all patterned on a single sample which means they went through the very same development process. The samples with the lower two doses are clearly under-exposed as seen from the presence of resist residues. The waveguide exposed with 300 µC/cm^2 appears to be sufficiently exposed, which was the case for all the tested doses between 300 and 500 µC/cm^2. No notable over-exposure was detected even for the highest doses, however this is not as easily detectable as under-exposure. Over-exposure will lead to enhanced proximity effects which in mild forms may not be significant – at least in order to be detected with optical microscopy.

SEM images of the resist pattern used for photonic crystal incoupling waveguides can be seen in Figure 5.25. As expected from the optical microscopy analysis, the waveguide with 250 µC/cm^2 nicely illustrates significant under-exposure. The waveguide with a dose of 300 µC/cm^2 is nearly sufficiently exposed, but minor residues of resist too small to be detected in light microscopy are observed both near the waveguide edges and as dots in bulk exposed areas. Waveguides with higher doses from 350 µC/cm^2 and upwards were all observed to be sufficiently exposed and exhibited smooth edges of the resist, as seen in the example structure exposed with 400 µC/cm^2 in Figure 5.25.

The resist residues observed for the dose 300 µC/cm^2 will severely influence

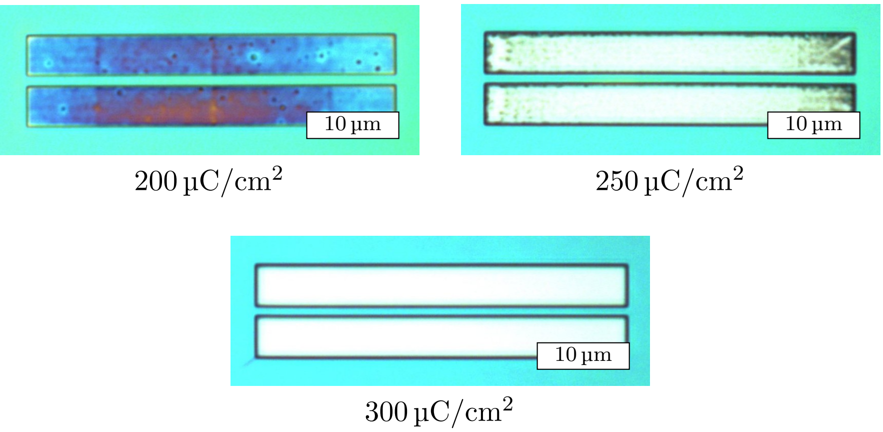

200 µC/cm^2 250 µC/cm^2

300 µC/cm^2

Figure 5.24.: Optical micrographs showing developed resist patterns of 1 µm wide strips exposed with different EBL doses. Regions without remaining resist appear white in color.

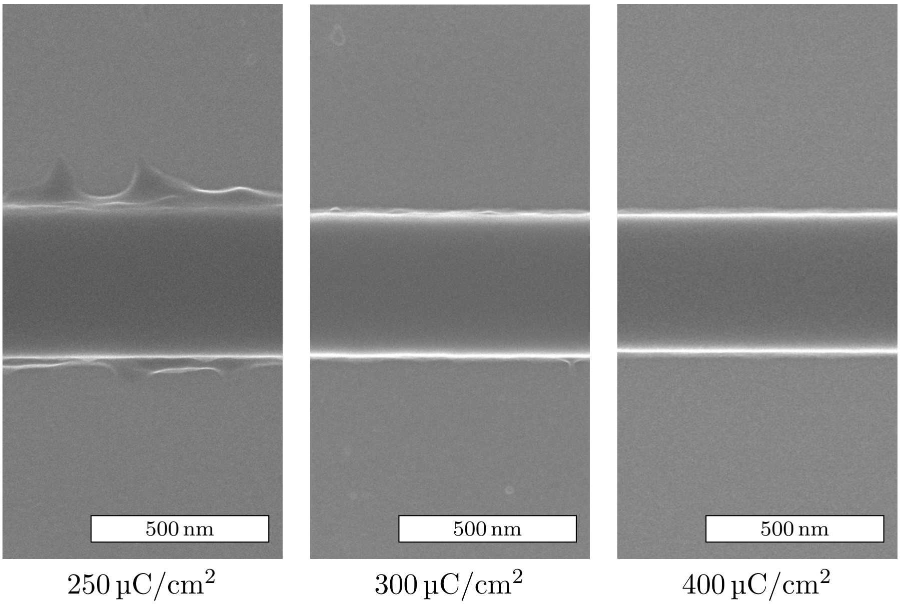

250 µC/cm^2 300 µC/cm^2 400 µC/cm^2

Figure 5.25.: SEM images of developed resist exposed with different doses, showing (from left to right) significant, moderate and no under-exposure.

the quality of etched structures by giving irregular sidewalls at edges and rough surface topography in bulk areas. The near-sufficient dose also explains results in preliminary fabrication attempts of identical structures where some were of high quality whereas others had irregular sidewalls. Since the dose is at the edge of the process window, slight differences in other parameters such as the exact value of the exposure current or the development process can result in large differences in resist pattern quality.

Figure 5.26 shows waveguides and holes that were exposed with different EBL doses and subsequently etched into silicon. The difference in sidewall regularity correlate well with that observed in Figure 5.25 when imaging the developed resist alone. Both the waveguides and holes exposed with $300\,\mu C/cm^2$ have vertical striations corresponding to lumps of resist remaining at the edge during etching, whereas the structures exposed with $400\,\mu C/cm^2$ are smoother. With these observations, it is concluded that the sidewall roughness of preliminary structures in Section 5.2.1 originates primarily from the lithography process and not from etching.

It is also seen in Figure 5.26 that higher doses yield larges holes and narrower waveguides. This is as expected from enhanced proximity effects in over-exposed structures. Specifically, hole radii for the doses 300, 400 and $500\,\mu C/cm^2$ were measured[6] to be 131, 137 and 141 nm, respectively, where the mask design specified a radius of 130 nm. It is possible to correct for such effects when designing exposure masks, but in practice the design process is more robust if the dimensions of fabricated structures match those of the design as closely as possible. In this case it is not necessary to perform feature-specific dose testing when new structural features are introduced to the design.

The conclusion from testing doses is that $300\,\mu C/cm^2$ is marginally insufficient, and that $350\,\mu C/cm^2$ and upwards is needed to remove all resist residues and leave smooth edges. For higher doses, larger areas than those specified in the designed mask are removed in the development due to over-exposure of the positive tone resist. An exposure dose of $350\,\mu C/cm^2$ is therefore chosen and used in the rest of this project, which provides a fair trade-off between tolerance towards under-exposure while avoiding excessive proximity effects from over-exposure. Different doses are however occasionally tested in later fabrication attempts to observe their influence on features such as sidewall etch profiles.

Effects of Different Exposure Currents

The effect of the exposure current on the sidewall quality of developed resist patterns was investigated by writing identical patterns with different currents. The main objective of varying the current is to observe whether the sidewall

---

[6] A programmatic analysis procedure of SEM images discussed in Appendix C is used to determine sizes of holes in this work.

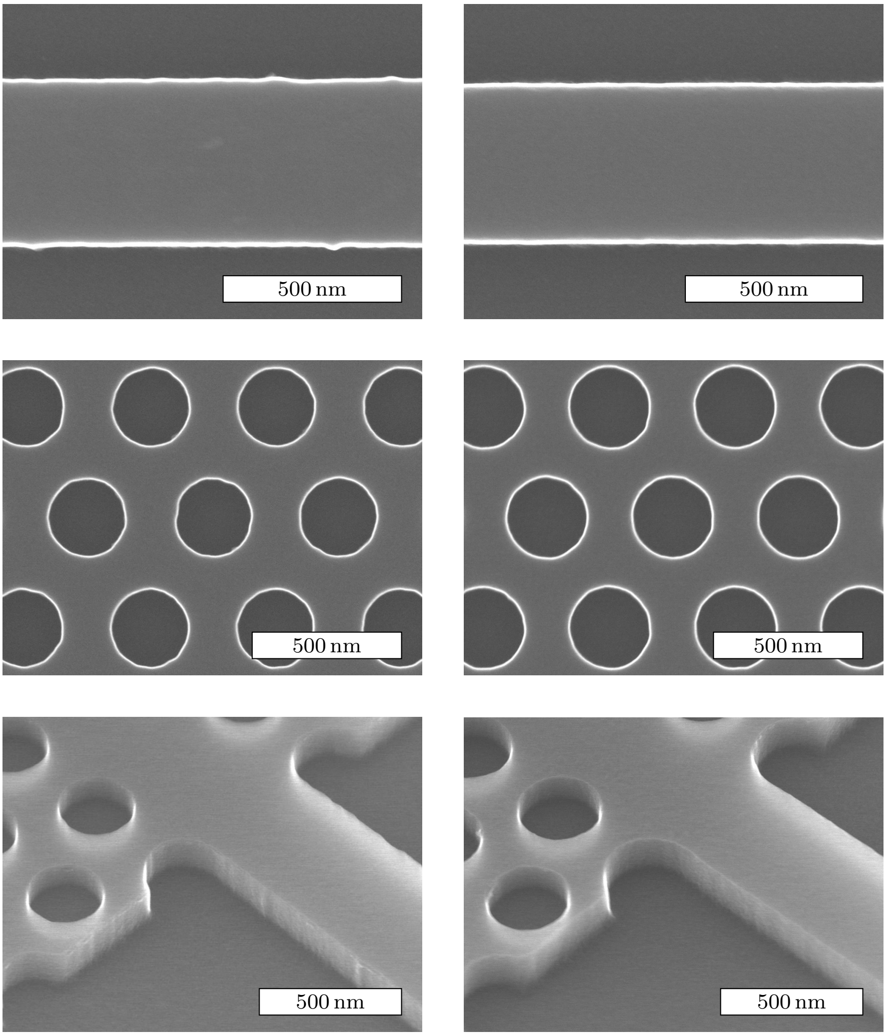

300 μC/cm^2 400 μC/cm^2

Figure 5.26.: SEM images of etched silicon patterned with different EBL exposure doses. Left column: 300 μC/cm^2, right column: 400 μC/cm^2. Note the irregular sidewall edges observed for the lower dose.

Table 5.2.: Measured RMS line edge roughnesses for the waveguides shown in Figure 5.27.

Exposure current	Edge roughness
100 pA	0.6 nm
1 nA	1.3 nm
5 nA	1.4 nm

regularity is improved by using lower currents, since this will result in a more time consuming process. As discussed in Section 3.2.3, the main contributor to the total EBL write time is often that spent on exposure, in which case it will be close to inversely proportional to the beam current. Three currents of 100 pA, 1 nA and 5 nA were tested in this project, where the extremities result in write times that differ by a factor ∼50. The exposures were done on a single sample so that the patterns were handled identically in all post-exposure fabrication steps, and an exposure dose of 350 µC/cm^2 was used as found optimal in the previous section.

The resulting developed resist patterns exposed with different currents were examined using scanning electron microscopy and can be seen in Figure 5.27. The line edge roughness of the strip exposed at 100 pA is notably lower than for the patterns exposed at 1 and 5 nA. Similar observations were made from SEM images of PhC holes which appeared slightly deformed when exposed at high currents compared to holes exposed at 100 pA. Using the image analysis method discussed in Appendix C, the RMS roughness values σ for the different exposure currents are quantified. The results are listed in Table 5.2, and support the qualitative observations in Figure 5.27. For comparison, the early fabricated waveguide structures shown in Section 5.2.1 had roughnesses of 5 nm and higher, where the exposure current was set to 5 nA.

Since sidewall scattering losses vary quadratically with σ [105], even small differences can be significant. For example, results from Sparacin et al. [69] show that the losses associated with sidewall roughness in 630×220 nm^2 silicon strip waveguides varied between 9.2 and 1.9 dB/cm for RMS roughnesses of 1.4 and 0.7 nm, respectively. Comparing these values to the results in Table 5.2, it is concluded that the use of the lowest exposure current is worthwhile, even though it causes longer write times. It is noted that the line roughnesses were determined from top-view SEM images of resist patterns, and that additional roughness is expected to be induced on the sidewalls during subsequent etching. Thus, the values in Table 5.2 form a lower limit for the final σ of the silicon sidewalls.

A workaround for the long write times that follows when exposing at 100 pA, is to expose different areas of a sample with different currents. Critical regions such

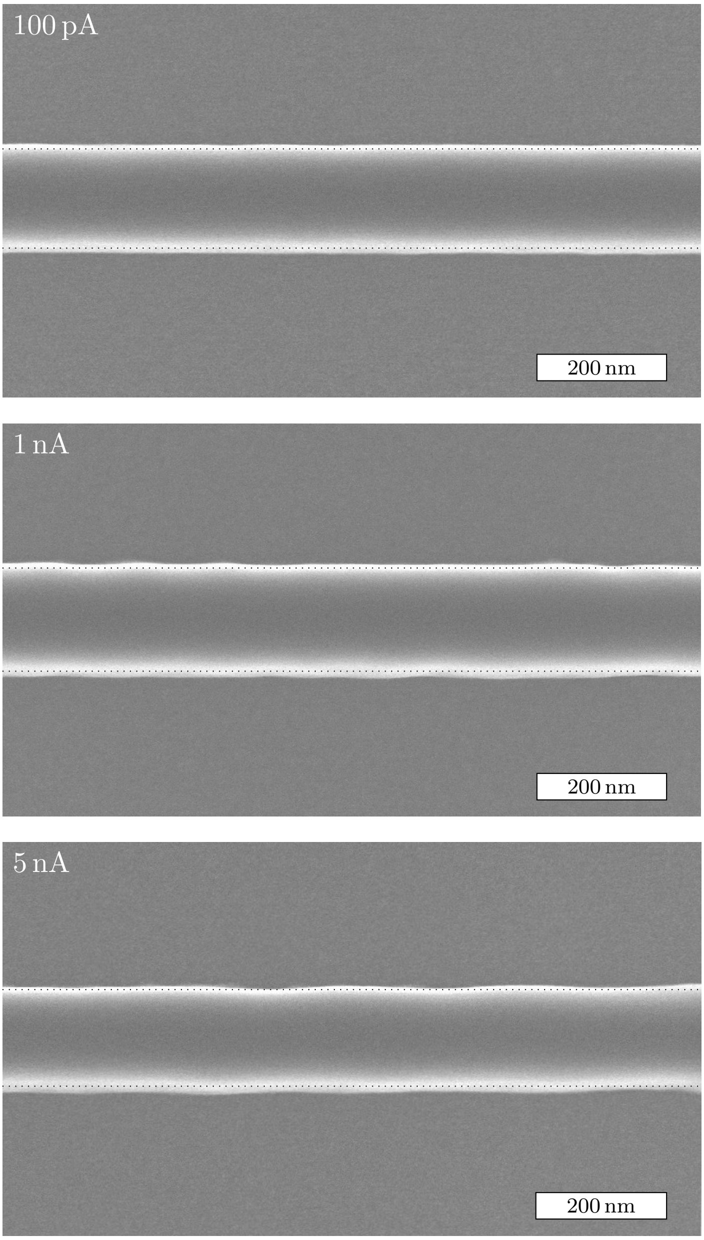

Figure 5.27.: SEM images of identical resist patterns written with different EBL exposure currents as labeled in the images. The dotted lines are added as guides to the eye for improved visualization of the line edge roughness.

as photonic crystal holes and the region right next to the waveguide sidewalls can be exposed with low currents, while bulk areas without important features are exposed at higher currents. This was done for some of the devices fabricated in this project, for which bulk areas were exposed at 5 nA. An additional waiting step of ∼30 min is however required after changing the beam current, since the beam needs to stabilize at the new current before proceeding with exposure. This means that the method is useful only for exposures where this addition in write time is small compared to the total.

An in-depth investigation of the causes of the correlation between σ and the exposure current is not performed, but a number of effects can partially explain the findings, both physical effects and instrumental errors. As mentioned in Section 3.3.1, sample charging is a key contributor for limiting the resolution of scanning electron microscopes due to the build-up of electrostatic fields. Although charging will indeed increase with the beam current, it is not assumed to be the primary cause of the increased line roughness since the patterns were written on a non-insulating substrate (lightly p-doped c-Si). Instrumental effects such as blanking errors are also assumed to be increasingly important at high currents, and can contribute to the less accurate pattern transfer that is observed.

Improving the Development Process

As seen in Figure 5.20, the first fabricated structures have a large variation in quality of the patterns that were transferred to the silicon during etching. Even on a single sample, some regions could have a fairly successful pattern transfer (if neglecting sidewall irregularities), while others showed highly deformed holes not even resembling the design specified in the exposure mask. The local variations are assumed to be caused by neither poor exposure nor the etch process, but rather by the development process since the first samples were immersion developed without any agitation. A stagnant developer is believed to have given varying development rates in different regions depending on the amount of chemical that is locally consumed. Agitation during development was suggested as a way to circumvent this by continuously bringing fresh developer to the sample surface.

Two types of agitation during immersion development were attempted. The first was ultrasonic agitation, which is a documented technique for improving development uniformity [106]. The second method was a gentle manual agitation (stirring) of the holder used to carry the sample during immersion.

Although having the advantage of avoiding human influence on the strength of agitation, ultrasonic agitation during development was found to be too violent for achieving the desired resist patterns. Figure 5.28 illustrates this by showing a developed resist strip intended for making a waveguide, which is broken at several places. Slight manual agitation was on the other hand found to be gentle enough to not destroy the resist patterns, while still yielding uniform results across entire

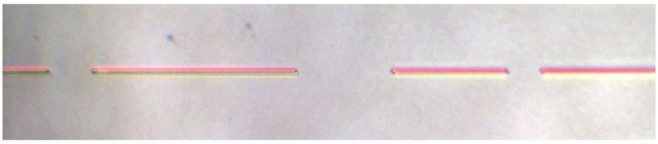

Figure 5.28.: Optical micrograph of a 500 nm wide strip of e-beam resist broken at several places due to excessive ultrasonic agitation during development.

samples. For that reason, manual agitation during development is used for all the samples succeedingly fabricated.

5.2.4. Silicon Etching

As discussed in Section 2.6, the etch process is a crucial step in photonic crystal fabrication – especially for high index contrast material systems such as SOI where sidewall roughness in many cases is the dominant optical loss mechanism [69]. The etch recipe used in this project is chosen to be one that has previously been found to be anisotropic and giving reasonably straight sidewalls with low roughness [6, 8]. The results from any etch process depends however largely on the preceding lithography step and corresponding resist patterns. A new EBL system and a different e-beam resist is used in this project, which calls for a thorough etch characterization in context of the new lithography process.

All of the structures presented and compared in this section were patterned and etched on the same crystalline silicon sample using a 40 s ICP-RIE process as described in Section 4.2.3.

Etch Rate and Selectivity

It is difficult to accurately determine ICP-RIE etch rates *a priori*, and they must generally be found using either real-time interferometric measurements or post-process methods such as profilometer scanning, AFM measurements or SEM cross-section imaging. The latter is used in this project due to the high resolution possible as well as the information revealed about etch profiles and qualitative sidewall roughness.

Figure 5.29 shows cross-sections of a waveguide and PhC holes revealed from cleaving in the Γ-M direction of the hexagonal lattice. The etch depths for the waveguide and holes are measured to be 243 nm and 164 nm, respectively, corresponding to etch rates of 365 nm/min and 246 nm/min. This rate difference is caused by *microloading* which is discussed in Section 3.2.4. The difference in pattern density and aspect ratio for the waveguide and PhC holes results in this case in a 33 % etch rate reduction if using the waveguide as reference. It is

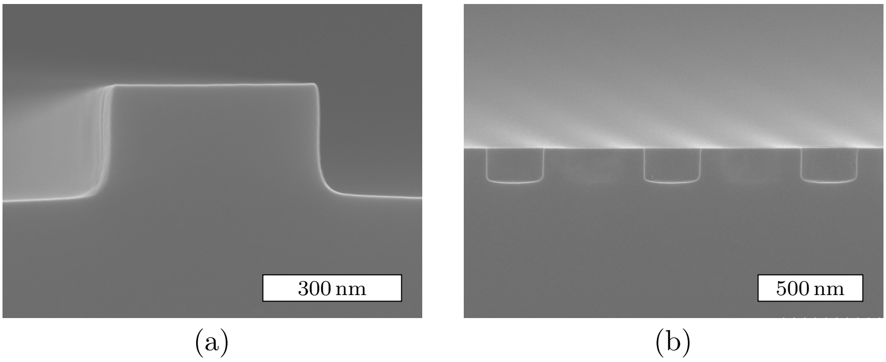

(a) (b)

Figure 5.29.: Cross-section SEM images of etched silicon structures: (a) waveguide and (b) photonic crystal holes.

furthermore expected that the rate difference will vary during an etch process by continuously increasing as the holes become deeper. This trend was confirmed by etching an identically patterned structure for a shorter time (30 s), which resulted in a measured PhC-hole etch rate reduction of 25 % as compared to the waveguides.

The different etch rates for holes and waveguides introduces a problem where the waveguides are etched for longer than necessary during the time needed to etch the holes deep enough. This can lead to excessive sidewall roughness due to chemical etching of the sidewalls, and thus cause larger propagation losses. Also, an undesirable effect called *notching* can occur, which consists of excessive etching of the silicon at the corner of the SiO_2-silicon interface [107].

One possible workaround for these problems is to etch the waveguides and holes in two separate processes. However, this is not desirable since it introduces an additional time-consuming lithography step, as well as opens up for alignment errors when overlaying the second lithography pattern. A simpler solution, which is used in this work, is to rely on the SiO_2 cladding to work as an etch stopping layer. This procedure does not account for the problem of excessive waveguide sidewall etching, but ensures that the etch depth of the two types of features are the same, assuming that the etch selectivity towards silicon is sufficient.

The etch rates (without microloading effects) of SiO_2 and the e-beam resist were measured in a separate run with the same recipe to be 71 nm/min and 153 nm/min, respectively. Reflectometry thickness measurements before and after a 40 s etch were used to determine these, and the resulting etch selectivity of silicon is found to be 5.1:1 towards the SiO_2 and 2.4:1 towards the resist.

The fair resist selectivity makes it possible to use thinner etch masks than those used in this project (∼500 nm). For high resolution pattern transfer, it is generally advantageous to use etch masks that – within reasonable margins – are as thin as possible. It is however believed that only minor or no improvements in line edge roughness is achievable for the structures fabricated in this work, since the pattern quality from the lithography process is already satisfactory. Furthermore, the high EBL acceleration voltage of 100 kV provides deep interaction volumes with straight sidewalls in the resist layer, making its thickness a less sensitive parameter in the patterning process. On the other hand, it is likely that thinner resists reduce the effect of microloading from lowering the aspect ratios during etching, and may also avoid collapse of resist patterns with higher aspect ratios than those fabricated thus far.

Etch Profile

The waveguide and PhC holes in Figure 5.29 are observed to be anisotropically etched, as is the intention for etching photonic structures with vertical sidewalls. Specifically, the sidewall angles for both structures are measured to deviate less than 1° to 2° from vertical, where the measurement uncertainty originates from the presence of slightly round edges.

The effects of tapered sidewalls on device performance have been investigated both numerically and experimentally. Simulations by Tanaka et al. [50] of the effect of tapered sidewalls of PhC air holes on propagation losses show that a taper angle as low as 1° can introduce losses up to 5 dB/cm at certain frequencies. They conclude that the vertical asymmetry introduces polarization mixing and thus power loss when the guided TE-like modes couple to in-plane extended TM-like modes. It is noted that only suspended membrane PhC waveguides were considered in this study, and that the vertical symmetry breaking from introducing a bottom SiO_2 cladding introduces much higher propagation losses than that expected from a small angle tapered sidewall. For example in the simulations of SOI PhC waveguide in Figure 5.10, the minimum propagation loss was found to be 59 dB/mm which makes the tapered sidewall contribution negligible. Furthermore, experimental results by Selvaraja et al. [70] show TE propagation losses in SOI photonic wires as low as 2.7 dB/cm even for sidewall angles of 8°. They point out that by using a passivation layer which results in tapered profiles, the sidewalls can be protected from ion bombardment, thus reducing the sidewall roughness.

In conclusion, the etch profiles observed in Figure 5.29 are considered to be of high quality, and they are not assumed to introduce significant propagation losses compared to other loss mechanisms such as scattering from sidewall roughness.

Since the lithography process and resulting resist patterns can influence the etch process, waveguides patterned with different exposure doses were investigated to observe the effect on the etch profiles. Figure 5.30 shows cross-sections of waveguides exposed with doses of 300, 400 and 500 µC/cm^2, to the same scale

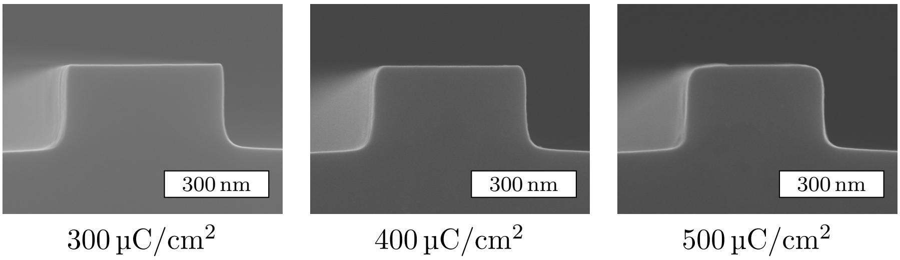

Figure 5.30.: Cross-section SEM images of etched silicon waveguides patterned with different exposure doses during electron beam lithography.

for comparison purposes. First of all, as noted in Section 5.2.3, the widths of these identically designed waveguides decrease for higher doses due to proximity effects that cause removal of more resist than intended. The respective widths are measured to be 448, 434 and 395 nm.

The cross-section views in Section 5.2.3 also show that the top corner of the waveguides become increasingly rounded for high doses. The reason for this is assumed to be an increased undercut in the resist profile for high exposure doses. An illustration is seen for the positive resist pattern affected by proximity effects in Figure 3.3[7]. The undercut can result in rounded waveguide edges from one of the two suggested mechanisms, or a combination of both: (i) the undercut resist profile protects against physical etching, but chemical etching occurs below the undercut profile, or (ii) the sharp edges of the undercut profile are gradually removed during an etch process, exposing increasingly more of the waveguide to both physical and chemical etching.

Although not attempted, it is believed that by reducing the development time, resist profiles without undercut could be achieved for higher exposure doses and thus less edge rounding. The validity of the suggested mechanisms for edge rounding are not investigated further, but it is concluded that lower exposure doses yield features of favorable characteristics in terms of having both appropriate widths and sharply defined etch profiles.

Sidewall Roughness

Direct measurements of waveguide sidewall roughness is experimentally difficult [45]. The AFM is the workhorse tool for nanoscale topographic mapping, but the large step heights and near vertical waveguide profiles make such measure-

---

[7] Note that Figure 3.3 illustrates an inverted exposure pattern compared to that needed to form waveguides with a positive resist etch mask. A more appropriate illustration is that in Figure 3.4 (c), although this figure illustrates effects of varying development times.

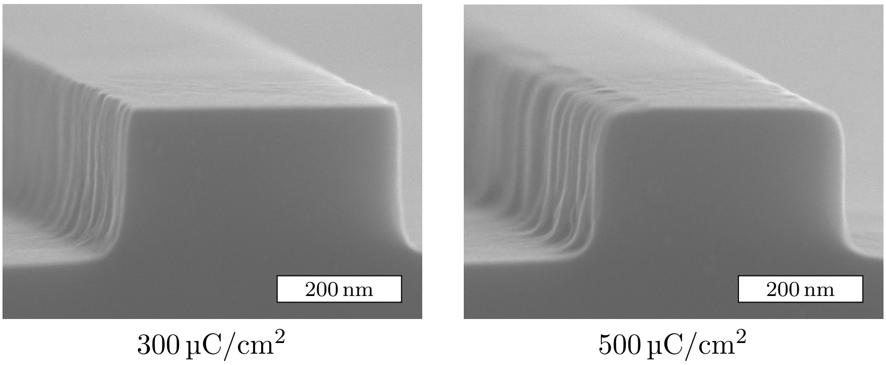

$300\,\mu\text{C/cm}^2$ $500\,\mu\text{C/cm}^2$

Figure 5.31.: Cross-section SEM image showing the sidewalls of etched crystalline silicon waveguides patterned with different EBL doses.

ments useless unless using technically challenging procedures such as cleaving the wafer right next to the waveguide and mounting the sample with the waveguide sidewall facing the AFM probe [108]. In lack of direct-measurement methods, qualitative SEM analysis and optical loss measurements are commonly used to estimate sidewall roughness [45, 48]. It is possible to use top-view SEM images to quantitatively determine sidewall RMS roughness and roughness correlation length [109], as elaborated in Appendix C. However, this is limited to cases where the top-view images reveal significant sidewall edge roughness, which is not the case for the structures etched in this project such as that shown in the top right image of Figure 5.26. Generally, waveguides appeared smoother in top-view SEM images than they did in tilted views, so the following discussion considers only qualitative appearance.

High resolution SEM images in Figure 5.31 show sidewalls of etched waveguides patterned with exposure doses of 300 and $500\,\mu\text{C/cm}^2$. It is pointed out that the images were captured after a 30 s O_2-plasma ashing, since initially imaged waveguides showed signs of remaining passivation polymers or resist residues. No additional roughness was observed to be introduced by the plasma ashing. The sample was mounted slightly tilted in order to better reveal the sidewall roughness during imaging. Whereas the sidewall of the $300\,\mu\text{C/cm}^2$ waveguide appears reasonably smooth except for light vertical striations, the sidewall of the $500\,\mu\text{C/cm}^2$ waveguide is notably rougher. Although not shown here, waveguides exposed with doses of $400\,\mu\text{C/cm}^2$ resulted in a somewhat intermediate sidewall roughness compared to the two shown in Figure 5.31.

The dose-dependent roughness is assumed to relate to the smoothness of the resist mask as well as the type of resist profile obtained from the lithography process. The higher dose is as discussed in the previous section expected to yield an undercut resist profile, allowing etching action to occur underneath the overhanging edges. The effect of this is observed as indentations at the top waveguide surface in regions that ideally should be covered by the etch mask. Furthermore, only small thickness fluctuations in the overhanging resist layer will cause deep vertical striations in the etched profile, since the etch breaks through the mask locally at different times. A resist mask with a vertical profile is less sensitive towards small fluctuations in thickness, and the amount of resist line edge roughness (LER) remaining from the lithography process is in that case expected to be the dominant mechanism for transferring roughness to the silicon sidewalls during etching.

Also evident from Figure 5.31 is that the roughness of the waveguide sidewalls is much larger than that of the top surface. In this case where the waveguides were made on a c-Si substrate, this is not surprising, but it nevertheless motivates why sidewall roughness usually is the dominant optical loss mechanism in strip waveguides [48, 49] – particularly for TE-modes which have high modal power at the sidewalls.

The sidewall roughness obtained for low exposure doses as seen in Figure 5.31 is concluded to be sufficiently small at this stage in fabrication. For later studies, three main routes for reducing roughness are nevertheless listed, and briefly discussed below:

1. Reduction of resist pattern line edge roughness remaining from lithography.
2. Test different ICP-RIE etch recipes and possibly -chemistries.
3. Include a post-etch sidewall smoothing process.

The development processes can result in the formation of *scum*, which is the term for remaining resist at the etch mask edges [49, Ch. 4]. It forms because the bulk resist is dissolved faster than resist at the substrate/resist-interface, and is inherently irregular. The irregularity of the scum is transferred to the silicon during etching in form of vertical striations. By including so-called descumming steps, the scum is removed and the resist LER can be reduced. Example descumming techniques are plasma etching or thermal reflow procedures [49].

The etch recipe itself has a vast number of parameters that can be tuned to yield features of low sidewalls roughness, too many for a thorough consideration to be made in this project. Among the parameters are the etch chemistry itself, the relative power of the ICP and CCP generators for tuning between physical and chemical etching, gas flows, pressure, temperature etc. Also, the use of hard masks during etching has been found to reduce LER since they are more resistant to degradation from reactive ion species during the etch step [49]. However, any benefits from using a hard mask come at the expense of introducing additional processing steps.

Finally, methods have been demonstrated for post-etch smoothing of waveguide sidewalls and thereby reducing optical scattering losses. For example, wet chemical oxidation has been shown to reduce the sidewall roughness amplitude without significantly changing the waveguide structural dimensions, causing in one study a change in sidewall losses from 9.2 to 1.9 dB/cm [69]. Such techniques do not necessarily complicate the overall fabrication considerably, and are thus relevant to investigate during future attempts of optimizing device performance.

5.2.5. Polymer Waveguides for Inverted Taper Coupling

Due to the large modal mismatch between lensed fibers and silicon strip waveguides, fabrication of polymer waveguides for inverted taper coupling as introduced in Section 2.7 is attempted. The epoxy-based resist SU-8 is chosen as the polymer material due to its mechanical properties and successful results from others [92, 55]. Since SU-8 is originally a photoresist, there are not as many available technical reports discussing SU-8 patterning with EBL. A few do exist [94, 93], but the main goal of this section is to find appropriate doses and development processes for making $2{\times}2\,\mu\text{m}^2$ strips of SU-8 overlaid on silicon inverted tapers.

Dose Testing

A wide range of 30 doses between 0.5 and $29.5\,\mu\text{C/cm}^2$ were used for the dose testing based on several reports [93, 94, 95], with a fixed development process of 60 s immersion development as suggested in the datasheet [92]. Figure 5.32 shows SEM top views and cross sections of polymer strips exposed with different doses. Firstly, it is observed that all the strips are thinner than the 2 µm which was measured with reflectometry after spin coating. This was later found to be partly caused by the resist evaporating during SEM-imaging, and is further discussed below. There is however also a trend of the low-dose strips being thinner, which is expected for a negative resist. When the dose is too low for sufficient cross-linking, the strip is thinned down during development.

Secondly, the resist profiles appear similar to the schematic presented in Figure 3.4. The highest dose shows side lobes characteristic for over-exposed negative resists caused by back-scattered electrons, and the lowest dose shows an undercut resist profile from a combination of insufficient cross-linking and over-development. Although the center dose resulted in a waveguide with more vertical sidewalls, it shows signs of over-development from the undercut sidewalls. These observations lead to the conclusion that the fixed development time of 60 s was too long to be compensated by an appropriate choice of dose, and that it was necessary to test doses in combination with different development times.

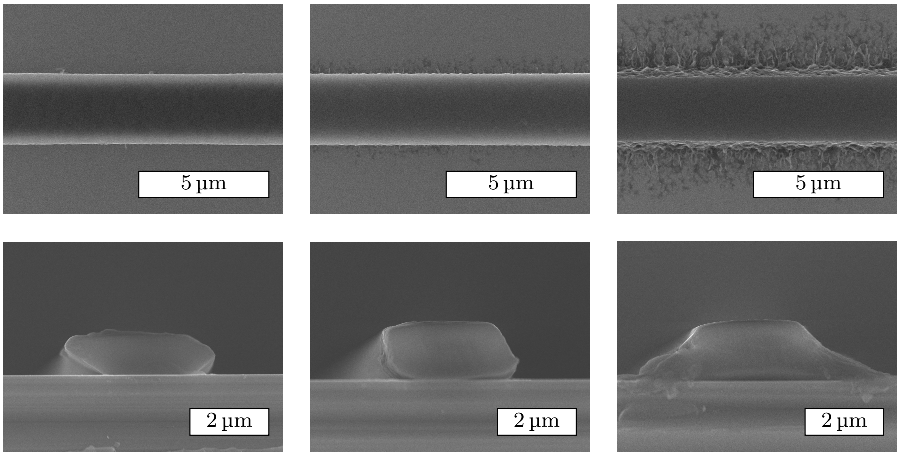

$3.5\,\mu C/cm^2$ $12.5\,\mu C/cm^2$ $29.5\,\mu C/cm^2$

Figure 5.32.: SEM images showing top and cross-section views of SU-8 polymer waveguides exposed with different doses.

Development Testing

After performing the same dose tests as above for patterns that were immersion developed for 30, 45 and 60 s, it was found that 45 s development in combination with doses of approximately $10\,\mu C/cm^2$ resulted in waveguides with superior characteristics to those in Figure 5.32. This dose is lower than the $19.9\,\mu C/cm^2$ suggested by Bilenberg et al. [93] for 100 keV EBL exposure of SU-8 resist, but they investigated much finer resist lines of few tens of nm where the requirement of larger doses is expected.

SEM images of the optimized structures are shown in Figure 5.33. The tilted cross section view in (a) shows that the resist sidewalls are nearly vertical and of fair quality, but the thickness decreases towards the cleaved edge. This was found to be caused by material evaporation when recording the high-resolution cross-section SEM image shown in Figure 5.33 (b), and the evaporation also explains the non-rectangular appearance of this cleaved waveguide edge. Despite attempts of imaging at low currents and acceleration voltages, the evaporation could not be avoided. However, devices used for optical coupling do not need to be examined with SEM prior to use, in which case this problem is non-existent.

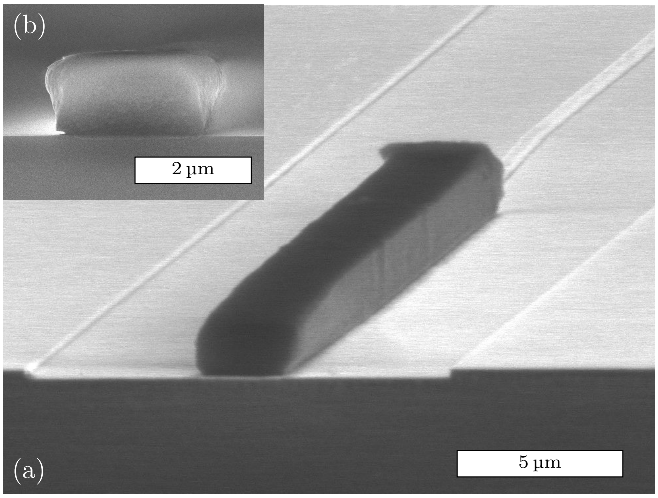

Figure 5.33.: SEM image showing (a) a tilted view of an SU-8 strip waveguide overlaid on a silicon inverted taper and (b) a cross section view of the same waveguide.

Spin Coating

The sample preparation procedure suggested in Section 4.2.4 for spin coating SU-8 onto silicon substrates is rather rigorous, but was developed after a number of preliminary tests yielding highly varying film qualities. Non-reproducible results were obtained when using identical cleaning procedures, ranging from perfectly uniform thin films to no adhesion at all.

The inconsistencies are believed to relate to the surface chemistry of individual samples, notably in terms of organic residues and and remaining moisture. Some samples had previously been coated (and stripped) with e-beam resist and cleaned with DI water. In addition to rinsing with various solvents, two steps were added to remove the influence of differing sample histories: A baking step and an O_2-plasma treatment. The baking step dehydrates the surface, while the plasma treatment removes organic residues. The O_2-plasma treatment was included as the final cleaning step and performed directly before spin coating. High quality SU-8 thin films were consistently spin-coated throughout this project after following the cleaning process described in Section 4.2.4.

Figure 5.34 shows a film that was successfully spin coated. It is observed that a significant part of the sample is covered by edge-beads of non-uniform thickness. This particular $14{\times}14\,\mathrm{mm}^2$ silicon sample has a useful region of approximately $1{\times}1\,\mathrm{cm}^2$ in the center where the thin film is uniform, in this case with a thickness of

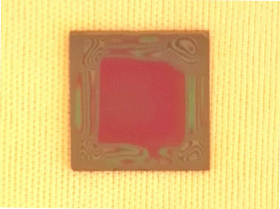

Figure 5.34.: Silicon 14×14 mm^2 sample spin-coated with a 2 µm film of SU-8 photoresist.

2.038 µm as measured with reflectometry. A larger usable sample area is desirable – particularly when using expensive substrates such as commercial SOI-wafers. The large edge-beads are believed to appear since the 2 µm thickness lies at the edge of the thickness range for which the resist is designed. At high spin speeds such as 4000 RPM, no significant edge-beads were obtained, however with a resulting film thickness of 1 µm. Although not attempted in this project, it is possible to make custom blends of SU-8 with desired viscosities and aim for one that gives 2 µm films at spin speeds between e.g. 3000 and 6000 RPM.

Pattern Overlay

Equally important as fabricating isolated high quality polymer waveguides is that of accurately positioning them on top of previously defined inverted taper silicon waveguides. By defining two registration marks during the first lithography step, these are used as reference for aligning the second layer. The registration marks are patterned and etched into silicon in the same process as that used for making the silicon photonic structures, meaning that no additional fabrication steps are introduced for the first lithography process.

Initial attempts of exposing the second layer failed since the registration marks could not be found during alignment. The reason is that even though the acceleration voltage of 100 kV provides deep beam penetration due to the large interaction volume, the resist thickness of 2 µm is too thick for the underlying etched silicon mark to be observed. A workaround was developed where, after spin coating and soft baking the SU-8 resist, a swab soaked with acetone is used to gently remove the resist layer at the corners of the sample where the marks are positioned. For best alignment, registration marks should ideally be situated as close to the exposed pattern as possible. However, the manual method of removing resist means that at least a few millimeters of clearance should be included. Nevertheless, practically perfect alignment was routinely obtained using the described procedure, where an example is shown in Figure 5.35.

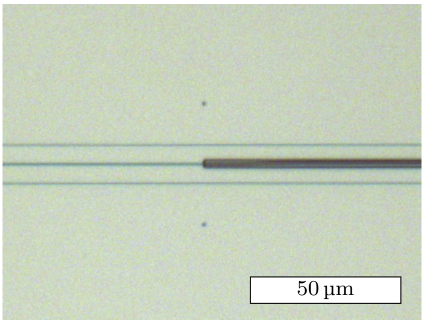

Figure 5.35.: Optical micrograph of a 2 µm polymer waveguide overlaid on an inverted taper silicon waveguide with an initial width of 450 nm. The dots serve no purpose besides being distance references.

Substrate Adhesion

Although the process development discussed above resulted in successful and reproducible fabrication of polymer waveguides of inverted taper coupling, problems of strip delamination were frequently encountered in subsequent processing steps. Particularly during sample cleaving and ultrasonic cleaning, the strips were found to both break and delaminate. Figure 5.36 shows an example of a partly delaminated polymer strip. The polymer is seen to curl into a loop, which besides being a spectacular view indicates the presence of stresses in the polymer film obtained during fabrication.

Care was taken as recommended in the datasheet [92] to reduce thermal stresses by using gradual temperature changes during baking steps, but remaining stresses are believed to contribute to the delamination observed. For future work, it is suggested to investigate adhesion promoters in combination with alternative baking steps in order to prevent delamination.

5.2.6. Fabrication Summary

A brief summary of the important findings from the various fabrication processes discussed above is given here.

The thin film deposition of SiO_2 and amorphous silicon (a-Si) was found to introduce undesirable amounts of surface roughness, which most likely explains previous unsuccessful attempts of light coupling in the research group. An RMS roughness of more than 5 nm in the 1 µm SiO_2 film was found, which was transferred to the subsequently deposited 220 nm a-Si. Methods to reduce the roughness have been discussed, and the simplest solution of depositing a-Si onto

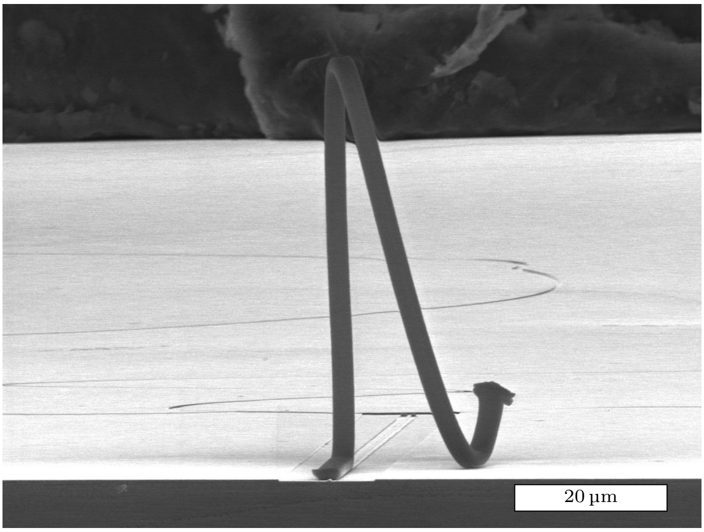

Figure 5.36.: SEM image of a partly delaminated SU-8 waveguide.

substrates with thermally grown SiO_2 was chosen. Alternative techniques such as chemical mechanical polishing or using (costly) commercial monocrystalline SOI wafers can be relevant for future fabrication of high-performance devices, since the loss contribution from surface roughness in such devices can be made negligible compared to other types of losses [48].

Several of the problems observed for early fabricated devices were found to originate from a poor lithography process. Most importantly, the effect of only a slight underexposure has been demonstrated to deteriorate the sidewall smoothness by leaving resist residues at the pattern edges. These irregularities were transferred to the silicon structures during etching, and were found to yield line edge roughnesses (LER) above 5 nm RMS, for which TE-mode propagation losses in strip waveguides are expected to be unacceptable due to the high modal power at the sidewalls [48]. Higher doses were seen to cause proximity effects e.g. in form of increased hole sizes, but can in mild forms be corrected for in software. Thus, for obtaining a robust EBL process, the optimum exposure dose of 350 $\mu C/cm^2$ was determined as one that was as low as possible while still having a significant tolerance towards underexposure. After using this dose, resist strips with LER of 0.6 nm RMS were obtained, which is comparable or better to other reports of photonic wire line roughness [109, 69]. Also the effects of different exposure currents were investigated, and it was found that low exposure currents (100 pA) yielded structures of reduced roughness compared to higher currents ($\geq$1 nA), at the expense of increasing the total write time.

The ICP-RIE process used for silicon etching resulted without modifications in etch profiles deviating less than 1° to 2° from vertical, which is desirable since tapered sidewalls gives rise to polarization mixing. The sidewall roughness could not be quantified directly, since the top-view SEM image analysis method described in Appendix C gave results of less than 1 nm RMS which from tilted SEM views of the same sidewalls appeared as underestimates. However, the qualitative appearance of the sidewalls indicates that the roughness is by no means unmanageable, which means that the etch process used can serve as a good starting point for further process optimization. Different methods for reducing the sidewall roughness have been suggested, which can be relevant for future studies.

An EBL process was developed for fabrication of SU-8 polymer waveguides for use in inverted taper spot-size converters. The dose and development time was adjusted to yield approximately $2 \times 2\,\mu\text{m}$ strips with near vertical sidewalls that were successfully overlaid on previously etched inverted silicon tapers. The polymer waveguides were found to delaminate easily during subsequent fabrication steps of sample cleaving and ultrasonic cleaning, likely due to inadequate substrate adhesion and remaining stresses of the SU-8 resist layer.

Some key aspects of the device quality could only partially or could not be probed without actual optical characterization of devices. Specifically, material absorption for different deposition recipes should be measured when using hydrogenated a-Si (a-Si:H) deposited with PECVD, since bulk defect state absorption can be a dominating loss mechanism in structures of amorphous or poly-crystalline material systems [109, 47, 74]. Also, sidewall roughness being the largest contributor to scattering losses for TE-modes in strip waveguides [49, Ch. 4] should be quantified for different etch processes by correlating strip waveguide loss characteristics to theoretical models for more accurate determination than that achievable by SEM-inspection.

Chapter 6.

Conclusion

The overall goals of this work have been to design and simulate a photonic crystal (PhC) interferometer for use as a biosensor, as well as development and optimization of fabrication processes to realize high-quality silicon nanophotonic devices.

Simulations

The computer simulations in this work have consisted of eigenmode computations of guided modes in photonic crystal structures, and complementary finite-difference time-domain (FDTD)-simulations of transmission properties of finite-sized devices. Both full 3D simulations and 2D effective index approximations have been done, generally with a high degree of correspondence which has demonstrated the usefulness of the much less computationally intensive latter alternative.

An integrated hole-slab photonic crystal Mach-Zehnder interferometer (MZI) has been designed, and optimized for high transmission at frequencies where the fundamental guided waveguide mode lies below the light line. The structural components constituting the MZI (waveguides, 60° bends and Y-splitters) have been investigated and optimized separately.

Single missing row (W1) waveguides were simulated for both 2D structures, 3D air-bridge slabs and 3D silicon-on-insulator slabs. FDTD cut-back-simulated propagation losses for the different structures were found that were successfully related to loss mechanisms understood from theory (cladding losses, polarization mixing) and correlated with band diagrams of corresponding guided eigenmodes. Lossless propagation of 90 nm bandwidth was demonstrated for TE-like modes in the air-bridge PhC, whereas the vertically asymmetric SOI slab showed losses for all frequencies due to coupling to TM-like modes. Local structural optimization of 60° bends and Y-splitters has been done, with the goal of suppressing higher order mode excitation by reducing the optical volume in the junctions. The transmission properties of both components were considerably improved compared to unoptimized implementations. When combined to form Mach-Zehnder interferometers, the optimized components resulted in high and broadband transmission through the complete device in both 2D and 3D simulations, with 3 dB bandwidths of 99 nm and 53 nm, respectively.

By adding a dielectric layer to the hole sidewalls of the MZI sensing arm, specific binding of biomolecules was modeled. Distinct dips in the transmission spectra were obtained, which were caused by excitation of high-Q ring-resonances in the MZI. This drastic change in transmission properties of balanced MZIs and MZIs with biolayers constitutes a promising transduction method for label-free biosensing. Suggestions for methods of enhancing the sensitivity to the addition of biolayers as well as challenges in experimentally realizing sensors based on the suggested design have been discussed.

The understanding of eigenmode band structures has been found useful in this project for interpreting features in FDTD-simulated transmission spectra such as the frequency-onset of high transmission and coupling between modes in bends and splitters. Thus, the use of eigenmode computations with complementary FDTD simulations has been demonstrated to be a powerful combination for studying properties of photonic crystal devices. Since waveguides, bends and power splitters are fundamental building blocks found in most PhC optical circuits, the simulations and optimized components of this work can easily be transferred to other devices than the MZI considered here.

Fabrication

This part of the work consisted of characterization and systematic optimization of individual processes in fabrication of silicon-on-insulator (SOI) nanophotonic devices, with the goal of reproducibly achieving structures of low roughness and vertically etched sidewalls. The main processes used for fabrication were thin film deposition using PECVD, lithographic pattering with EBL and plasma etching with ICP-RIE.

Thin film deposition of SiO_2 resulted in surfaces with RMS roughness above 5 nm, which lead to the decision of using thermally grown SiO_2 wafers instead of growing the oxide in-house. The lithographic patterning has been found to be a crucial step in the fabrication process, where carefully optimized process parameters are needed in order to consistently obtain resist patterns of satisfactory quality. Initially fabricated structures had waveguides with RMS sidewall roughnesses of ∼5 nm, which was improved to 0.6 nm after adjusting the exposure dose and current to optimal values of $350\,\mu C/cm^2$ and 100 pA, respectively. The plasma etch process was found to give vertical sidewalls with angles from 1° to 2°, however with aspect-ratio dependent etch rates which meant that PhC holes etched slower than low pattern-density waveguides. An EBL process for making SU-8 polymer waveguides has also been developed, which in combination with silicon inverted tapers can serve to improve the fiber-chip coupling efficiency of future devices.

The combined results from all optimized processes resulted in devices of high and reproducible quality, and the results are the best achieved thus far in the research group. Although optical characterization remains to be done, the resulting structures shows characteristics that are promising for future fabrication of functional SOI nanophotonic devices such as photonic crystals and strip waveguide components. For example, the smoothness of fabricated PhC holes appear from top-view SEM inspection as similar or better to devices by others [100] that have demonstrated low loss SOI photonic crystal waveguides.

Future Work

There is a large amount of numerical and experimental work that can be done to build upon this thesis, and only what I consider to be the most interesting and important next steps for demonstrating interferometric PhC-based label-free optical biosensors are listed below.

- Optical characterization of fabricated devices should be done to compare the findings from numerical simulations with experimental results.
- Development of biofunctionalization schemes must be done in order to demonstrate label-free biosensing through specific binding of biomolecules.
- In order to interface between the optical chip and test solution, microfluidics is suggested as a promising platform.
- Although several 3D simulations were performed in this project, they were performed on a semi-powerful desktop workstation which limited the available grid resolution and sizes of computational domains. It is straightforward on distributed memory parallel computers to perform larger and more accurate 3D simulations of the same type, which is interesting for future work[1].

---

[1] In fact, both of the software packages used in this work (MPB [110] and Meep [111]) support parallel computing.

Appendices

Appendix A.

Eigenmode computations with MPB

This appendix aims to briefly introduce MPB as software to readers who wish to get started with simulating band structures of photonic crystals, and also present examples of the source code used in the simulations performed in this project. Generalities about the program and the physics it solves can be found in Section 3.1 and Section 4.1.1, and this section will focus on the practical procedure of setting up and running simulations.

Much of the information in this appendix originates from the well-written online reference for the software package [110], where a more comprehensive tutorial can be found.

Installation

The source code, installation files and installation guide are easily found online [110]. The installation is straightforward on Debian GNU/Linux, but solutions also exist for other systems.

Running Simulations

MPB uses so-called "control files" to specify the geometry we wish to study, the number of eigenvectors to compute, what to output, etc. These files are typically given the extension `.ctl`, but this is no requirement. The file paths are passed as arguments when calling MPB, which then performs the simulations specified in the files. If for example a simulation is defined in the file `foo.ctl`, the program is executed by calling it from the unix terminal with the following command:

```
unix%    mpb foo.ctl >& foo.out
```

Here, the program output is chosen to be written to an arbitrarily named file `foo.out`.

Setting Up Simulations

An example program for calculating the band structure of a hexagonal lattice PhC consisting of air holes surrounded by silicon is used to illustrate the procedure of defining a control file for MPB simulations. For simplicity, a 2D simulation is chosen, but a more complicated example code for simulating a linear defect in 3D slabs is shown in the next section. The resulting band structure for this code (only at higher resolution and more **k**-points) can be seen in Figure 5.2 (a).

In the beginning of the ctl-file, it is useful to define global parameters that will be used in the simulations. The comments in the code should explain which parameters are defined:

```
(define-param r 0.3);   defines hole radius r/a
(define-param eps 8.23);   effective permittivity of silicon

; define silicon material
(define silicon (make dielectric (epsilon eps)))

; semicolon is used for commenting in ctl-files!
```

After defining user-specific parameters, we need to set the value of several built-in parameters unless the default values should be used. The default values of all parameters can be found in the online reference.

```
(set! num-bands 10); how many eigenmodes to calculate
(set! default-material silicon); we want air holes in Si slab
```

Next, the lattice geometry and the resolution of the grid must be defined, using the basis vectors stated in Section 2.2.

```
; hexagonal lattice is defined with the following unit vectors:
(set! geometry-lattice (make lattice (size 1 1 no-size)
                         (basis1 (/ (sqrt 3) 2) 0.5)
                         (basis2 (/ (sqrt 3) 2) -0.5)))

(set! resolution 32); use a 32x32 computational grid
```

Since the default material is set to be silicon, we must create air holes at the appropriate points in our lattice (note that air is a predefined material in MPB):

```
(set! geometry (list (make cylinder (center 0 0 0) (material air)
                                    (radius r) (height infinity))))
```

The last step before we can run the simulations is to determine which **k**-points the eigenmodes should be computed for. These are chosen to be the high-symmetry points of the hexagonal lattice, with interpolating points between them:

```
(set! k-points (list (vector3 0 0 0)          ; Gamma
                     (vector3 0 0.5 0)        ; M
                     (vector3 (/ -3) (/ 3) 0) ; K
                     (vector3 0 0 0)))        ; Gamma

; number of interpolating k-points:
(set! k-points (interpolate 16 k-points))
```

Finally, the bands of TE and/or TM polarized modes are calculated by calling their respective `run`-functions:

```
(run-te); calculate TE-modes
(run-tm); calculate TM-modes
```

The reader is referred to the online user tutorial [112] for a more detailed explanation of performing MPB-simulations than that presented here. A tutorial considering data analysis and post-processing of simulation results can also be found online.

Example Simulation: Linear Defects

The above simulation considers an infinite 2D photonic crystal, but most of the work in this project has been about the dispersion characteristics of linear defects in 3D PhC slabs. Therefore, a basic setup for simulating a W1 missing row linear defect in the Γ-K-direction is shown here. The ctl-file is presented as a whole, with explanations left as comments in the code.

The reader should consult with Section 3.1.2 for background information about supercell approximations before embarking on this code. Also, it is pointed out that this code can be used for performing 2D simulations and 3D simulations of the same structure simply by setting the value of the parameter `3D` to `true` or `false`. Simple conditional statements in the code are used to give the silicon slab its appropriate thickness (infinite in 2D, `h` in 3D) and refractive index (effective index approximation needed in 2D). Likewise, the boolean value of the parameter `bottom_oxide` determines whether to simulate an air-bridge slab (`false`) or an silicon-on-insulator slab (`true`). All parameters defined through the statement `(define-param ...)` can conveniently be set as an argument when calling the program from the command line. This is highly useful for reusing code and for making shell scripts used for structural optimization or iterative simulations.

```
(define-param sy 7) ; (odd) number of lateral supercell periods
(define-param sz 4) ; height of supercell
(define-param 3D true) ; 3D or 2D simulation
(define-param bottom_oxide false) ; with or without oxide substrate
```

```
(define-param k_interp 4) ; the number of k points to interpolate
(define-param res_xy 32) ; in-plane grid resolution
(define-param res_z 16) ; vertical resolution (only used in 3D)
(define-param extra_bands 4) ; number of extra bands above first
                             ; defect-mode to compute

(define h 0.55) ; thickness of slab
(define r 0.3) ; radius of holes

; set (effective) dielectric constant for 2D/3D:
(define eps_silicon (if 3D 12.11 8.23))
(define eps_oxide 2.07)

; define materials:
(define si (make dielectric (epsilon eps_silicon)))
(define ox (make dielectric (epsilon eps_oxide)))


; hexagonal lattice with supercell in both y and z-direction
; (only supercell in z-direction for 3D simulations)
(set! geometry-lattice (make lattice
    (basis1 (/ (sqrt 3) 2) 0.5)
    (basis2 (/ (sqrt 3) 2) -0.5)
    (size 1 sy (if 3D sz no-size))))

(set! default-material si)

; add geometric features to form the PhC linear defect slab
(set! geometry
    (append
        ; create the bulk crystal holes over the supercell:
        (geometric-object-duplicates (vector3 0 1 0)
            (/ (+ sy -1) -2) (/ (+ sy -1) 2)
            (make cylinder (material air)(center 0)
                (radius r) (height infinity)) ; air hole
        )

        (list
            ; add a rod of silicon, to erase a row of rods
            ; and form a waveguide:
            (make cylinder (center 0) (radius r)
            (height infinity)(material si))
```

```
            ;add top cladding (air)
            (make block (center 0 0 (+ (/ sz 4 ) (/ h 4)))
            (material air) (size infinity infinity
            (- (/ sz 2) (/ h 2)) ))

            ; add bottom cladding (air or oxide)
            (make block (center 0 0 (+ (/ sz -4 ) (/ h -4)))
            (material (if bottom_oxide ox air))
            (size infinity infinity (- (/ sz 2) (/ h 2)) ))
)
)
)

(define Gamma (vector3 0 0 0))
(define K' (lattice->reciprocal (vector3 0.5 0 0))) ; edge of BZ
; interpolate between k-points:
(set! k-points (interpolate k_interp (list Gamma K')))

; set number of bands to compute
(set! num-bands (+ sy extra_bands))
(set-param! resolution  res_xy )

; run the simulation:
(if 3D
    (if bottom_oxide
        ; if true, do not assume vertical symmetry:
        (run display-zparities display-yparities)
        ; if false, assume vertical symmetry:
        (run-zeven display-yparities)
    )
; if 2D-simulation, only compute TE-modes
    (run-te display-yparities)
)
```

As seen in the code, it is necessary to calculate at least the number of bands corresponding to the number of lateral supercell periods to reach the modes that lie inside the band gap. This is because the supercell causes the original bands in the Brillouin zone to be “folded” back several times, in this case `supercell-y` times.

Regarding analysis of the band diagrams from simulations like this, the reader is encouraged to read up on projected band structures in for example Joannopoulos [18]. An easy way to project a band structure is to run the simulation above, but not include the line that creates the linear defect. In that case, the band structure is not perturbed by the linear defect, and a good estimation of the projected band structure can be found by increasing the size of the supercell until converging bands outlining the region of projected bulk bands are obtained.

Output Possibilites

MPB can perform a variety of field computations such as mode parities and group velocities, as well as output desired fields for specific eigenmodes. Due to the large number of possibilities, the reader is referred to the online reference for a complete list of supported functions [110].

Parallel Computing

A version on MPB with support for simulations on distributed-memory parallel machines also exists, and is called `mpb-mpi`. This is readily installed by following a specific installation guide in the online reference, and the functionality of the program is more or less the same as the serial version of MPB.

Even though the reader of this report most likely does not have access to distributed computer systems, a significant reduction in simulation time can be achieved by using parallelization on a single computer since it allows for all the available processor cores to be used. The serial version of MPB runs as a single thread, which means only one core is utilized. The memory requirements for MPB have been observed to be modest, which means that the processing speed is the limiting factor, making such parallelization a big improvement in simulation time. After installing the parallel version of MPB, the program can be executed by the following command:

```
unix%    mpirun -np 4 mpb-mpi foo.ctl
```

The number 4 determines the number of processors (cores) that will be turned on, and can be chosen to whatever is available on a particular machine.

Appendix B.

FDTD-simulations with Meep

This appendix serves the purpose of introducing the reader to finite-difference time-domain simulations with Meep. Focus is put on describing simulations in practice by showing example code and discussing important technical subtleties to consider when working with Meep. Brief general theory about time-domain simulations and FDTD can be found in Section 3.1.

Installation

As for MIT Photonic Bands, Meep exists as a precompiled software package for Debian GNU/Linux, and can be installed through the terminal:

```
unix%    apt-get install meep
```

See the online reference for installing Meep on other operating systems.

Example Simulation: Linear Defects

Since the procedure of setting up and running Meep-simulations is equivalent to that described for MPB in Appendix A, we jump straight to presenting example code for simulating the transmission through a photonic crystal linear defect. A schematic of the simulation domain can be seen in Figure 4.4. The code below can be used for simulating structures in 2D, 3D air-bridge slabs and 3D SOI slabs by changing the values of boolean variables in the script. As discussed in Section 4.1.2, a reference run must be performed for correctly normalizing the transmission through the PhC waveguide, and this is done by setting `ref_run=true`.

```
; booleans used for defining type of simulation:
(define-param ref_run false); reference run or not
(define-param 3D false); 3D or 2D simulation
(define-param bottom_oxide false); SOI or suspended membrane
(define-param nfreq 1000); number of freqs for finding flux

; constants that define the geometry:
```

```
(define A (/ (sqrt 3) 2)); row-separation in Gamma-M direction
(define r 0.3); hole radius
(define wg_width (* 2 (- A rad))); width of incoupling waveguides
(define wg_length 2); length of inclupling waveguides
(define pml_t 1); thickness of PML layer
(define flux_sep 0.5); distance from flux plane to PML
(define source_sep 0.25); distance from source plane to PML
(define numx 21); number of periods along waveguide (x-direction)
(define numy 15); (odd) number of periods in the y-direction
(define sx (+ numx (* 2 wg_length) (* 2 pml_t))); domain size
                                                  ; in x-direction
(define sy (+ (* numy A) (* 2 pml_t))); domain size in y-direction
(define flux_pos_x (- (/ sx 2) (+ pml_t flux_sep)))
(define source_pos_x (- (/ sx 2) (+ pml_t source_sep)))
(define h 0.55)
(define sz (+ (* 2 pml_t) (* 9 h))); domain size in z-direction

; excitation source properties:
(define fcen 0.3); pulse center frequency
(define df 0.1); pulse width (in frequency)

; make simulation domain:
(set! geometry-lattice (make lattice
                       (size sx sy (if 3D sz no-size))))

; set (effective) dielectric constants, and define materials:
(define eps_silicon (if 3D 12.11 8.23))
(define eps_oxide 2.07)
(define si (make dielectric (epsilon eps_silicon)))
(define ox (make dielectric (epsilon eps_oxide)))

; define part of the simulation geometry
(set! geometry (list
    (if ref_run
        ; waveguide across entire cell:
        (make block (center 0 0 0) (material si)
                    (size infinity wg_width (if 3D h infinity)))
        ; slab of length numx:
        (make block (center 0 0 0) (material si)
                    (size numx infinity (if 3D h infinity)))
    )
))
```

```
; make PhC holes if not reference run
(if (not ref_run)
    (set! geometry (append geometry
        (geometric-objects-duplicates
        (vector3 0.5 (/ (sqrt 3) 2) 0) (- (+ numx 1)) (+ numx 1)
        (geometric-object-duplicates
        (vector3 0.5 (-(/ (sqrt 3) 2.0)) 0) (- (+ numx 1))
        (+ numx 1)  (make cylinder   (center 0 0 0) (radius rad)
        (height infinity)  (material air))))
    )
))

; make more features for non-reference run
(if (not ref_run)
    (set! geometry (append geometry (list
        ; cover center row of holes with silicon:
        (make block (center 0 0 0) (material si)
        (size infinity (* 2 rad) (if 3D h infinity)))
        ; make input and output waveguides:
        (make block (center (/ (+ pml_t wg_length numx) -2) 0 0)
        (material si)
        (size (+ pml_t wg_length) wg_width (if 3D h infinity)))
        (make block (center (/ (+ pml_t wg_length numx) 2) 0 0)
        (material si)
        (size (+ pml_t wg_length) wg_width (if 3D h infinity)))
        (make block (center 0 (/ sy  2) 0) (material si)
        (size numx (* pml_t 2) (if 3D h infinity)))
        (make block (center 0 (/ sy -2) 0) (material si)
        (size numx (* pml_t 2) (if 3D h infinity)))
    )))
)

; add silicon dioxide substrate to consider SOI-PhC:
(if bottom_oxide
    (set! geometry (append geometry (list
        (make block (center 0 0 (+ (/ sz -4 ) (/ h -4)))
        (material ox)
        (size infinity infinity (- (/ sz 2) (/ h 2)) ))
    )))
)
```

```
; set up excitation current source:
(set! sources (list
    (make source
        (src (make gaussian-src (frequency fcen) (fwidth df)))
        (component Ey) (center (* source_pos_x -1) 0 0)
        (size 0 wg_width  (if 3D h infinity))
)))

; define a perfectly matched layer around simulation domain
(set! pml-layers (list (make pml (thickness pml_t))))

; define mirror symmetries present in simulation domain with
; appropriate phases (z-symm must be removed for SOI-simulations):
(set! symmetries (list
    (make mirror-sym (direction Y) (phase -1))
    (make mirror-sym (direction Z))
    )
)

; flux plane at output waveguide:
(define trans
    (add-flux fcen df nfreq (make flux-region
    (center flux_pos_x 0 0) (size 0 (* wg_width 2)
    (if 3D (* h 2) infinity ))))
)

; run simulation until Ey-field at flux plane has decayed by 1e3:
(run-sources+
    (stop-when-fields-decayed 200 Ey
    (vector3 flux_pos_x 0 0) 1e-3)
    (at-beginning output-epsilon)
)

(display-fluxes trans); print out the accumulated fluxes at output
```

Harmonic Inversion and Resonant Modes

The freely available program “Harminv” [113] can be called directly in Meep simulations to extract information about resonant modes such as their amplitudes and Q-factors. It solves the problem of *harmonic inversion* of a discrete series of time-domain data, and can in principle provide better accuracy than that possible by extracting FFT peaks since it makes stronger (but valid) assumptions about the specific form of the signal. It can also be faster than FFT since it is not limited by the time-frequency uncertainty principle. Further information about the program can be found at its website [113], and details about the algorithm it implements can be found in Mandelshtam [114].

Tips'n Tricks

A few tricks that make the FDTD-simulations in Meep easier and/or quicker are listed below:

- Take advantage of symmetries in the simulation domain, see the code above for examples.
- Use command line arguments such as `3D=true` when executing Meep in order to use the same code for simulating several similar structures.
- Perform initial simulations at low resolutions and for few time-steps, and increase both to desired values after everything is confirmed to be set up correctly.
- Use broadband sources to get overview transmission spectra. Often, these will point out interesting frequency ranges which following simulations can cover with narrowband sources.
- Gaussian sources are useful for flux spectra, and continuous sources are useful for steady-state responses to a single frequency. Note however that it is important to switch the continuous sources on gradually to avoid excitation of high-frequency components.
- Meep supports a number of different field computations and output functions, and the reader is referred to the online reference for a list of these [111].

Numerical Artifacts from Early Simulation Stop

An important consideration in time-domain simulations is for how long a given simulation should be run. The short answer is "long enough for the excited fields to have decayed to negligible values". It is however not a trivial task to determine what this corresponds to, and too short times are demonstrated in the following to introduce nonphysical features in transmission spectra. In other words, care must be taken when interpreting such spectra. Consider again the transmission through a liner defect waveguide as seen in Figure 4.4. After 300 time steps, the Gaussian wave packet has mostly passed through the structure, and the field amplitude at the output flux region had decayed by a factor 10^3 compared to

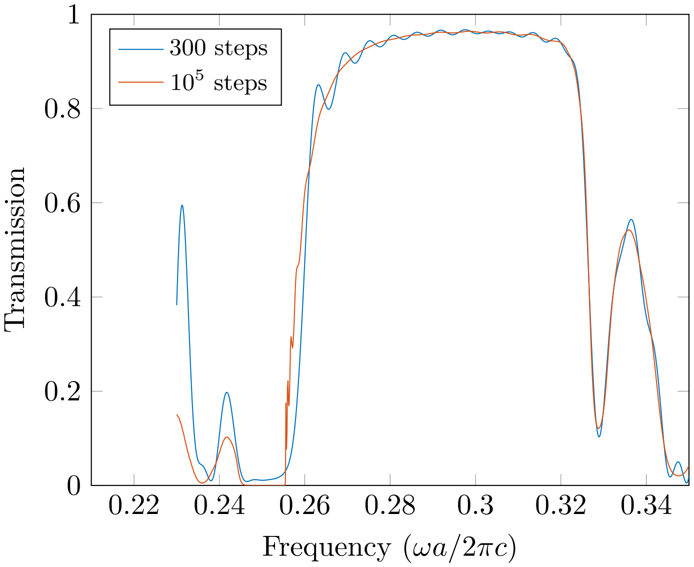

Figure B.1.: FDTD-simulated transmission spectra of a $21a$ long W1 waveguide, see Figure 4.4. The legend refers to the number of time steps computed before stopping the simulation.

the maximum registered amplitude. The time-stepping was thus stopped, and the transmission through the structure was found from the accumulated Fourier transformed fields and is shown as the blue line in Figure B.1.

As evident, although the transmission is high in the frequency range corresponding to the band gap above the onset of the ground mode, there are oscillations present. The obvious first explanation is that they correspond to Fabry-Pérot resonances from multiple reflections at the coupling region between the PhC and strip waveguides. However, the free spectral range[1] ($\Delta\nu = c/2n_gL$) is found to not match the physical waveguide length $L = 21a$ and the group indices n_g found as the inverse slope of the ground mode dispersion in Figure 5.5 (a).

Similar results of FDTD-spectrum oscillations are found in [102], where they are concluded to be a numerical artifact caused by early truncation of the time-domain simulation. Different frequency components of the broadband excitation decay at different rates, causing ripples in the spectrum since non-negligible amounts of these components has not decayed sufficiently. Particularly near the ground

---

[1] The free spectral range is notably frequency dependent due to dispersion of the ground mode which results in a varying group index n_g.

mode band edge, this effect is significant due to the flat dispersion and thus small group velocity.

Two methods for confirming the nonphysical interpretation of the features were performed: (i) running the same simulation for many more time steps (10 000 compared to 300), and (ii) computing only 300 time steps, but using a narrower excitation source that does not cover the slow-light modes near the band edge. Both methods were observed to remove the oscillations, but only (i) is useful since it covers the original frequency range of interest. The red line in Figure B.1 shows how the longer simulation reduces the effect of stopping the time-domain simulation before all frequency components have decayed sufficiently.

The simulations in Figure B.1 are done in 2D, but the described effect of early simulation truncation is equally valid for 3D systems. The quick-fix of increasing the total number of time steps is unfortunate in terms of severely increasing the computation time – particularly when dealing with slowly decaying modes such as resonances or slow light. A trade-off between computation time and avoiding excessive numerical artifacts has been found necessary in this project. For future work, it is suggested to investigate alternative workarounds such as using windowing functions to remove these numerical artifacts from FDTD transmission spectra.

Appendix C.

Image Analysis for Fabrication Quality Assesment

A significant amount of post processing of scanning electron micrographs has been done in this project, primarily with the purpose of measuring the size of various features. Examples are determination of etch depths, waveguide widths and importantly for in study of hole-slab photonic crystals: determination of hole radii. The Image Processing Toolbox in MATLAB® has been found valuable in this process, enabling programmatic measurements of hole sizes and line edge roughness (LER) from input SEM images.

In addition to removing the human influence on determining LER and fitting circles to imaged holes, fast analysis of several images is possible when using programmatic methods. The latter means that statistical information about the hole size distribution is readily obtained. Although not covered in detail in this project, such information can be used to predict device performance. Numerous studies have been performed on the effects of fabrication induced disorder such as hole size fluctuations, inaccurate hole positions, sidewall roughness etc. [115, 116, 52, 51, 50, 117].

C.1. Hole Size Measurements

Without going into depths about the image processing theory for detecting circles, it is achieved using an edge-detecting “Circle Hough Transform” [118]. A voting-based algorithm is used to see which objects are the best candidates for being a circle with a radius within a user-specified range.

The SEM images recorded in this project display holes as bright circles where the contrast comes from significantly enhanced secondary electron signal caused by an edge effect of the interaction volume [76, Ch. 5]. The MATLAB® implementation for circle detection is capable of finding circular objects that are both brighter and darker than the background. In practice for the SEM images captured in this project, this means finding the inner and outer bounding circles of the hole edge.

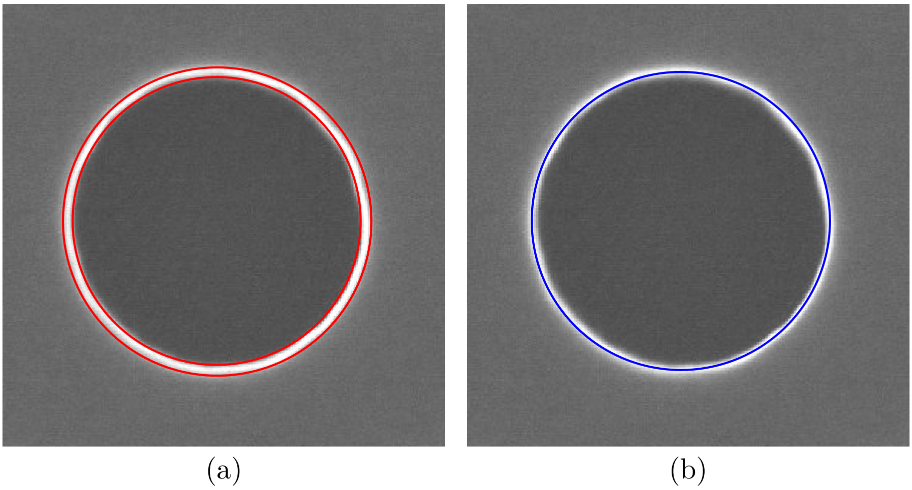

Figure C.1.: Example SEM image of a photonic crystal hole showing (a) the superimposed inner and outer bounding circles, and (b) a circle with the averaged radius.

An example can be seen in Figure C.1 (a), where the inner and outer radii are found to be 133 nm and 142 nm, respectively.

An assumption is made in that the physical edges of holes correspond to circles with a radius midway between the inner and outer circles. This is shown in Figure C.1 (b) as a hole with radius 138 nm. The validity of this assumption is not considered further, but since this particular procedure is used for measuring all holes in this project, it is assumed that results obtained from imaging different structures are transferable from sample to sample. It was confirmed that the hole radii determined for the same holes were consistent when imaged at different magnifications.

Figure C.2 shows an example distribution of hole radii for a SEM image captured in this project. This particular image covered an area containing 174 photonic crystal holes. From the data, the average radius is found to be 137.9 nm, and a distribution width of 0.49 nm (standard deviation). It is pointed out that SEM inspection itself as a method for determining hole sizes can introduce large systematic errors because different electron detectors and detector settings can provide differing contrasts between a hole and its edge. This has been investigated by Beggs et al. [119], which conclude that optical methods based on measuring the cut-off frequency for W1 PhC waveguides provide more accurate size determination. Nevertheless, SEM characterization is useful during fabrication

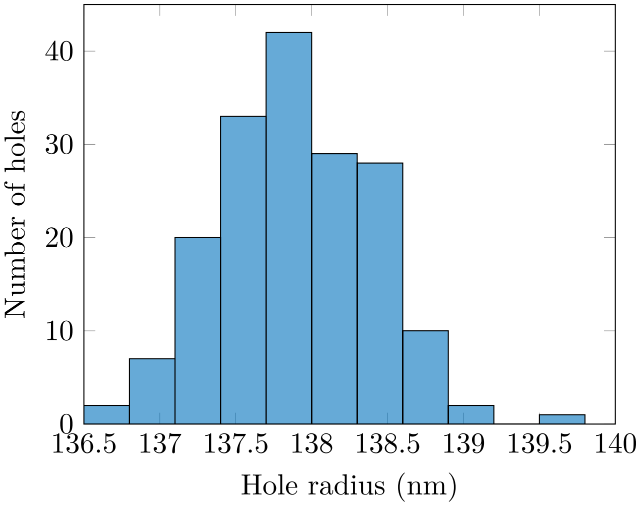

Figure C.2.: Hole size distribution measured from image analysis of a scanning electron micrograph containing 174 photonic crystal holes.

process development, and a combination of several methods is considered the best way of determining hole sizes.

In conclusion, the described programmatic method of investigating SEM images is a quick and easy way to determine hole sizes and evaluate consistency across a sample. Quantitative data on the quality of a given fabrication process is provided through the width of the size distribution. Care must however be taken when interpreting the data since SEM imaging can give varying results depending on imaging conditions. Alternative methods of determining hole sizes should be used in combination with SEM image analysis for increased reliability. It is left as a suggestion for later studies to investigate the effect of different hole size distributions on device performance.

C.2. Line Edge Roughness Measurements

Algorithms exist in MATLAB® that detect edges in images as a path of a rapid change in intensity, in a function called `edge()`. Although several implementations are available, the "Canny method" [120] has been found the most reliable when investigating waveguide edges in SEM images in this project. The detected bounding edge of an example waveguide found using this method is shown in Figure C.3. As can be seen, the detection threshold is appropriately chosen since

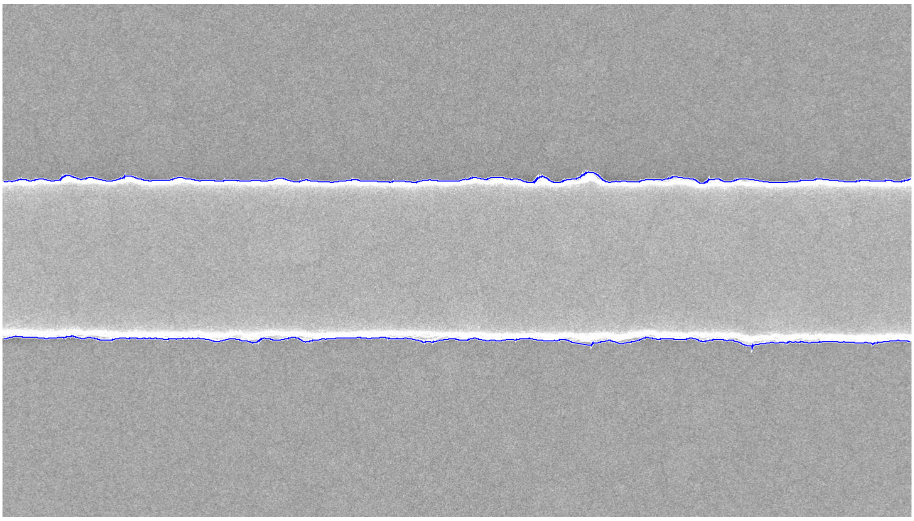

Figure C.3.: SEM image of a strip waveguide where the edges (blue) have been found using edge-detecting image analysis.

only the bounding edges of the waveguide are detected as edges. The brightness and contrast of the SEM image have been adjusted to better display the waveguide edge.

The output from the edge detecting algorithm is only a binary image the same size as the input, filled with 1s where the function finds edges in the input image and 0s elsewhere. These must be sorted into two arrays of x and y-positions corresponding to the lower and upper edge. The next step is to subtract a linear baseline from the edges, in case the input image is not perfectly horizontally oriented. This is achieved using linear regression. After subtracting the baseline, the root-mean-square deviation from the average value is found using the standard formula

$$\sigma = \sqrt{\frac{1}{N}\sum_{i=1}^{N} y_i^2}, \tag{C.1}$$

where N is the total number of sampling points along the trace and y_i is the distance of the ith datapoint from the mean line (already accounted for when subtracting the baseline), which in the example case shown in Figure C.3 yields an RMS roughness of $\sigma = 5.0\,\text{nm}$.

It is noted that this technique for measuring LER has significant flaws. It was observed during this project that the same waveguides had qualitatively higher roughness when imaged in tilted cross-sections compared to top-view SEM images, since the latter only shows a vertical projection of the sidewall contour. The technique is thus assumed to only give a lower bound for the LER, and other methods such as that used in Sparacin et al. [69] of correlating propagation losses for waveguides of different widths towards theoretical models for sidewall scattering is considered a better way for determining σ. Still, the method is useful for quantifying the quality of structures during fabrication process development.

Bibliography

[1] S. Johnson and J. Joannopoulos, "Block-iterative frequency-domain methods for Maxwell's equations in a planewave basis," *Optics Express*, vol. 8, no. 3, p. 173, 2001.

[2] A. F. Oskooi, D. Roundy, M. Ibanescu, P. Bermel, J. Joannopoulos, and S. G. Johnson, "Meep: A flexible free-software package for electromagnetic simulations by the FDTD method," *Computer Physics Communications*, vol. 181, pp. 687–702, mar 2010.

[3] L. G. Holmen, "Simulations of Photonic Crystal Mach-Zehnder Interferometers for Biosensing Applications." Project report, Norwegian University of Science and Technology, 2015.

[4] J. Høvik, "Photonic crystal waveguide fabrication." Master's thesis, Norwegian University of Science and Technology, 2012.

[5] M. Lorvik, "Photonic crystal structures design and fabrication." Master's thesis, Norwegian University of Science and Technology, 2013.

[6] L. Vigen, "Silicon racetrack resonator." Master's thesis, Norwegian University of Science and Technology, 2014.

[7] T. Bolstad, "Fabrication of a silicon photonic crystal biosensor." Master's thesis, Norwegian University of Science and Technology, 2014.

[8] S. M. Martinussen, "Silicon photonic components: characterization and optimization of fabrication." Master's thesis, Norwegian University of Science and Technology, 2015.

[9] Z. Fang and C. Z. Zaho, "Recent Progress in Silicon Photonics, a Review," *ISRN Optics*, vol. 2012(42869), 2012.

[10] O. Kononchuk and B.-Y. Nguyen, *Silicon-on-insulator (SOI) Technology*. Elsevier, 2014.

[11] E. Yablonovitch, "Inhibited Spontaneous Emission in Solid-State Physics and Electronics," *Physical Review Letters*, vol. 58, no. 20, pp. 2059–2062, 1987.

[12] S. John, “Strong localization of photons in certain disordered dielectric superlattices,” *Physical Review Letters*, vol. 58, no. 23, pp. 2486–2489, 1987.

[13] J. D. Joannopoulos, P. R. Villeneuve, and S. Fan, “Photonic crystals: putting a new twist on light,” *Nature*, vol. 386, no. 6621, pp. 143–149, 1997.

[14] M. R. Lee and P. M. Fauchet, “Two-dimensional silicon photonic crystal based biosensing platform for protein detection,” *Optics Express*, vol. 15, no. 8, p. 4530, 2007.

[15] D. Dorfner, T. Zabel, T. Hürlimann, N. Hauke, L. Frandsen, U. Rant, G. Abstreiter, and J. Finley, “Photonic crystal nanostructures for optical biosensing applications,” *Biosensors and Bioelectronics*, vol. 24, no. 12, pp. 3688–3692, 2009.

[16] W.-C. Lai, S. Chakravarty, Y. Zou, and R. T. Chen, “Silicon nano-membrane based photonic crystal microcavities for high sensitivity bio-sensing.,” *Optics letters*, vol. 37, no. 7, pp. 1208–10, 2012.

[17] X. Fan, I. M. White, S. I. Shopova, H. Zhu, J. D. Suter, and Y. Sun, “Sensitive optical biosensors for unlabeled targets: a review.,” *Analytica chimica acta*, vol. 620, no. 1-2, pp. 8–26, 2008.

[18] J. D. Joannopoulos, S. Johnson, J. N. Winn, and R. D. Meade, *Photonic crystals: molding the flow of light.* Princeton University Press, 2008.

[19] W. Bogaerts, *Nanophotonic waveguides and photonic crystals in silicon-on-insulator.* PhD thesis, Ghent University, 2004.

[20] J. Bravo-Abad, A. Rodriguez, P. Bermel, S. G. Johnson, J. D. Joannopoulos, and M. Soljacic, “Enhanced nonlinear optics in photonic-crystal microcavities,” *Optics Express*, vol. 15, no. 24, p. 16161, 2007.

[21] F. Bloch, “Über die Quantenmechanik der Elektronen in Kristallgittern,” *Zeitschrift für Physik*, vol. 52, no. 7-8, pp. 555–600, 1929.

[22] D. J. Griffiths, *Introduction to Quantum Mechanics.* Pearson Prentice Hall, 2005.

[23] J. Høvik, “Characterization of photonic crystals using frequency-domain simulation methods.” Project report, Norwegian University of Science and Technology, 2011.

[24] C. Kittel, *Introduction to solid state physics.* John Wiley & Sons, Inc, 2005.

[25] B. E. A. Saleh and M. C. Teich, *Fundamentals of Photonics, 2nd Edition.* John Wiley & Sons, Inc, 2007.

[26] S. G. Johnson, S. Fan, P. R. Villeneuve, J. D. Joannopoulos, and L. A. Kolodziejski, “Guided modes in photonic crystal slabs,” *Physical Review B*, vol. 60, no. 8, pp. 5751–5758, 1999.

[27] B. Ellis, M. A. Mayer, G. Shambat, T. Sarmiento, J. Harris, E. E. Haller, and J. Vučković, “Ultralow-threshold electrically pumped quantum-dot photonic-crystal nanocavity laser,” *Nature Photonics*, vol. 5, no. 5, pp. 297–300, 2011.

[28] D. Ripin, G. Petrich, P. Villeneuve, E. Thoen, J. Joannopoulos, E. Ippen, and L. Kolodziejski, “One-dimensional photonic bandgap microcavities for strong optical confinement in GaAs and GaAsAlxOy semiconductor waveguides,” *Journal of Lightwave Technology*, vol. 17, no. 11, pp. 2152–2160, 1999.

[29] M. R. Lee and P. M. Fauchet, “Nanoscale microcavity sensor for single particle detection,” *Optics Letters*, vol. 32, no. 22, p. 3284, 2007.

[30] C. Jamois, R. Wehrspohn, L. Andreani, C. Hermann, O. Hess, and U. Gösele, “Silicon-based two-dimensional photonic crystal waveguides,” *Photonics and Nanostructures - Fundamentals and Applications*, vol. 1, no. 1, pp. 1–13, 2003.

[31] Z. Hu and Y. Y. Lu, “Improved bends for two-dimensional photonic crystal waveguides,” *Optics Communications*, vol. 284, no. 12, pp. 2812–2816, 2011.

[32] P. Xing, P. Borel, L. Frandsen, A. Harpøth, and M. Kristensen, “Optimization of bandwidth in 60 degree photonic crystal waveguide bends,” *Optics Communications*, vol. 248, no. 1-3, pp. 179–184, 2005.

[33] I. Ntakis, P. Pottier, and R. M. De La Rue, “Optimization of transmission properties of two-dimensional photonic crystal channel waveguide bends through local lattice deformation,” *Journal of Applied Physics*, vol. 96, no. 1, p. 12, 2004.

[34] L. H. Frandsen, A. Harpøth, P. I. Borel, M. Kristensen, J. S. Jensen, and O. Sigmund, “Broadband photonic crystal waveguide 60 degree bend obtained utilizing topology optimization,” *Optics Express*, vol. 12, no. 24, p. 5916, 2004.

[35] A. Chutinan, M. Okano, and S. Noda, “Wider bandwidth with high transmission through waveguide bends in two-dimensional photonic crystal slabs,” *Applied Physics Letters*, vol. 80, no. 10, p. 1698, 2002.

[36] S. A. Suliman, “Silicon Photonics for Telecommunications and Biomedicine,” *Journal of Nanophotonics*, vol. 6, no. 1, p. 060201, 2012.

[37] X.-q. Li and Y. Xu, “Optical sensing by using Photonic Crystal based Mach–Zehnder interferometer,” *Optics Communications*, vol. 301-302, pp. 7–11, 2013.

[38] A. Martínez, P. Sanchis, and J. Martí, “Mach–Zehnder interferometers in photonic crystals,” *Optical and Quantum Electronics*, vol. 37, no. 1-3, pp. 77–93, 2005.

[39] A. E. Miroshnichenko and Y. S. Kivshar, “Mach–Zehnder–Fano interferometer,” *Applied Physics Letters*, vol. 95, no. 12, p. 121109, 2009.

[40] C.-Y. Liu and L.-W. Chen, “Tunable photonic-crystal waveguide Mach-Zehnder interferometer achieved by nematic liquid-crystal phase modulation,” *Optics Express*, vol. 12, no. 12, p. 2616, 2004.

[41] M. H. Shih, W. J. Kim, W. Kuang, J. R. Cao, H. Yukawa, S. J. Choi, J. D. O’Brien, P. D. Dapkus, and W. K. Marshall, “Two-dimensional photonic crystal Mach–Zehnder interferometers,” *Applied Physics Letters*, vol. 84, no. 4, p. 460, 2004.

[42] F. Prieto, B. Sepulveda, and A. Calle, “An integrated optical interferometric nanodevice based on silicon technology for biosensor applications,” *Nanotechnology*, vol. 14, pp. 907–912, 2003.

[43] P. Klan, T. Solomek, C. G. Bochet, R. Givens, M. Rubina, V. Popik, A. Kostikov, and J. Wirz, “Photoremovable Protecting Groups in Chemistry and Biology: Reaction Mechanisms and Efficacy,” *Chemical Reviews*, vol. 113, pp. 119–191, 2012.

[44] R. E. Saunders and B. Derby, “Inkjet printing biomaterials for tissue engineering: bioprinting,” *International Materials Reviews*, vol. 59, no. 8, pp. 430–448, 2014.

[45] D. K. Sparacin, *Process and design techniques for low loss integrated silicon photonics.* PhD thesis, Massachusetts Institute of Technology, 2006.

[46] P. Dumon, W. Bogaerts, V. Wiaux, J. Wouters, S. Beckx, J. Van Campenhout, D. Taillaert, B. Luyssaert, P. Bienstman, D. Van Thourhout, and R. Baets, “Low-loss SOI photonic wires and ring resonators fabricated with deep UV lithography,” *IEEE Photonics Technology Letters*, vol. 16, no. 5, pp. 1328–1330, 2004.

[47] S. Zhu, G. Q. Lo, and D. L. Kwong, “Low-loss amorphous silicon wire waveguide for integrated photonics: effect of fabrication process and the thermal stability.,” *Optics express*, vol. 18, no. 24, pp. 25283–25291, 2010.

[48] Y. Vlasov and S. McNab, “Losses in single-mode silicon-on-insulator strip waveguides and bends.,” *Optics express*, vol. 12, no. 8, pp. 1622–1631, 2004.

[49] R. Sun, *Advanced materials, process, and designs for silicon photonic integration.* PhD thesis, Massachusetts Institute of Technology, 2009.

[50] Y. Tanaka, T. Asano, Y. Akahane, B. S. Song, and S. Noda, “Theoretical investigation of a two-dimensional photonic crystal slab with truncated cone air holes,” *Applied Physics Letters*, vol. 82, no. 11, pp. 1661–1663, 2003.

[51] D. Wang, Z. Yu, Y. Liu, S. Zhou, X. Guo, and C. Shu, “Slight disorder effects in two dimensional photonic crystal structures,” *Optik*, vol. 125, no. 18, pp. 5418–5421, 2014.

[52] D. Gerace and L. Andreani, “Low-loss guided modes in photonic crystal waveguides.,” *Optics express*, vol. 13, no. 13, pp. 4939–4951, 2005.

[53] L. Vivien and L. Pavesi, *Handbook of silicon photonics.* Taylor & Francis, 2013.

[54] J. Jiang and Y. Zhang, “Nonlinear dynamic analysis of speech from pathological subjects,” *Electronics Letters*, vol. 38, no. 6, pp. 294–295, 2002.

[55] S. McNab, N. Moll, and Y. Vlasov, “Ultra-low loss photonic integrated circuit with membrane-type photonic crystal waveguides,” *Optics Express*, vol. 11, no. 22, p. 2927, 2003.

[56] S. G. Johnson, “Notes on Perfectly Matched Layers (PMLs),” 2010. Available online at `http://math.mit.edu/~stevenj/18.369/pml.pdf`.

[57] A. F. Oskooi, L. Zhang, Y. Avniel, and S. G. Johnson, “The failure of perfectly matched layers, and towards their redemption by adiabatic absorbers.,” *Optics express*, vol. 16, no. 15, pp. 11376–11392, 2008.

[58] A. Oskooi and S. G. Johnson, “Distinguishing correct from incorrect PML proposals and a corrected unsplit PML for anisotropic, dispersive media,” *Journal of Computational Physics*, vol. 230, no. 7, pp. 2369–2377, 2011.

[59] P. R. Loh, A. F. Oskooi, M. Ibanescu, M. Skorobogatiy, and S. G. Johnson, “Fundamental relation between phase and group velocity, and application to the failure of perfectly matched layers in backward-wave structures,” *Physical Review E - Statistical, Nonlinear, and Soft Matter Physics*, vol. 79, no. 6, pp. 1–4, 2009.

[60] S. G. Johnson, P. R. Villeneuve, S. Fan, and J. D. Joannopoulos, “Linear waveguides in photonic-crystal slabs,” *Physical Review B*, vol. 62, no. 12, pp. 8212–8222, 2000.

[61] A. Taflove and S. C. Hagness, *Computational electrodynamics: The finite-difference time-domain method.* Artech: Norwood, MA, 2005.

[62] J. B. Schneider, "Understanding the finite-difference time-domain method," 2010. Available online at `http://www.eecs.wsu.edu/~schneidj/ufdtd/`.

[63] G. Chavoor, X. Jin, A. Ellaboudl, X.-x. Fub, X.-n. Kangb, B. Zhangb, and G.-y. Zhangb, "Light Extraction Improvement of GaN LEDs using Nano-scale Top Transmission Gratings," *Proc. SPIE*, vol. 8123, pp. 1–8, 2011.

[64] K. S. Yee, "Numerical solution of initial boundary value problems involving Maxwell's equations in isotropic media," *IEEE Transactions on Antennas and Propagation*, vol. 14, no. 3, pp. 302–307, 1966.

[65] M. Hammer and O. V. Ivanova, "Effective index approximations of photonic crystal slabs: A 2-to-1-D assessment," *Optical and Quantum Electronics*, vol. 41, no. 4, pp. 267–283, 2009.

[66] M. Qiu, "Effective index method for heterostructure-slab-waveguide-based two-dimensional photonic crystals," *Applied Physics Letters*, vol. 81, no. 7, p. 1163, 2002.

[67] P. Strasser, G. Stark, F. Robin, D. Erni, K. Rauscher, R. Wüest, and H. Jäckel, "Optimization of a 60 degree waveguide bend in InP-based 2D planar photonic crystals," *Journal of the Optical Society of America B*, vol. 25, no. 1, p. 67, 2008.

[68] A. Chutinan and S. Noda, "Waveguides and waveguide bends in two-dimensional photonic crystal slabs," *Physical Review B*, vol. 62, no. 7, pp. 4488–4492, 2000.

[69] D. K. Sparacin, S. J. Spector, and L. C. Kimerling, "Silicon waveguide sidewall smoothing by wet chemical oxidation," *Journal of Lightwave Technology*, vol. 23, no. 8, pp. 2455–2461, 2005.

[70] S. K. Selvaraja, P. Jaenen, W. Bogaerts, D. Van Thourhout, P. Dumon, and R. Baets, "Fabrication of photonic wire and crystal circuits in silicon-on-insulator using 193-nm optical lithography," *Journal of Lightwave Technology*, vol. 27, no. 18, pp. 4076–4083, 2009.

[71] M. Quirk and J. Serda, *Semiconductor Manufacturing Technology.* Prentice Hall, 2001.

[72] M. Ohring, *Materials science of thin films.* Elsevier, 2002.

[73] F. Karouta, K. Vora, J. Tian, and C. Jagadish, “Structural, compositional and optical properties of PECVD silicon nitride layers,” *Journal of Physics D: Applied Physics*, vol. 45, no. 44, p. 445301, 2012.

[74] K. Narayanan, *Hydrogenated amorphous silicon photonics.* PhD thesis, Rochester Institute of Technology, 2011.

[75] A. M. Mohammad, M. Muhammad, S. K. Dew, and M. Stepanova, *Nanofabrication.* Springer, 2012.

[76] R. F. Egerton, *Physical principles of electron microscopy.* Springer, 2005.

[77] J. M. Ryan, “A study of the effect of ultrasonic agitation during development of poly(methylmethacrylate) for ultrahigh resolution electron-beam lithography,” *Journal of Vacuum Science & Technology B: Microelectronics and Nanometer Structures*, vol. 13, no. 6, p. 3035, 1995.

[78] A. N. Broers, A. C. F. Hoole, and J. M. Ryan, “Electron beam lithography - Resolution limits,” *Microelectronic Engineering*, vol. 32, pp. 131–142, 1996.

[79] C. Vieu, F. Carcenac, A. Pepin, Y. Chen, M. Mejias, A. Lebib, L. Manin-Ferlazzo, L. Couraud, and H. Launois, “Electron beam lithography: resolution limits and applications,” *Applied Surface Science*, vol. 164, no. 1, pp. 111—-117, 2000.

[80] V. R. V. Manfrinato, L. Zhang, D. Su, H. Duan, R. G. Hobbs, E. A. Stach, and K. K. Berggren, “Resolution Limits of Electron-Beam Lithography toward the Atomic Scale,” *Nano Letters*, vol. 13, no. 4, pp. 1555–1558, 2013.

[81] A. Khursheed, *Scanning Electron Microscope Optics and Spectrometers.* World Scientific, 2010.

[82] Allresist GmbH, “CSAR 62 – Positive tone e-beam resist datasheet,” 2014. Available online at `http://www.allresist.com/wp-content/uploads/sites/2/2014/03/allresist_produktinfos_ar-p6200_englisch.pdf`.

[83] MicroChem, “PMMA – Positive tone e-beam resist datasheet,” 2001. Available online at `http://www.microchem.com/pdf/PMMA_Data_Sheet.pdf`.

[84] S. L. Lai, D. Johnson, and R. Westerman, “Aspect ratio dependent etching lag reduction in deep silicon etch processes,” *Journal of Vacuum Science & Technology A: Vacuum, Surfaces, and Films*, vol. 24, no. 4, p. 1283, 2006.

[85] Filmetrics, “F20 - Taking the mystery out of thin film measurements,” 2006.

[86] B. Murty, P. Shankar, B. Raj, B. B. Rath, and J. Murday, *Textbook of nanoscience and nanotechnology.* Springer, 2013.

[87] P. Eaton and P. West, *Atomic force microscopy.* Oxford University Press, 2010.

[88] E. D. Palik, *Handbook of Optical Constants of Solids.* Academic Press, 1998.

[89] A. Lavrinenko, P. I. Borel, L. H. Frandsen, M. Thorhauge, A. Harpøth, M. Kristensen, T. Niemi, and H. M. H. Chong, "Comprehensive FDTD modelling of photonic crystal waveguide components," *Optics Express*, vol. 12, no. 2, p. 234, 2004.

[90] J. Lu and J. Vučković, "Nanophotonic computational design," *Optics Express*, vol. 21, no. 11, p. 13351, 2013.

[91] R. Wilson, T. J. Karle, I. Moerman, and T. F. Krauss, "Efficient photonic crystal Y-junctions," *Journal of Optics A: Pure and Applied Optics*, vol. 5, no. 4, pp. S76–S80, 2003.

[92] MicroChem, "SU-8 – Negative tone photoresist datasheet," 2002. Available online at `http://www.microchem.com/pdf/SU8_2-25.pdf`.

[93] B. Bilenberg, S. Jacobsen, M. Schmidt, L. Skjolding, P. Shi, P. Bøggild, J. Tegenfeldt, and A. Kristensen, "High resolution 100kV electron beam lithography in SU-8," *Microelectronic Engineering*, vol. 83, no. 4-9, pp. 1609–1612, 2006.

[94] A. K. Nallani, S. W. Park, and J. B. Lee, "Characterization of SU-8 as a photoresist for electron-beam lithography," pp. 414–423, International Society for Optics and Photonics, 2003.

[95] J. Ribe, "30 kV 1 µm SU-8 process," 2014. Available online at `https://github.com/NanoLabStaff/nanolab/wiki/SU-8-EBL`.

[96] M. Lončar, J. Vučković, and A. Scherer, "Methods for controlling positions of guided modes of photonic-crystal waveguides," *Journal of the Optical Society of America B*, vol. 18, no. 9, p. 1362, 2001.

[97] M. Notomi, A. Shinya, K. Yamada, J.-I. Takahashi, C. Takahashi, and I. Yokohama, "Structural tuning of guiding modes of line-defect waveguides of silicon-on-insulator photonic crystal slabs," *IEEE Journal of Quantum Electronics*, vol. 38, no. 7, pp. 736–742, 2002.

[98] W. C. Lai, S. Chakravarty, Y. Zou, Y. Guo, and R. T. Chen, "Slow light enhanced sensitivity of resonance modes in photonic crystal biosensors," *Applied Physics Letters*, vol. 102, no. 4, 2013.

[99] D. Gerace and L. C. Andreani, “Disorder-induced losses in photonic crystal waveguides with line defects,” *Optics Letters*, vol. 29, no. 16, p. 1897, 2004.

[100] M. Settle, M. Salib, A. Michaeli, and T. F. Krauss, “Low loss silicon on insulator photonic crystal waveguides made by 193nm optical lithography,” *Optics Express*, vol. 14, no. 6, p. 2440, 2006.

[101] R. Kappeler, P. Kaspar, and H. Jäckel, “Propagation loss computation of W1 photonic crystal waveguides using the cutback technique with the 3D-FDTD method,” *Photonics and Nanostructures - Fundamentals and Applications*, vol. 9, no. 3, pp. 235–247, 2011.

[102] M. Cryan, D. Wong, I. Craddock, S. Yu, J. Rorison, and C. Railton, “Calculation of losses in 2-D photonic Crystal membrane waveguides using the 3-D FDTD method,” *IEEE Photonics Technology Letters*, vol. 17, no. 1, pp. 58–60, 2005.

[103] M. G. Scullion, A. Di Falco, and T. F. Krauss, “Slotted photonic crystal cavities with integrated microfluidics for biosensing applications.,” *Biosensors & bioelectronics*, vol. 27, no. 1, pp. 101–5, 2011.

[104] M. Terrel, M. J. F. Digonnet, and S. Fan, “Ring-coupled Mach-Zehnder interferometer optimized for sensing.,” *Applied optics*, vol. 48, no. 26, pp. 4874–4879, 2009.

[105] F. P. Payne and J. P. R. Lacey, “A theoretical analysis of scattering loss from planar optical waveguides,” *Optical and Quantum Electronics*, vol. 26, no. 10, pp. 977–986, 1994.

[106] K. L. Lee, “Ultrasonic and dip resist development processes for 50 nm device fabrication,” *Journal of Vacuum Science & Technology B: Microelectronics and Nanometer Structures*, vol. 15, no. 6, p. 2621, 1997.

[107] J. Li, Q. X. Zhang, a. Q. Liu, W. L. Goh, and J. Ahn, “Technique for preventing stiction and notching effect on silicon-on-insulator microstructure,” *Journal of Vacuum Science & Technology B: Microelectronics and Nanometer Structures*, vol. 21, no. 6, p. 2530, 2003.

[108] H. Kuribayashi, R. Hiruta, R. Shimizu, K. Sudoh, and H. Iwasaki, “Investigation of shape transformation of silicon trenches during hydrogen annealing,” *Japanese Journal of Applied Physics, Part 2: Letters*, vol. 43, no. 4 A, 2004.

[109] J. S. Orcutt, S. D. Tang, S. Kramer, K. Mehta, H. Li, V. Stojanović, and R. J. Ram, “Low-loss polysilicon waveguides fabricated in an emulated

high-volume electronics process," *Optics Express*, vol. 20, no. 7, p. 7243, 2012.

[110] S. G. Johnson, "MIT Photonic Bands Website," 2016. Available online at `http://ab-initio.mit.edu/wiki/index.php/MIT_Photonic_Bands`.

[111] S. G. Johnson, "MIT Electromagnetic Equation Propagation Website," 2016. Available online at `http://ab-initio.mit.edu/wiki/index.php/Meep`.

[112] S. G. Johnson, "MIT Photonic Bands User Tutorial," 2014. Available online at `http://ab-initio.mit.edu/wiki/index.php/MPB_User_Tutorial`.

[113] S. G. Johnson, "Harminv Website," 2016. Available online at `http://ab-initio.mit.edu/wiki/index.php/Harminv`.

[114] V. a. Mandelshtam and H. S. Taylor, "Harmonic inversion of time signals and its applications," *The Journal of Chemical Physics*, vol. 107, no. 17, p. 6756, 1997.

[115] S. Fan, P. R. Villeneuve, and J. D. Joannopoulos, "Theoretical investigation of photonic crystals of fabrication-related disorder on the properties," *Journal of Applied Physics*, vol. 78, no. 3, pp. 1415–1418, 1995.

[116] E. Kuramochi, M. Notomi, S. Hughes, A. Shinya, T. Watanabe, and L. Ramunno, "Disorder-induced scattering loss of line-defect waveguides in photonic crystal slabs," *Physical Review B - Condensed Matter and Materials Physics*, vol. 72, no. 16, pp. 2–5, 2005.

[117] W. Bogaerts, P. Bienstman, and R. Baets, "Scattering at sidewall roughness in photonic crystal slabs.," *Optics letters*, vol. 28, no. 9, pp. 689–691, 2003.

[118] T. J. Atherton and D. J. Kerbyson, "Size invariant circle detection," *Image and Vision Computing*, vol. 17, no. 11, pp. 795–803, 1999.

[119] D. M. Beggs, L. O'Faolain, and T. F. Krauss, "Accurate determination of the functional hole size in photonic crystal slabs using optical methods," *Photonics and Nanostructures - Fundamentals and Applications*, vol. 6, no. 3-4, pp. 213–218, 2008.

[120] J. Canny, "A computational approach to edge detection.," *IEEE transactions on pattern analysis and machine intelligence*, vol. 8, no. 6, pp. 679–698, 1986.